Master's thesis

NTNU
Norwegian University of Science and Technology
Faculty of Natural Sciences
Department of Materials Science and Engineering

Emilie Bjønnes

Surface Treatment of Graphite for the Mitigation of Lithium Plating in Fast Charging Lithium-Ion Batteries

Master's thesis in Materials Science and Engineering
Supervisor: Ann Mari Svensson
Co-supervisor: Nils P. Wagner
June 2022

NTNU
Norwegian University of
Science and Technology

Emilie Bjønnes

Surface Treatment of Graphite for the Mitigation of Lithium Plating in Fast Charging Lithium-Ion Batteries

Master's thesis in Materials Science and Engineering
Supervisor: Ann Mari Svensson
Co-supervisor: Nils P. Wagner
June 2022

Norwegian University of Science and Technology
Faculty of Natural Sciences
Department of Materials Science and Engineering

NTNU
Kunnskap for en bedre verden

Preface

This thesis concludes five years of studies at the Department of Materials Science and Engineering at NTNU. The work presented has been carried out during the spring of 2022. All of the experimental work was conducted by the author except for the FIB post mortem characterisation, which kindly was performed by post doctoral fellow Inger-Emma Nylund.

It has been truly interesting to take part in Vianode's project "Surface treatment of Artificial Graphite" (SAGA) for the past year, through this master's thesis and the project work carried out in the autumn of 2021. Hence, I would like to thank Vianode and especially the SAGA project leader Navaneethan Muthuswamy for their collaboration and for letting me be a part of their exciting project.

Moreover, a special thanks to my supervisor Ann Mari Svensson for her valuable help, guidance and feedback throughout the whole semester. Much appreciation and thanks must also be directed to my co-supervisor Nils P. Wagner for his valuable inputs in many insightful discussions. I would also like to thank all the bright people at the NTNU Battery Group for helping out whenever needed and for sharing your interesting research. Lastly, I would like to thank my fellow students at materials science for all the great memories from the past five years, and especially Mari Hognestad and Ragnhild Åkre Reite for making life at the battery lab the past year a lot of fun.

Trondheim, June 2022

Abstract

The graphite anode has been the preferred choice for use in lithium-ion batteries (LIBs) since their commercialisation in 1991, due to its low cost, raw material abundance, relatively high energy and power density, and long cycle life. However, the occurrence of lithium (Li) plating on the anode surface upon fast charging poses a safety and degradation risk to the LIB. The reason for this is that growth of dendrites of plated Li metal can puncture the separator and cause a short circuit and fire of the LIB. Thus, the graphite anode must be developed with a focus on its capability to mitigate Li plating, as the improved fast charging capability of LIBs plays a crucial role in electrifying the transportation sector.

This thesis investigates the effects of surface treatment of graphite particles on mitigation of Li plating by comparing two synthetic graphite powders, i.e. one pristine and one surface modified by amorphous carbon coating. Half cells with Li metal as the counter electrode were electrochemically tested to investigate the effect of Li plating and the mitigation capabilities of the graphite powders by deliberately imposing Li plating by lithiation of the graphite electrode below 0 V vs. Li/Li^+. Using potential and differential capacity plots, the amount of reversible and irreversible plating was quantified after a set amount of plating was imposed at 50% and 100% state of charge (SOC). The results were in agreement with the literature, namely, that the risk of plating increases with an increased SOC due to the increased resistance towards lithiation for increased concentrations of Li in the graphite structure. Furthermore, the surface modified graphite particles mitigated Li plating to a greater extent in both cases, as less plating was quantified for the modified cells than for the pristine cells. Also, the first cycle irreversible capacity loss was reduced for the modified cells, resulting in a thinner solid electrolyte interface layer. This was linked to the reduced surface roughness of the modified powder.

Cyclic voltammetry measurements confirmed the more favourable cell kinetics of the modified cell, as the lithiation and delithiation occurred at higher and lower potentials, respectively, compared to for the pristine cell. Impedance measurements performed before and after imposed Li plating revealed that the total electrode resistance was lower and the active internal surface area, derived from the capacitance, was larger for the modified cell. These findings support the theory about how amorphous carbon coating results in a smoother surface that reduces resistance towards desolvation of Li-ions on the anode surface, which is a key factor for mitigating Li plating.

In order to detect any residual Li plating and possible degradation, post mortem scanning electron microscopy using secondary and backscattered electrons was utilised. The effect of plating C-rate was visible by detection of two different plating structures, i.e. thick dendrites for high C-rates and a mossy and more porous structure for low C-rates. The latter structure may contribute to higher irreversible plating and an increased risk of electrolyte depletion, and should be examined further.

Overall, the findings show that the surface treatment of graphite with amorphous carbon coating mitigates the risk of Li plating and improves the fast charging capability of the graphite anode.

Sammendrag

Grafittanoden har vært det foretrukne valget for bruk i litium-ionbatterier (LIB-er) siden de ble kommersialisert i 1991, på grunn av dens lave kostnad, råmaterialtilgjengelighet, relativt høye energi- og effekttetthet og lange syklingsliv. Imidlertid utgjør forekomsten av litium (Li)-plettering på anodeoverflaten ved hurtiglading en sikkerhets- og degraderingsrisiko for LIB-er. Grunnen til dette er at vekst av dendritter av belagt Li-metall kan punktere separatoren og forårsake kortslutning og brann i batteriet. Derfor må grafittanoden utvikles med søkelys på dens evne til å redusere Li-plettering, ettersom forbedringen av hurtigladeevnen til LIB-er spiller en avgjørende rolle i å elektrifisere transportsektoren.

Denne oppgaven undersøker effekten av å overflatebehandle grafittpartikler for å begrense Li-plettering ved å sammenligne to syntetiske grafittpulver, dvs. et ubehandlet og et overflatemodifisert med amorft karbonbelegg. Halvceller med Li-metall som motelektrode ble elektrokjemisk testet for å undersøke effekten av Li-plettering og evnen til grafittpulveret til å begrense Li-plettering. Li-metall ble bevisst plettert ved å litiere grafittelektroden under 0 V vs. Li/Li^+. Mengden reversibel og irreversibel plettering ble kvantifisert ved å analysere potensial- og differensialkapasitetsplott etter at Li-plettering ble pålagt ved 50% og 100% oppladning. Resultatene samsvarte med litteraturen, nemlig at risikoen for plettering øker med økt oppladning på grunn av den økte motstanden mot litiering for økte konsentrasjoner av Li i grafittstrukturen. Videre reduserte de overflatemodifiserte grafittpartiklene Li-pletteringen i større grad i begge tilfellene, ettersom mindre plettering ble kvantifisert for de modifiserte cellene enn for de ubehandlede cellene. I tillegg ble det irreversible førstesykel kapasitetstapet redusert for de modifiserte cellene, noe som resulterte i et tynnere overflatesjikt mellom grafittanoden og elektrolytten (SEI). Dette var knyttet til den reduserte overflateruheten til det modifiserte pulveret.

Syklisk voltammetrimålinger bekreftet den mer gunstige cellekinetikken til den modifiserte cellen, da litieringen og delitieringen skjedde ved henholdsvis høyere og lavere potensialer sammenlignet med for den ubehandlede cellen. Impedansmålinger utført før og etter Li-plettering viste at den totale elektrodemotstanden var lavere og det indre aktive elektrodearealet, avledet fra kapasitansen, var større for den modifiserte cellen. Disse funnene støtter teorien om hvordan et amorft karbonbelegg resulterer i en jevnere overflate som reduserer motstanden mot desolvasjon av Li-ioner på anodeoverflaten, og på denne måten kan anses som en sentral faktor for å redusere Li-plettering.

For å oppdage eventuell gjenværende Li-plettering og mulig degradering, ble post mortem skanning elektronmikroskopi med sekundære og tilbakespredte elektroner brukt. Effekten av pletteringsstrømmen var synlig ved påvisning av to forskjellige pletteringsstrukturer, dvs. tykke dendritter for høye C-rater og en moseliknende og mer porøs struktur for lave C-rater. Sistnevnte struktur kan bidra til høyere irreversibel plettering og økt risiko for elektrolyttreduksjon, og bør undersøkes nærmere.

Alt i alt viser funnene at overflatebehandlingen av grafitt med amorft karbonbelegg reduserer risikoen for Li-plettering og dermed forbedrer grafittanodens hurtigladingsevne.

Contents

List of Figures

List of Tables

List of Abbreviations

BET	Brunauer-Emmett-Teller
BSE	Backscattered electron
CB	Carbon black
CE	Coloumbic efficiency
CMC	Carboxymethyl cellulose
CPE	Constant phase element
CV	Cyclic voltammetry
DEC	Diethyl carbonate
DI	Deionised
DMC	Dimethyl carbonate
EC	Ethylene carbonate
EDS	Energy disperse X-ray spectroscopy
EIS	Electrochemical impedance spectroscopy
EMC	Ethyl methyl carbonate
EV	Electric vehicle
FEC	Fluoroethylene carbonate
FIB	Focused ion beam
GD-OS	Glow discharge optical emission spectroscopy
GEIS	Galvanostatic electrochemical impedance spectroscopy
GIC	Graphite intercalation compound
HOMO	Highest occupied molecular orbital
ICL	Irreversible capacity loss
LIB	Lithium-ion battery
LUMO	Lowest unoccupied molecular orbital
PC	Propylene carbonate
PEIS	Potentiostatic electrochemical impedance spectroscopy
PP	Polypropylene
PSD	Particle size distribution
SBR	Styrene butadiene rubber
SE	Secondary electron
SEI	Solid electrolyte interface
SEM	Scanning electron microscopy
SOC	State of charge
VC	Vinylene carbonate
vdW	van der Waals
WD	Working distance

1 Introduction

1.1 Background and Motivation

In IPCC's Sixth Assessment Report published this spring, it was made clear that climate change will present multiple unavoidable risks to ecosystems and humans, as a result of the global warming being on a trajectory to exceed 1.5 °C before 2040.[1] Hence, strong countermeasures to reduce greenhouse gas emissions must be made. One such countermeasure is to electrify the transportation sector with reliable and sustainable batteries.[2]

The number one battery technology for use in electric vehicles (EVs) today is the lithium-ion battery (LIB), due to its low cost, raw material abundance, relatively high energy and power density, and long cycle life.[3,4] The fundamental principles of LIBs are attributed the initial discoveries of the lithium (Li) metal battery by Wittingham and the reversible intercalation mechanism in graphite and cathodic oxides by Besenhard in the 1970s. Yet, it was not until 1991 that Sony successfully commercialised the first LIB.[3] Over the past 30 years, extensive research has been put into improving the LIB technologies in order to satisfy the requirements, such as high energy density, low cost, and long cycle life, for application in EVs. In 2020, the global EV stock surpassed 10 million after a rapid growth over the last decade, due to the improved driving range of EVs (>500 km) combined with government incentives in some countries.[2] Nevertheless, there will still be a need for fast charging opportunities along the road, which poses some challenges for the current LIBs.

Fast charging is a factor that contributes to reduced energy efficiency, increased safety risk, and capacity deterioration. One major culprit is the undesired mechanism of Li plating where the Li-ions are reduced to metallic Li on the anode surface instead of being intercalated into the graphite structure.[5] Graphite has been the preferred anode material in LIBs since the commercialisation in 1991, and holds a dominating market share of 98%. This is mainly due to its low cost, raw material abundance, high energy and power density, and long cycle life.[6] However, the occurrence of Li plating upon fast charging poses a safety and degradation risk to the LIB.

Many works have investigated the nature of Li plating in detail. In this way, the triggering factors for its occurrence, in-situ and post mortem characterisation techniques for its detection and quantification, and methods for its mitigation have been revealed to a great extent. The details of some of these insights will be presented and later discussed in relation to reported results of this thesis, which involve materials and electrochemical characterisation of one pristine and one surface modified synthetic graphite powder. Hopefully, this will contribute to add further knowledge to the topic of Li plating and the development of graphite anodes with better fast charging capabilities.

1.2 Aim of This Work

The overall aim of this thesis is to investigate whether the surface treatment of the graphite particles affects the susceptibility of the anode material towards Li plating. To reach the main goal, procedures for imposing Li plating on the anode, as well as procedures for quantifying the amounts and evaluating the effect of the plating, will be developed and utilised. Two synthetic graphite powders, i.e. one pristine and one surface modified, are compared with the objective of investigating the factors that mitigate Li plating. Moreover, Li plating and stripping reactions are compared, and the effect on the anode performance is evaluated.

The graphite powders are electrochemically characterised using galvanostatic cycling, cyclic voltammetry (CV), and electrochemical impedance spectroscopy (EIS) in half cells with Li metal as the counter electrode. In the cycling programmes, plating is imposed on the graphite anodes with the aim of evaluating which powder that is less susceptible towards plating. The effect of plating at different state of charge (SOC) and charging C-rates is also investigated. Moreover, factors such as cell performance and the amount of reversible and irreversible plating are investigated and compared. Hence, the thesis explores methods for detecting and quantifying the plating through electrochemical characterisation and post mortem characterisation using scanning electron microscopy (SEM). To investigate how surface modifications may affect the mitigation of plating, active materials characterisation of the powders are performed to examine differences in morphology, specific surface area, and particle size and distribution.

The graphite powders are provided by Vianode, and this work has been a part of their ongoing project with the goal of developing the best and safest anodes for fast charging LIBs.

2 Theory

2.1 The Lithium-Ion Battery

2.1.1 Working Principle

This section provides an overview of the working principle of a LIB, and is mostly based on two articles; one by Goodenough and Park[4] and one by Zubi et al.[3] The LIB is an electrochemical cell that converts chemical energy into electricity and vice versa by rocking Li-ions back and forth between the electrodes. The positive electrode is commonly referred to as the cathode and the negative electrode is referred to as the anode, and upon charge of the cell this is where reduction and oxidation occur, respectively. This terminology is commonly used when considering secondary batteries and will be used for conciseness purposes in this thesis too, despite the fact that both electrodes alternate between being the cathode and anode upon charge and discharge.

Figure 2.1 illustrates the working principle and main components of a LIB. Upon charge of the cell, the Li-ions are extracted from the cathode, which is composed of a layered oxide $LiMO_2$ including a transition metal "M", i.e. usually Co, Ni, or Mn. The liquid electrolyte has a high ionic conductivity to enable fast transport of Li-ions over to the anode. Here, the ions intercalate into and are stored in the layered structure of graphite, which is the most utilised anode material in commercial LIBs. In addition, a porous polymer separator located between the electrodes prevents electrical short-circuiting of the cell by being soaked in electrolyte. Upon discharge of the cell, the Li-ions flow spontaneously back into the cathode, due to the difference in electrochemical potential between the electrodes. Electrons are forced to move in an external circuit where they perform work, due to the presence of the separator and the poor electronic conductivity of the electrolyte.

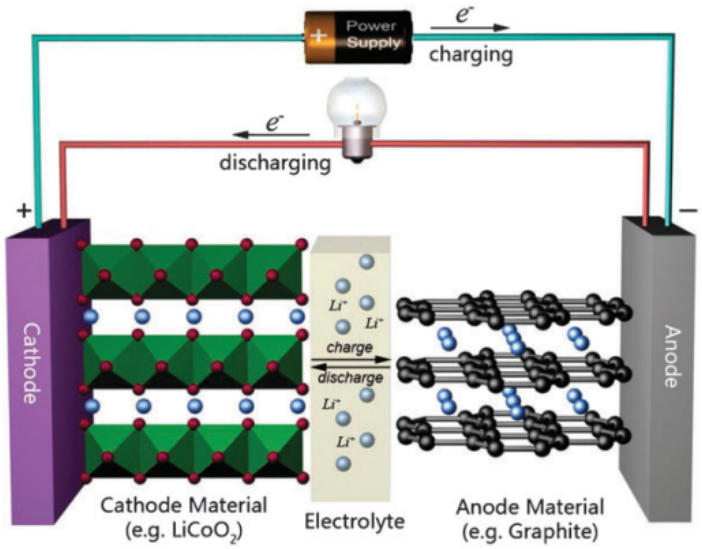

Figure 2.1: Illustration of the working principle of a LIB. Figure adapted from Liu and Duay.[7]

The reversible electrochemical reactions occurring at the electrodes are the following:

- Anode (-): $\mathrm{Li_xC_6} \underset{\text{charge}}{\overset{\text{discharge}}{\rightleftharpoons}} \mathrm{C_6} + \mathrm{xe^-} + \mathrm{xLi^+}$
- Cathode (+): $\mathrm{Li_{1\text{-}x}MO_2} + \mathrm{xe^-} + \mathrm{xLi^+} \underset{\text{charge}}{\overset{\text{discharge}}{\rightleftharpoons}} \mathrm{LiMO_2}$

where $0 < x < 1$.

It is the Li-ion donor in the cathode that gives rise to the name of the various commercial LIB technologies, because this determines the main battery characteristics and thus the main differences between them. An overview of cathode materials is provided in Section 2.3. Despite the varieties, the cell voltage upon discharge of LIBs normally lies around 3.5 V vs. $\mathrm{Li/Li^+}$, which results in a high specific energy and power density compared to other secondary cells such as lead-acid and NiCd batteries. In addition, the long cycle lives, high reliability, and intensive R&D efforts in the technology have made the LIB the number one choice for use in portable electronics and EVs.

2.1.2 Important Parameters and Equations

The following parameters and equations are important when considering the characteristics and performance of a LIB:[4]

1. **Capacity** Q is the total charge q that is possible to store in the battery. It depends on the specific capacities of the electrodes, in which the cathode usually is the limiting factor. It can be obtained by calculating the total charge transferred by the current $I = dq/dt$ on discharge or charge of the battery, as given by the following equation:

$$Q = \int_0^{\Delta t} I\,dt = \int_0^{Q} dq \tag{2.1}$$

2. **Specific capacity** is the capacity of an electrode, i.e. the theoretical amount of charge that the active electrode material can convert per unit weight, which is given by Faraday's law:

$$Q_{th} = \frac{nF}{M} \tag{2.2}$$

   where n is the number of electrons involved in the electrode reaction, M is the molecular mass of the electroactive components, and F is the Faraday constant. The unit of the specific capacity is usually expressed in mAh $\mathrm{g^{-1}}$ with F equal to 26.8 Ah.

3. **Energy** is given as the product of the charge and the open-circuit potential of the cell, as given by the following equation:

$$Energy = \int_0^{Q} V(q)\,dq \tag{2.3}$$

   By dividing the energy available by the mass of the battery, one can determine the gravimetric energy density (Wh $\mathrm{kg^{-1}}$), which is especially important for application in EVs.

4. **Open-circuit potential** V_{oc} is the difference between the electrochemical potential of the anode μ_A and cathode μ_C divided by the electron charge e:

$$V_{oc} = \frac{\mu_A - \mu_C}{e} \tag{2.4}$$

5. **(Dis-)charge potential**. The discharge potential V_{dis} is the output potential of a cell during discharge. The V_{oc} is reduced by an overvoltage η origin from an internal battery resistance R_b to the ionic current, i.e. $\eta = I_{dis}R_b$, which can be expressed as:

$$V_{dis} = V_{oc} - \eta(q, I_{dis}) \tag{2.5}$$

The charge potential V_{ch} is the potential required to reverse the chemical reactions in the cell upon charge, and is the addition of an overvoltage $\eta = I_{ch}R_b$ to the open-circuit potential:

$$V_{ch} = V_{oc} + \eta(q, I_{ch}) \tag{2.6}$$

where q is the amount of charge stored in the battery at a given time, commonly referred to as the SOC.

6. **C-rate** is the current corresponding to a certain charge or discharge rate of the battery. For instance, 1C corresponds to the current that will discharge or charge the battery in 1 hour, 2C equals the current at which the battery is charged or discharged in 30 minutes, and 0.5C equals the current at which the battery is charged or discharged in 2 hours, and etc. The C-rate of a cell is determined by the capacity of the electrode.[8]

7. **Coloumbic efficiency** (CE) is the yield of capacity for a single charge/discharge cycle. It is found by taking the ratio of charge obtained upon discharge Q_{dis} over the charge stored upon charge Q_{ch}:

$$\text{CE} = \frac{Q_{dis}}{Q_{ch}} \times 100\% \tag{2.7}$$

For the anode, the CE is the ratio of the amount of Li-ions that can be retrieved from the electrode upon delithiation over the amount of Li-ions that can be stored in the electrode upon lithiation. For the cathode, the CE is the ratio of the amount of Li-ions that enter the electrode upon lithiation over the amount extracted upon delithiation.

8. **Irreversible capacity loss** (ICL) is the deviation from CE = 100%, i.e:

$$\text{ICL} = 100\% - \text{CE} = \frac{Q_{ch} - Q_{dis}}{Q_{ch}} \times 100\% \tag{2.8}$$

As given by the name, this is an irreversible loss and should hence be minimised as much as possible.

9. **Cycle life** is the number of cycles until the capacity of the cell has been reduced to 80% of the initial value. It is important that commercial batteries have long cycle lives to prolong the lifetime of EVs and consumer electronics.

2.2 Electrolyte and Solid Electrolyte Interface Layer

The electrolyte is an important component in the LIB, as it enables the transportation of Li-ions between the electrodes. Most of the electrolytes used in commercial LIBs are non-aqueous solutions in which a Li salt, usually Li hexafluorophosphate ($LiPF_6$), is dissolved in organic carbonate solvents. Important criteria that the electrolyte should fulfill are summarised in the following bullet points:[9]

- Good ionic conductivity and electronic insulation to minimise self-discharge of the cell
- Electrochemically inert with the electrode surfaces in the operating voltage window of the cell
- Non-reactive with other components of the cell, e.g. separator and current collectors
- Environmentally friendly

The electrolyte stability window E_g gives the voltage range with which the electrolyte is thermodynamically stable, and equals the energy separation of the lowest unoccupied molecular orbital (LUMO) and the highest occupied molecular orbital (HOMO), as illustrated by Figure 2.2. If the anode has an electrochemical potential μ_A above the LUMO, the electrolyte will be reduced, and similarly if the cathode has an electrochemical potential μ_C below the HOMO, the the electrolyte will be oxidised.[10]

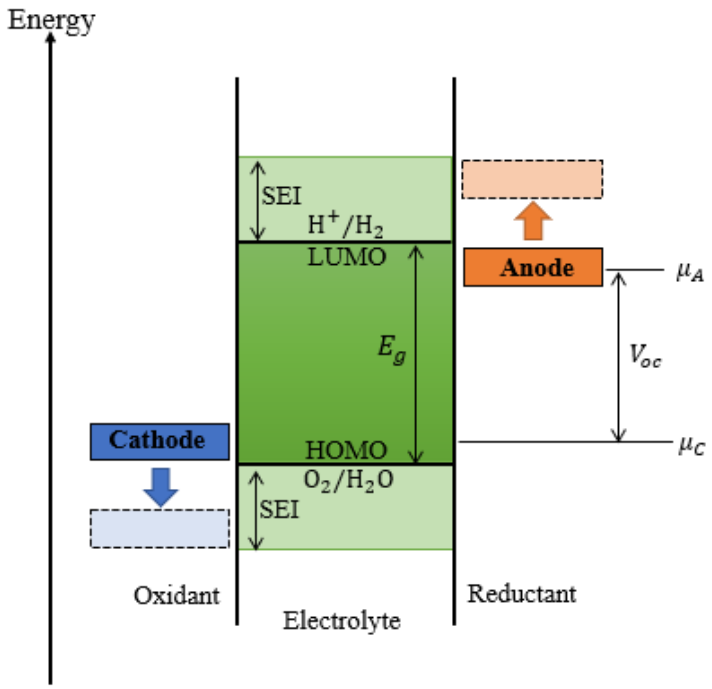

Figure 2.2: Illustration of the electrolyte stability window E_g. The anode and cathode electrochemical potentials are denoted by μ_A and μ_C, respectively. Figure inspired from Goodenough and Kim.[10]

The reduction and oxidation of electrolyte on the electrode surfaces result in the formation of a passivation layer, namely the solid electrolyte interface (SEI) layer, at the anode/electrolyte interface mainly during the first few cycles. The SEI layer is composed of a dense layer of inorganic compounds, such as Li_2O, Li_2CO_3, and LiF, that are thermodynamically stable against Li, which again is covered by organic decomposition products.[11] Further breakdown of the electrolyte and electrodes can be stopped by obtaining a stable SEI layer, as this will limit the electron transfer from the anode to the electrolyte and from the electrolyte to the cathode. This results in a kinetic stability in the cell and allows for operation outside of the stability window.[9,10] Additionally, too extensive growth and build-up of the SEI layer lead to increased internal resistance and capacity fade with consumption of active Li from the Li salt in the electrolyte. Therefore, the composition of the electrolyte is important to optimise, as the correct combination of linear and cyclic carbonate organic solvents, e.g. ethylene carbonate (EC), ethyl methyl carbonate (EMC), diethyl carbonate (DEC), and dimethyl carbonate (DMC), leads to the desired SEI-forming ability, high ionic conductivity, and good viscosity of the electrolyte.[9]

One negative aspect of the organic carbonate solvents is that they are not thermodynamically stable at low potentials against Li/Li^+ with decomposition occurring at about 0.8 V vs. Li/Li^+. Consequently, the formation of the SEI layer is more prominent at the anode surface, due to the Li intercalation primarily occurring below this potential.[9,11,12] Luckily, Fong et al.[13] discovered in 1990 that the use of sufficient EC in the electrolyte rather than propylene carbonate (PC) would prevent further decomposition of the electrolyte by forming a static SEI layer after the first few initial charge/discharge-cycles of the cell. Nonetheless, the SEI formation and change over time are still considered as main causes for cell deterioration with increased internal resistance and capacity fade.[9] Section 2.5 will provide more details on the importance of electrolyte compatibility with the graphite anode.

2.3 Cathode Materials

The characteristics of lithium such as high availability, non-toxicity, low molar mass, and high electropositivity are among the main reasons for why the LIB has become the dominating battery technology today. However, one utilises oxide compounds that can donate Li-ions as cathode material, because metallic Li is highly reactive and causes safety issues with dendrite growth on the Li metal electrode. The oxide compounds give rise to the name of the different LIBs and the main differences between them.[3,14] The state of the art oxide cathodes can be divided into three categories based on their crystal structure, i.e. layered, spinel, and polyanion, as illustrated in Figure 2.3.[14]

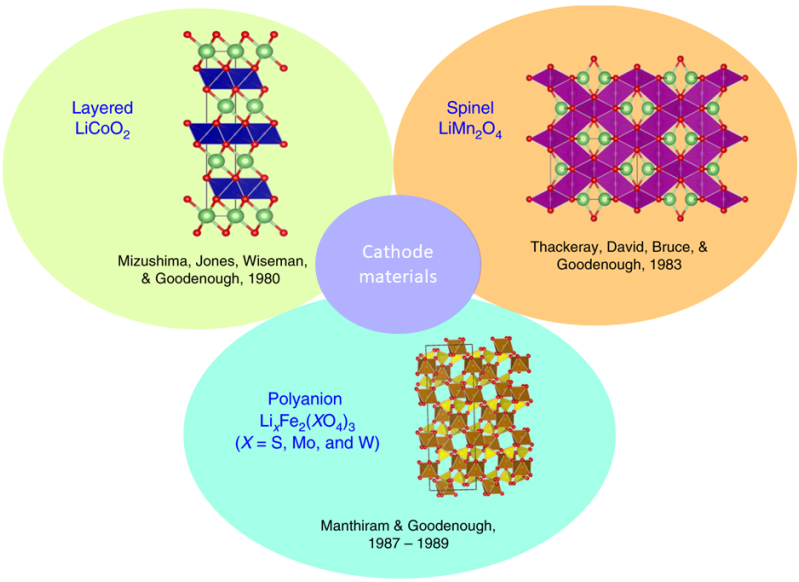

Figure 2.3: Illustration of the different crystal structures of state of the art cathode oxides, i.e. layered, spinel, and polyanion. Figure adapted from Manthiram.[14]

The layered oxide cathodes offer good structural stability, high energy density, high electrical and Li-ion conductivity, and high operating voltages of 4 V, which overall makes these types among the best cathodes today. Examples of well-known and commercially available layered oxides are $LiCoO_2$ (LCO), $LiNi_{1-y-z}Co_yMn_zO_2$ (NMC) and $LiNi_{1-y-z}Co_yAl_zO_2$ (NCA).[14]

Likewise, the three-dimensional structure of the spinel oxides provides a high structural stability and a low internal resistance for the conduction of Li-ions. $LiMnO_4$ (LMO) is a well-known example within this class, and it particularly allows for a high specific power, long cycle life, high thermal stability, and low cost of LIBs. However, the energy density is lower compared to the layered oxides.[3,14]

Lastly, the polyanion oxides generally have lower energy and power densities, due to poor electronic conductivity. Yet, advantages of high thermal stability, inherent safety, and environmentally friendly materials have made the $LiFePO_4$ (LFP) cathode increasingly more suitable for use in EVs and power supply systems.[3,14]

Overall, it is the cathode that limits the energy density of the LIB, as the theoretical capacity of the cathode materials (120-270 mAh g^{-1}) are much smaller compared to the anode materials (372-4000 mAh g^{-1}).[6,15] This is mainly due to unresolved degradation mechanisms linked to metal dissolution, phase transitions, and electrolyte oxidation, which limit the operating potential window to 4.2-4.3 V and hence a limited capacity.[15] However, further details on cathode materials will not be discussed, as this goes outside of the main scope of this thesis.

2.4 Anode Materials

The anode materials in LIBs should fulfill the following key criteria:[16]

- Light and accommodate as much Li as possible to obtain a high gravimetric capacity
- The redox potential against Li/Li^+ should be as low as possible at any Li concentration to enable a high energy density
- Good ionic and electronic conductivity to enable high power density
- Non-soluble in the solvents of the electrolyte and non-reactive with Li salt
- High safety to avoid thermal runaway of the battery
- High cycle life and reversible capacity
- Low cost
- Environmentally friendly

Li metal has been proposed as anode material, due to its high theoretical capacity of 3860 mAh g^{-1}. However, safety issues with dendrite formation on the Li metal upon charge and poor cycle life prevent the use of Li metal as anode material in commercial LIBs.[17,18] Therefore, alternative anode materials meeting the criteria above have been developed or suggested as promising candidates. These can be divided into three main categories based on their reaction mechanism with Li; intercalation materials, alloying materials, and conversion materials.[17,18] Figure 2.4 provides an overview of the various anode materials with their potential range plotted against Li/Li^+ and the corresponding capacity.

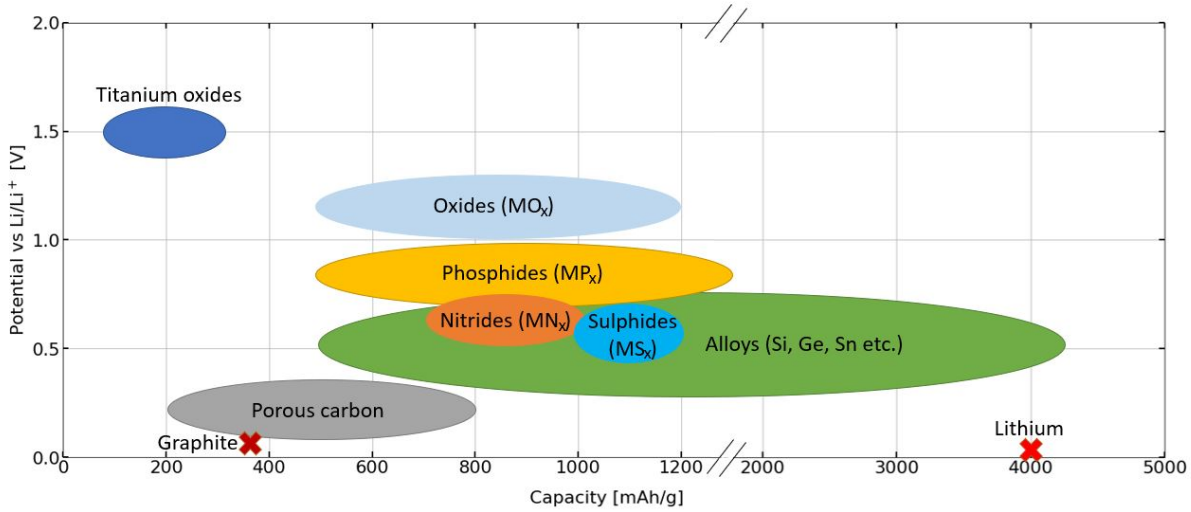

Figure 2.4: Illustration of the capacity and potential against Li/Li^+ for the different groups of anode materials. Figure inspired from Goriparti.[18]

2.4.1 Intercalation Materials

The most common intercalation materials are carbon based materials (e.g. graphite, porous carbon, and carbon nanotubes), TiO_2, and $Li_4Ti_5O_{12}$ (LTO).[18] These materials store guest ions, i.e. Li-ions in the case of a LIB, in a solid host structure. The ions can be reversibly inserted into and removed from the structure, which commonly is referred to as intercalation and deintercalation, respectively.[17]

The successful reversible electrochemical intercalation of Li-ions in graphite by Samar Basu in the late 1970s was a substantial factor in enabling the commercialisation of LIBs in 1991.[3] Up until today, over 30 years later, nearly all anodes used in commercial LIBs have been made of graphite. This is due to the graphite anode having the combined properties of a relatively good gravimetric capacity of 372 mAh g^{-1}, high cycle life, raw material abundance, and low cost.[3] Graphite as anode material will be discussed further in Section 2.5.

Another commercialised anode material is LTO, which provides superior thermal stability, high rate, and high cycle life. In addition, LTO's high potential of 1.55 V vs. Li/Li^+ means that it can operate in a potential window above 1 V, thus reducing the formation and growth of SEI on the anode surface, which is a problem for the graphite anodes. However, drawbacks such as the high cost of Ti, reduced cell voltage, low electronic conductivity, and low gravimetric capacity of 175 mAh g^{-1} have limited LTO's success as anode material.[17,18]

TiO_2 is regarded as a very promising anode material, due to its high safety and stability with its operative potential of 1.5 V vs. Li/Li^+. In addition, TiO_2 is highly cost effective, of high abundance, and inherits good chemical stability and a relatively high theoretical capacity of 330 mAh g^{-1}.[18] However, it is yet to be commercialised, due to unresolved challenges linked to fully exploiting its capacity and rate performance.[19]

2.4.2 Alloying Materials

Alloying materials in the context of battery materials refer to elements, "X", which electrochemically alloy and form compound phases with Li at a low potential in the following way:[17]

$$yLi^+ + X \rightleftharpoons Li_yX$$

The main benefit of alloying materials over intercalation materials is the extremely high specific capacity, both volumetric and gravimetric. Some of the most promising alloying elements include Si, SiO, Ge, and SnO. Their specific capacity ranges from 783 mAh g^{-1} for SnO up to 4211 mAh g^{-1} for Si. However, the volume expansion/contraction of several times the original volume upon lithiation/delithiation poses as a great drawback and challenge, due to loss of electrical contact with the current collector, electrolyte decomposition, and destruction of the SEI layer. Overall, this leads to a short cycle life caused by loss of active material and increased cell impedance.[17]

One promising solution to tackle the expansion problems has been to produce carbon composites where small particles of the alloying material are incorporated. In this way, the mechanical stability of the anode is improved and the Li diffusion paths upon lithiation are maintained. Yet, electrodes with high mass loading and long cycle life have still not been demonstrated.[17,18]

2.4.3 Conversion Materials

The third category of anode materials involves the transition metal conversion materials such as oxides, phosphides, sulphides and nitrides. The Li is stored through reversible solid-state redox reactions between the Li-ions and the transition metal cations, which can be expressed in the following way:[18,20]

$$M_xN_y + zLi^+ + ze^- \rightleftharpoons Li_zN_y + xM$$

where M = Fe, Co, Cu, Mn, or Ni, and N = O, P, S, or N.

These anode materials provide high specific capacities (500-1000 mAh g^{-1}), due to the large number of electrons involved in the reactions.[18] Nevertheless, the large voltage hysteresis and poor cycle life caused by intrinsically poor electronic and ionic conductivity, continuous electrolyte decomposition, and relatively large volume expansions have prevented any commercial application of these materials so far.[17,20]

2.5 The Graphite Anode

Despite efforts in developing new anode materials with higher energy densities like the alloying Si anode, the graphite anode holds the dominating market share with its reliable technology, relatively high energy density, and exceptional cycle life. It has been the preferred anode ever since the commercialisation of LIBs in 1991, and it is expected that this trend continues in the closest future as well.[6,11] An in-depth review of the advantageous characteristics of graphite as anode material, but also some of its challenges and drawbacks, will be presented in this section.

2.5.1 Electrode Components

The graphite electrode is mainly made of graphite (90-95 wt%) with the final percentages usually comprising of carbon black (CB) and binder materials. The CB improves the contact between graphite particles, which results in an optimal conductive matrix. The binder materials, usually styrene butadiene rubber (SBR) and carboxymethyl cellulose (CMC), provide good adhesion between the particles, and between the electrode components and the Cu current collector.[21]

2.5.2 Crystal Structure and Intercalation Mechanism

Figure 2.5a illustrates the crystal structure of graphite used in LIBs, i.e. a hexagonal symmetry with graphene layers stacked in an ABAB-sequence.[22] This structure is thermodynamically favoured over rhomobohedral graphite with ABCABC-stacking. The graphene layers in the hexagonal structure are sp^2 hybridized and linked together by weak van der Waals (vdW) forces and π-π interactions of delocalised electrons.[23] This results in a 2D layered structure with high anisotropy, which is key for enabling the storage of Li-ions between the graphene layers through intercalation. This is as the weak vdW forces between the layers and high in-plane mechanical strength allow for expansion of the interlayer distance by approximately 10.3% upon intercalation.[11,22,23] Additionally, the stacking sequence changes to an AA-sequence upon intercalation, as illustrated by Figure 2.5b.[22]

The intercalation reaction occurs primarily at the edge planes, also known as prismatic surfaces, due to their higher surface energy and thus higher surface reactivity towards Li-ions compared to the basal planes.[11,23] Nevertheless, intercalation may occasionally occur at the basal planes through defect sites with higher surface reactivity.[24]

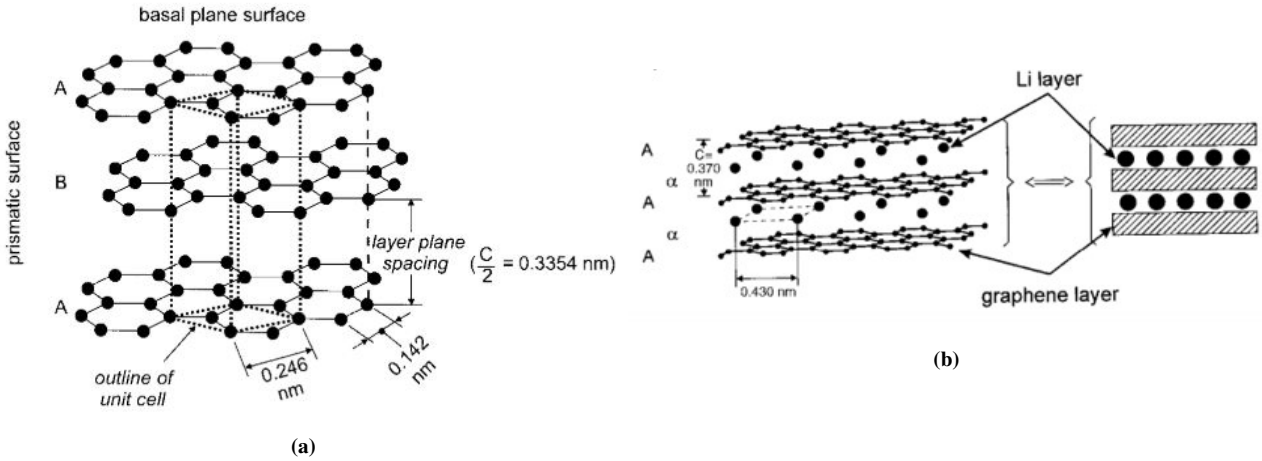

Figure 2.5: (a) Crystal structure of hexagonal graphite and (b) stacking sequence of intercalated lithium in graphite. Both figures from Winter et al.[22]

The Li-ions intercalate into graphite with the following stoichiometry:[10]

$$C_6 + xe^- + xLi^+ \rightleftharpoons Li_xC_6$$

Upon intercalation, graphite intercalation compounds (GICs) are formed with LiC_6 representing the final compound formed upon a fully charged cell, i.e. one Li per hexagonal carbon ring. This translates to a theoretical capacity of 372 mAh g^{-1}, which, in combination with the low intercalation potential against Li/Li^+ over nearly the entire charge/discharge cycle, as illustrated in Figure 2.6, enables the LIB to achieve relatively high energy densities.[6,21]

The intercalation proceeds through several stages of successive formation of different GICs; stage-IV (not well-defined composition), stage-III (LiC_{24}), transition stage-II L (LiC_{18}), stage-II (LiC_{12}), and stage-I (LiC_6).[21] The stage-*n* denotes the number of graphene layers between any successive intercalate layers, i.e. every filled layer is followed by *n* graphene layers.[6] The transition stage-II L accounts for the Li-ions not being perfectly ordered within the layers, but more in a liquid-like manner.[11] The transitions are recognised by a drop in potential, as an increased Li content results in increased Li activity. Figure 2.6 illustrates these drops with 0.09 V corresponding to the transition between stage-I and -II, 0.12 V between stage-II and -II L, 0.14 V between both stage-II L and -III, and stage-III and -IV, and 0.20 V between stage-IV and -I, with all potentials given with respect to Li/Li^+.[21]

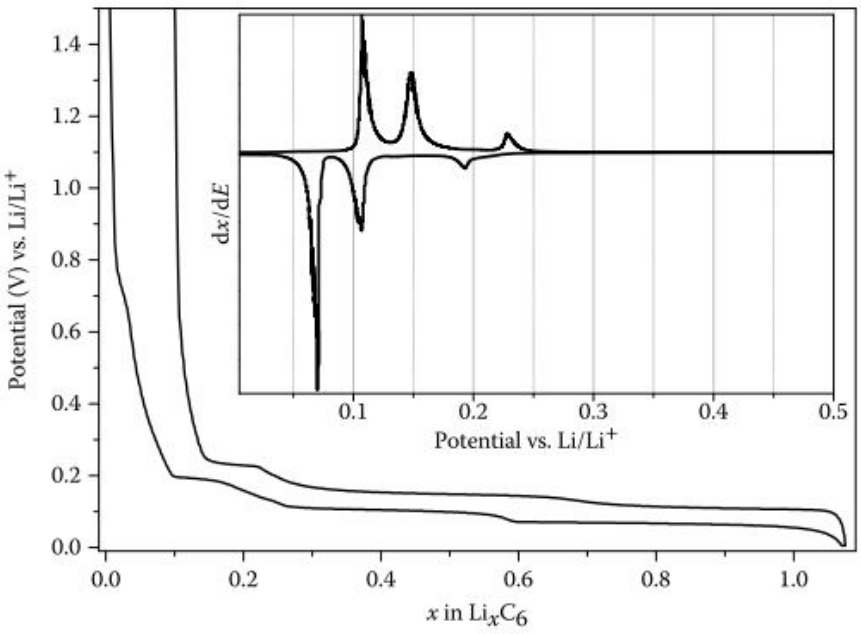

Figure 2.6: First galvanostatic charge (Li intercalation) and discharge (Li deintercalation) curve for a cell with a graphite working electrode and metallic Li counter electrode. The inset shows the derivative of the composition (x in Li_xC_6) with respect to the potential. Figure from Novák et al.[21]

2.5.3 Challenges Linked to the SEI Layer

The intercalation mechanism has been crucial to understand for the success of the graphite anode, but so has the formation of a static SEI layer on the anode surface. Its presence is necessary in order to prevent further breakdown of the electrolyte and corrosion of the anode surface, due to the intercalation occurring below the stability limit at 0.8 V vs. Li/Li^+ for carbonate-based electrolytes. However, it also comes with some challenges and negative aspects.[11]

One of the main negative aspects is the first cycle ICL (Equation 2.8, Section 2.1.2), due to the formation of the SEI layer in the initial cycles. This loss (approximately 10-20%) is unavoidable, due to the need of the SEI layer, but should still be minimised for optimisation of the energy density.[11] It is broadly accepted in the literature that the first cycle ICL depends on the electrode surface area and the specific Brunauer-Emmett-Teller (BET) surface area of the graphite. This is because the SEI layer covers all the surface area exposed to the electrolyte.[25] In this way, graphite with a low surface area, i.e. below 10 $m^2\ g^{-1}$, is preferred, as this will reduce the first cycle ICL and excessive electrolyte decomposition.[26] Another proven approach is through surface modification of the graphite edge planes, as the SEI thickness is three to five times greater at the more reactive edge planes compared to at the basal planes.[27] Hence, the first cycle ICL can be reduced with surface modifications mitigating the initial electrolyte decomposition at these exposed planes.

Different from altering the characteristics of the graphite particles, the addition of film forming additives to the electrolyte can reduce the first cycle ICL. Small amounts of carbonates such as fluoroethylene carbonate (FEC)[28] and vinylene carbonate (VC)[29] are often added to the electrolyte, and are either reduced before the electrolyte and/or limit the reduction of other electrolyte components. Consequently, less of the active charge carriers, i.e. the Li-ions, in the electrolyte are consumed in forming the SEI layer.[11]

In addition to the initial SEI formation, changes in the SEI morphology and composition may occur upon cycling and storage, which poses critical safety issues.[11] The most destructive factor is that of elevated temperature, since the SEI layer starts to decompose at approximately 90 °C, depending on the system. Further increase in temperature to 250 °C will initiate complete breakdown of the SEI and/or decomposition of the electrolyte, and then a thermal runaway of the battery.[11,30] This issue has been tried to handle with the development of more stable electrolytes and advanced surface modified graphite materials that reduce side reactions, as well as implementation of battery management systems that monitor the health of the battery. Another closely linked safety issue is Li plating, which will be discussed in the subsequent section.

2.6 Lithium Plating on Graphite Anodes

The graphite anode has to be developed with special attention targeted to its fast charging abilities, due to the ever increasing demands and expectations from car manufactures and customers on reducing the charging time for EVs. When a battery is to be fast charged, e.g. 80% SOC in less than 15-20 minutes, there is an increased risk of Li plating and other degradation mechanisms.[6,11] This section reviews the main factors, mechanism, and consequences of Li plating. In addition, methods for Li plating mitigation and detection will be presented.

2.6.1 Mechanism and Triggering Factors

Literature describes Li plating as the reduction of Li-ions to Li metal on the anode surface, i.e.

$$\mathrm{Li^+ + e^- \rightleftharpoons Li}$$

and Li stripping as the reversed reaction with oxidation of Li metal into Li-ions again. The term "metal plating" is defined as a homogeneous film covering a surface. Thus, the broader term "Li deposition" is sometimes utilised by researchers in order to also include local and marginal reduction of Li-ions, as Li plating on graphite anodes does not necessarily occur homogeneously.[31] In fact, the intercalation/deintercalation and plating/stripping of Li have been observed experimentally to occur in parallel and to different extents, as illustrated schematically in Figure 2.7.[32]

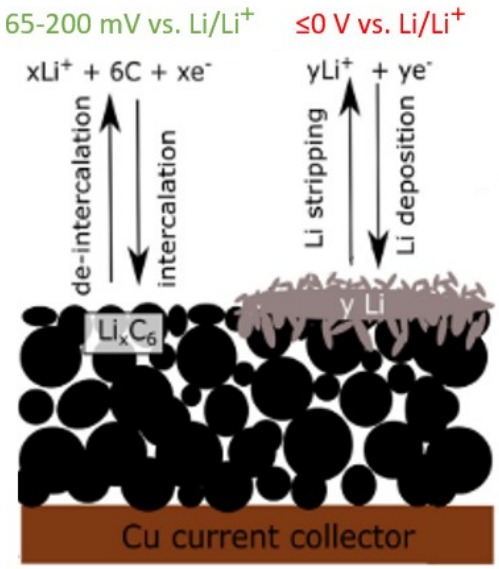

Figure 2.7: Illustration of the desired Li-ion reaction of intercalation/deintercalation into graphite and the undesired reaction of Li plating/stripping. Figure adapted from Waldmann et al.[31]

Li plating does not pose a great risk in theory, since Li-ions intercalate into graphite in the potential range of 200 to 65 mV vs. Li/Li^+ and Li plating only becomes thermodynamically possible below 0 V vs. Li/Li^+.[33] However, polarisation of the anode surface can be imposed under non-ideal circumstances, which may lead to a negative cell potential vs. Li/Li^+ and thus Li plating. Waldmann et al.[31] summarise the main factors triggering a decreased anode potential and thus an increased risk of Li plating as

- increased SOC
- increased charging C-rate
- low temperatures

In order to understand how these three factors are among the main culprits provoking Li plating, it is important to understand the mechanism behind diffusion and transport of Li-ions. The intercalation process and the corresponding energy barriers at the atomic scale are illustrated in the top and bottom of Figure 2.8, respectively. The energy barrier in the liquid phase is rather low compared to the charge transfer barrier, as the latter involves transport through the SEI layer and electron transfer. The final step is the solid diffusion of Li-ions between the graphene layers, which is limited by an energy barrier in the range of 0.22-0.36 eV.[31]

The solid diffusion energy barrier increases with an increased concentration of Li in the graphite structure, i.e. increased "x" in Li_xC_6.[34] This is the main explanation for why an increased SOC negatively affects the risk of Li plating.[31]

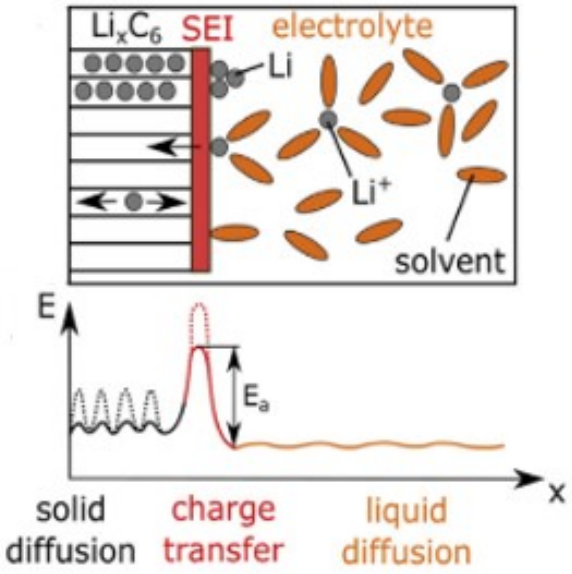

Figure 2.8: Illustration of the intercalation process on the atomic scale (top) and the involved energy barriers (bottom). Figure adapted from Waldmann et al.[31]

According to the Arrhenius law, the charge transfer at the graphite interface and the diffusion of Li-ions are slowed down at lower temperatures, and Li plating takes precedence over intercalation. Consequently, the probability of overcoming the energy barrier for intercalation decreases, i.e. $\propto \exp(-E_a/(k_B T))$. Additionally, at lower temperatures, the conductivity of the electrolyte decreases, which slows down the chemical intercalation of Li into graphite.[31]

Increasing charging C-rates result in higher current densities on the macroscale, which translates to higher Li-ion flux per anode area on the atomic scale. Taking into consideration that the diffusion of intercalated Li-ions from the graphite surface to inside is driven by concentration gradients, it is known that Li plating may occur when this transport is slow.[31] This is because the increased current and poor diffusion lead to higher overpotentials, as shown in Equation 2.5 previously, which increase the possibility of plating. The electrode edges are particularly vulnerable to Li deposition and dendritic growth, due to the non-uniform current distribution that leads to a higher field at the electrode edge.[35] Consequently, such areas are at greater risk of Li deposition and dendritic growth, especially when high current densities are applied.[36]

Therefore, the main mechanisms behind Li plating are the too slow intercalation rate of Li-ions into the graphite structure and/or a very high transport rate for Li-ions to the electrode surface. Additionally, both mechanisms increase the resistance towards the transport of Li, and one risks that the ohmic loss becomes too large so that the potential on the anode surface drops below 0 V.[9] Nevertheless, the interplay between these factors is also important.[31] By applying low charging currents or preheating the battery, for example, the risk of plating caused by slow diffusion at lower temperatures can be reduced. Similarly, it is possible to charge a cell with high currents at low SOC and then with lower currents at higher SOC without the occurrence of Li plating.[31]

2.6.2 Consequences

Li plating is detrimental for the integrity of the cell as well as posing a safety hazard. It is possible for metallic Li to lose electrical contact with the anode during the stripping process upon discharge of the cell, resulting in so-called "dead Li". This leads to a direct loss of active Li in the cell as well as additional SEI growth, which results in an irreversible capacity loss and energy efficiency degradation. Additional capacity loss can result from pore clogging and increased cell impedance caused by film formation of Li metal and/or a thicker SEI layer.[31] Figure 2.9 illustrates these negative consequences of Li plating with the formation of "dead Li" and the generation of new SEI. In addition, the figure illustrates the more desirable scenarios of reversible Li plating with the stripping occurring upon discharge and the chemical intercalation upon rest.[37]

Moreover, dendritic growth of Li metal may occur upon plating, resulting in a risk of puncturing the separator. This, in turn, may cause a short-circuit and consequent heat generation in the battery. Additionally, the "dead Li" may react with the electrolyte, and such exothermic reactions will also lead to heat generation. In cases of inadequate heat dissipation, the heat generation can spiral out of control, leading to a thermal runaway of the battery. This poses a great safety threat to nearby humans and a material cost linked to the possible damages caused by a battery fire or explosion.[31] In this way, it is important to develop graphite that mitigate the risk of plating.

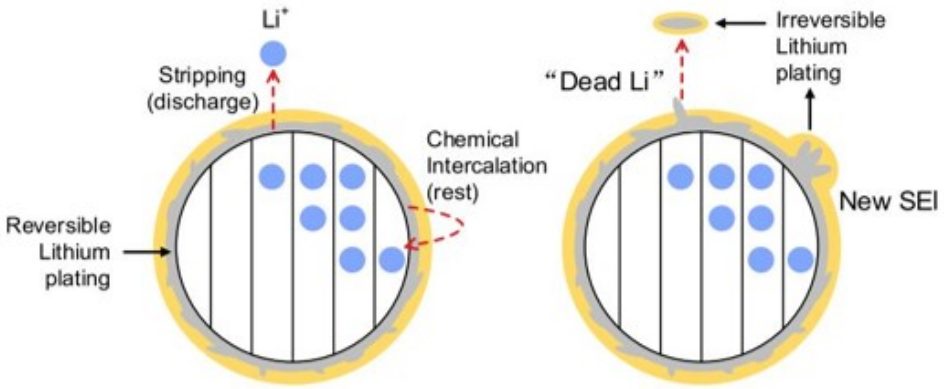

Figure 2.9: Illustrations of the possible processes related to reversible (left) and irreversible (right) Li plating. Figure adapted from Tian et al.[37]

2.6.3 Surface Modifications for Mitigation of Plating

Ever since the commercialisation of the LIB with the graphite anode in 1991,[3] tremendous efforts have been put into improving the electrochemical performance of graphite.[38] Some of the most explored modifications include reducing the particle size, making a graphite/nanopowder composite, oxidising the surface, or applying a coating.[38] In particular, many researchers have shown that amorphous carbon coating improves the cycling performance and rate capability, where the latter is key for mitigating Li plating.[38–41] In addition, amorphous carbon is both relatively cheap and environmentally friendly compared to other coating materials, such as polymers and metals.[26]

The main culprit of graphite is the poor Li-ion diffusion across the electrode/electrolyte interface, i.e. the desolvation of ions at the anode interface, compared to diffusion within the electrolyte and the graphite planes.[40] This is mainly due to the high anisotropy of graphite, as the energy barrier for intercalation is much lower at the edge planes compared to the basal planes where intercalation is impossible except for at defect sites. Differently, amorphous carbon has an isotropic structure that increases the diffusion channels of Li-ions and facilitates increased transport of Li-ions to the edge planes of the graphite particles when coated in a thin layer around the graphite particles. In this way, the ohmic resistance and polarisation of the surface are reduced, and thereby also the risk of plating.[38,39,42]

Carbon coating will also reduce the specific surface area, due to coverage of pores and defects and a slightly larger particle size. This reduces the first cycle ICL and excessive electrolyte decomposition, as discussed in Section 2.5.3. Figure 2.10 illustrates this schematically where the carbon coated graphite clearly has a denser and thinner SEI layer compared to the pristine. This is also beneficial for the mitigation of plating, as the resistance in the SEI will be lower, resulting in reduced polarisation at higher charging rates.[26,38,42]

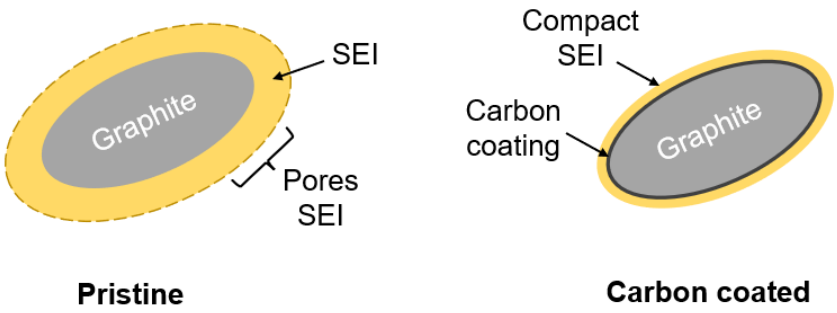

Figure 2.10: Illustration of a pristine (left) and carbon coated (right) graphite particle. Figure inspired from Natarajan et al.[43]

The amount of carbon coating should be optimised by considering several factors. For instance, excessive coating will not only reduce the energy density with the additional mass of an inactive component, but also increase the diffusion distance of Li-ions. The latter will affect the rate capability, as it increases both electronic and ionic resistance.[38] On the other hand, an incomplete coating layer will lead to exposure of the graphite particle and possible exfoliation, of which neither is beneficial.[38] Therefore, one should optimise the amount of coating in order to achieve proper coverage of the graphite particles without negatively affecting the rate capability, and hence the ability to mitigate plating.

2.6.4 Detection and Characterisation of Plating

It is necessary to detect Li plating on graphite anodes in order to improve their fast charging capabilities. Today, there are no direct techniques for detecting the occurrence of plating in commercial cells, only indirect signs such as premature ageing behaviour with rapid capacity and CE losses. This is not a secure way of detecting Li plating, as side reactions in the electrolyte also degrade the cell over time. In contrast, in a half cell with a Li metal counter electrode or in a three-electrode cell with a Li metal reference ring, it is possible to monitor the potential of the graphite electrode and detect the occurrence of plating if the graphite potential falls below 0 V vs. Li/Li^+.[31,37,44] This detection principle is illustrated in Figure 2.11.

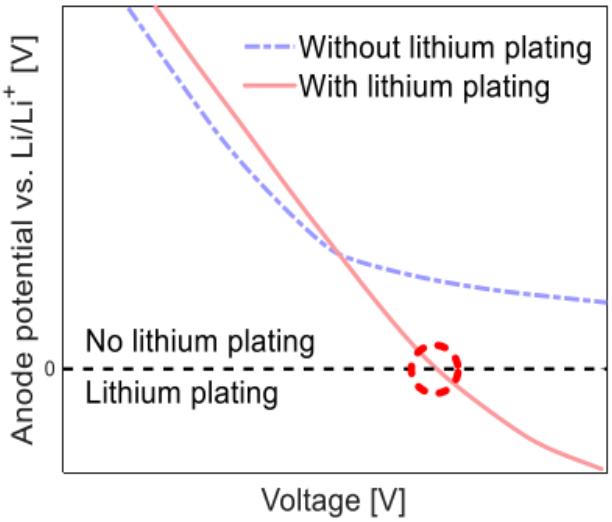

Figure 2.11: Illustration of the principle of detection of plating by anode potential measurements. The red circle highlights the occurrence of plating. Figure adapted from Tian et al.[37]

In addition, it is possible to reveal the occurrence of plated Li by investigating the potential curves upon discharge of the cell. The work of Smart and Ratnakumar,[45] for example, has demonstrated a correlation between Li plating and the discharge potential curve plateauing after charging at low temperatures, i.e. after imposing plating. Additionally, it was observed that the plateau increased with increased amounts of imposed plating. The stripping reaction is a more facile reaction compared to deintercalation, and it will appear as a voltage plateau as a result

of the phase equilibrium between oxidation of plated Li metal and the first deintercalation of graphite.[46] Thus, the authors linked this initial plateau at a lower potential to the stripping of reversibly plated Li.

In order to quantify the amount of plated Li with increased preciseness, the potential curve including the stripping plateau can be made into a differential capacity plot, as proposed by e.g. Petzl and Danzer.[46] In their work, plating was imposed by charging at temperatures down to $-20\,^{\circ}\mathrm{C}$ before the reversible plating was quantified by investigating the differential capacity plot. Here, a distinct peak corresponding to the discussed voltage plateau was visible. The authors concluded that the charge delithiated until the potential of this peak almost solely could be denoted the stripping reaction, i.e. $Q_{rev.plating}$. However, as discussed, the stripping reaction will only account for the reversible plated Li and not possible irreversible plating that results in "dead Li". This irreversible amount plated can be estimated from the capacity loss in the cycle with imposed plating, which equals the difference between the amount charged and discharged, i.e.

$$Q_{irrev.plating} = Q_{ch} - Q_{dc}$$

The amount of irreversible plating has also been found to correlate to the SOC at the point of plating. At a higher SOC, the plating reaction is even more favourable than intercalation compared to at lower SOC, as discussed in Section 2.6.1. This leads to more excessive plating, but also increased film formation as the Li metal may grow past the SEI layer and react with the electrolyte. Upon discharge, there is a large probability for these deposits to lose electrical contact from the electrode, thus resulting in "dead Li" and irreversible plating.[46]

By adding the reversible and irreversible amounts one can determine the total amount of charge that has been plated, i.e.

$$Q_{plating} = Q_{rev.plating} + Q_{irrev.plating}$$

However, it should be noted that this only provides an estimate, as possible film formation on "dead Li" is not distinguishable from irreversible plating.[46] Nevertheless, this contributes to an irreversible capacity loss originating from plating, which not necessary would have taken place without the occurrence of plating.

Several post mortem characterisation techniques have been evaluated for detection of Li metal on graphite anodes. However, a few negative aspects must be mentioned; post mortem techniques cannot provide in situ detection of the plating's degradation processes with need for disassembly of the cell, and the plated Li may chemically intercalate upon rest before disassembly. Hence, the cells should be opened shortly after the end of cycling.[31,46]

One common technique for detection of metal elements, including Li, is glow discharge optical emission spectroscopy (GD-OS) depth profiling. Yet, the GD-OS method can only determine the amount of Li metal from the amount of LiO_2. Thus, it can only be regarded as a semi-quantitative method for detecting Li plating, as one has to assume that all Li metal has been oxidised after exposing the anode to air prior to the analysis.[31,47] Moreover, there is some Li present in the SEI layer in the form of Li_2CO_3, LiF, and Li_2O, due to the reduction of Li salts in

the electrolyte. Despite these drawbacks, Ghanbari et al.[47] successfully characterised Li plating with GD-OS. Figure 2.12 presents their results. Local areas assumed to be Li metal, referred to as "islands", showed higher mass-% of Li compared to areas without such "islands" and a non-cycled graphite electrode. Additionally, the electrodes were imaged using SEM, prior to the GD-OS analysis. Here, the assumed plated areas appeared with a dendritic morphology in contrast to the graphite particles of the non-cycled electrode and areas without plating. Thus, SEM can also be used as a tool for investigating Li plating and for verifying the results of element analysis techniques such as GD-OS.[47]

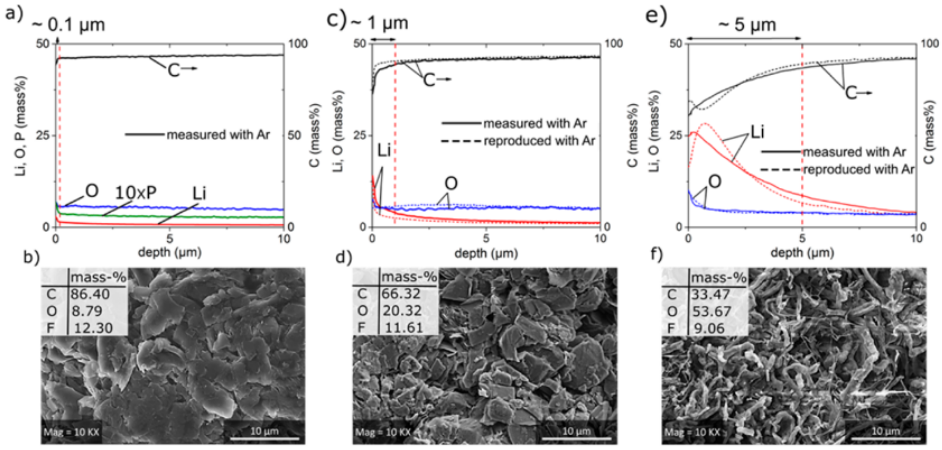

Figure 2.12: Results of GD-OS analysis for a) a non-cycled electrode, c) cycled electrode without Li plating, and e) cycled electrode with Li plating, with respective SEM micrographs in b), d), and f). Figure adapted from Ghanbari et al.[47]

Additionally, SEM has been used to reveal two different morphologies of plated Li metal, i.e. dendrites and mossy structures. These have been found to correlate to the C-rate of the plating; high charging currents ($\sim$1C) lead to the formation of relatively thick dendrites with a limited distance from the electrode surface, and low charge currents ($\sim$C/5) lead to a mossy structure that is more porous and dispersed.[46,48]

The element analysis energy disperse X-ray spectroscopy (EDS) is often used in combination with morphology analysis in SEM. However, Li is too light for being detected by EDS, and consequently this technique cannot provide direct evidence of Li plating. The detection of backscattered electrons may be used to obtain Z-contrast images that reveal the composition of the sample, i.e. with heavier and lighter elements appearing as brighter and darker areas, respectively. Though, with Li and C being relatively close in the periodic system, this may not be the most solid technique for detecting Li plating either.[31,47] In general, evidence of plated Li tends to be slightly difficult to obtain through post mortem characterisation, as Li is present in the SEI layer and most techniques cannot detect Li in its elemental form.

2.7 Electrochemical Characterisation Techniques

2.7.1 Galvanostatic Cycling

Galvanostatic cycling is a common technique for assessing the capacity, CE, stability, and rate capability of the electrode materials. A constant current equivalent to a specified C-rate is applied to the cell and the voltage response is recorded.[49]

2.7.2 Cyclic Voltammetry

CV involves the application of a triangular voltage on the electrochemical system at a given scan rate (mV s^{-1}) while recording the current response. Figure 2.13a illustrates the voltage profile where the upper E_2 and lower E_1 potential limits are determined from the working potentials of the battery. The resulting output can be presented in a so-called cyclic voltammogram with the current plotted against the potential, as illustrated in Figure 2.13b. Normal convention is that all positive-going currents are anodic and negative-going currents are cathodic. The peak voltages, such as E_{pa} and E_{pc}, correlates to specific electrode reactions, and a shift in such peaks indicates polarisation of the electrodes. In this way, CV is sensitive to changes in the kinetics of electrode reactions, and can be used to analyse the effect of e.g. plating.[49]

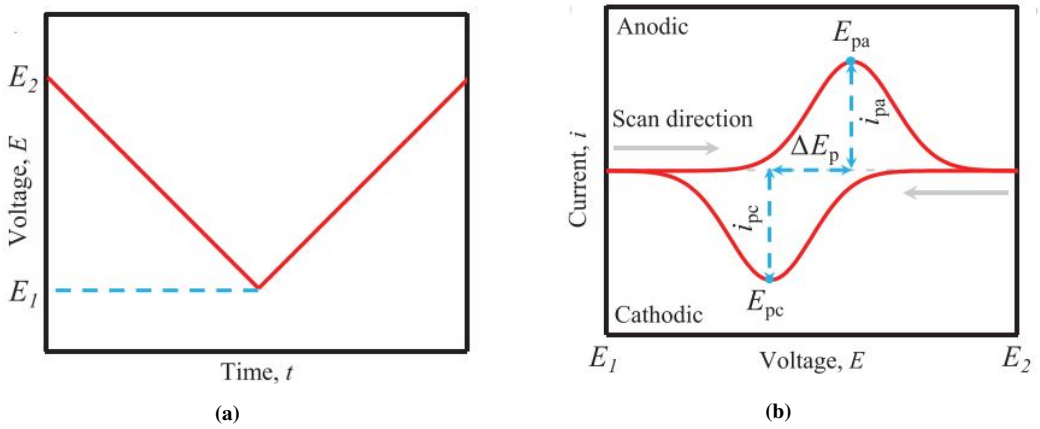

Figure 2.13: (a) Voltage profile applied and (b) resulting voltammogram in a CV measurement. Figures adapted from Yang and Rogach.[49]

2.7.3 Electrochemical Impedance Spectroscopy

EIS allows for analysis of kinetic characteristics of electrochemical systems, e.g. diffusion coefficients, rate constants, and ohmic resistance in the electrolyte.[49,50] In this way, one can characterise possible degradation of the cell by comparing EIS measurements performed e.g. after different amounts of cycles or before and after a cycle with imposed plating.

The principle of EIS is to apply an alternating signal over a range of frequencies to the cell, and observe the following reaction at the steady state. The voltage excitation must be low to ensure a linear behaviour. There are mainly two different techniques based on the type of signal applied; potentiostatic EIS (PEIS) and galvanostatic EIS (GEIS) where the potential and the current is controlled, respectively.[50]

The most common plots that visualise the impedance spectrum are Nyquist and Bode plots. The Nyquist plot illustrates the imaginary part ($-Im(Z)$) against the real part ($Re(Z)$) of the impedance, which is given as $Z(j\omega) = Re + jIm$. Here, $\omega = 2\pi f$ and is the circular frequency derived from the usual frequency f, and $j = \sqrt{-1}$ and is the imaginary number. The shape of the Nyquist plot gives information about the system at hand, and by fitting the data by an equivalent circuit the impedance related to different electrochemical processes in the system can be derived. Similarly, the Bode plot illustrates the different processes occurring at the different frequencies in the system by plotting $Re(Z)$ and $Im(Z)$ separately against $\log(\omega)$.[50]

Figure 2.14a illustrates a typical Nyquist plot and the corresponding equivalent circuit, known as the Randles circuit. The elements depicted are the internal, ohmic resistance (R_{int}), the double layer capacitance (C_{dl}), the charge transfer resistance (R_{ct}), and the Warburg impedance (Z_W). These represent the impedance related to specific electrochemical processes occurring at the electrode, as the processes can be estimated to occur at certain frequencies.[49] For example, R_{int} is the starting point, i.e. at the highest frequencies, R_{ct} equals the diameter of the semicircle, and a resistor in parallel with a capacitor will appear as a semicircle. At low frequencies, the double layer capacitance is negligible, which appears as a slope with a 45° angle, and the resulting impedance originates from the Warburg element.[49,50]

Figure 2.14b illustrates the case where the capacitor is replaced with a constant phase element (CPE), which is a non-ideal form of the capacitor. The purpose of this is to better fit the spectrum whose semicircle at high frequencies appears depressed due to the overlay of multiple RC-circuits, and whose slope at low frequencies deviates from 45°.[49]

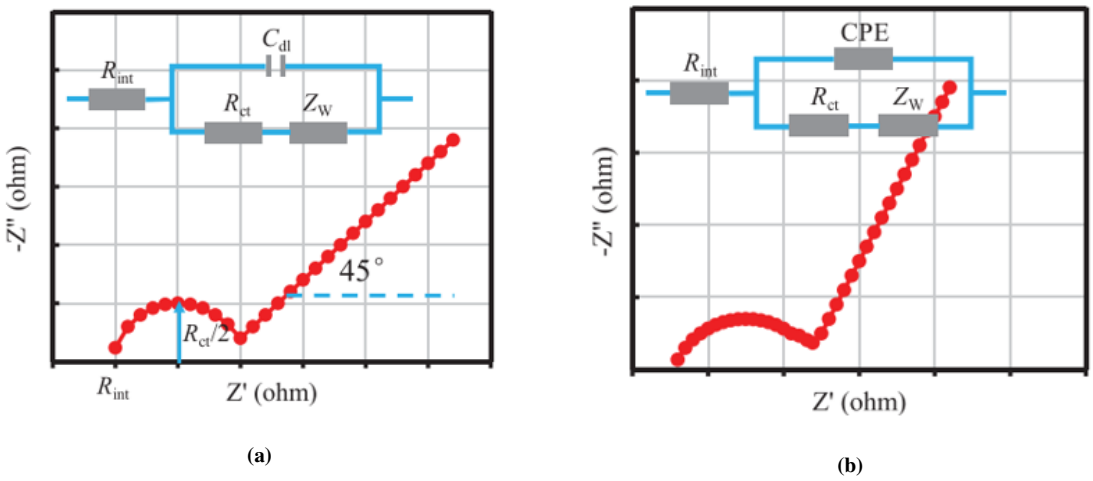

Figure 2.14: (a) Randles circuit and (b) Randles circuit with CPE. Figures adapted from Yang and Rogach.[49]

Table 2.1 provides an overview of some of the most common circuit elements, such as R, C, CPE, and W (infinite Warburg). In addition, two alternative types of the Warburg impedance are included, i.e. finite Warburg open (Wo) and finite Warburg short (Ws). The finite Warburg elements describe the diffusion of electroactive species in a geometrically limited space, which is the case for graphite particles.

Table 2.1: Equations and descriptions of common circuit elements.[49,50]

Name	Symbol	Equation, Z =	Description
Resistor	R [Ω]	R	Resistance of resistor
Capacitor	C [F]	$\frac{1}{i\omega C}$	Capacitor
Constant phase element	CPE (Q) [F $s^{\alpha-1}$]	$\frac{1}{Q(i\omega)^{\alpha}}$	Non-ideal capacitor Q [F $s^{\alpha-1}$]: admittance α [-]: exponential factor (0-1)
Infinite Warburg	W [Ω]	$\frac{A_W}{\omega^{0.5}}$ $-i\frac{A_W}{\omega^{0.5}}$	Linear diffusion towards an electrode Straight line at angle = 45° A_W [Ω $s^{-0.5}$]: Warburg coefficient
Finite Warburg (open)	Wo [Ω]	$\frac{Z_W}{(i\omega\tau)^{\alpha}}$ $coth((i\omega\tau)^{\alpha})$	Max length of diffusion is limited Straight line at angle > 45° Z_W [Ω $s^{\alpha-1}$]: Warburg coefficient τ [s]: time-constant α [-]: exponential factor (0-1)
Finite Warburg (short)	Ws [Ω]	$\frac{Z_W}{(i\omega\tau)^{\alpha}}$ $tanh((i\omega\tau)^{\alpha})$	Max length of diffusion is limited and concentration of diff.species is replenished to a constant level Straight line at angle < 45° Z_W [Ω $s^{\alpha-1}$]: Warburg coefficient τ [s]: time-constant α [-]: exponential factor (0-1)

2.8 Materials Characterisation Techniques

2.8.1 Particle Size Distribution

The particle size distribution (PSD) and mean diameter of a powder can be determined by laser diffraction. This is based on the knowledge that particles scatter light with a certain intensity and angle determined by its size, i.e. smaller particles scatter weakly at small angles and large particles more intense at wide angles. The laser diffraction instrument consists of at least one source of high intensity, monochromatic light, a sample handling system, and several photodiodes that detect the scattered light over a wide range of angles. The angles and intensities of scattered light are recorded, and the PSD is determined with the use of an optical model based on the Mie scattering theory. Certain assumptions are made in the model; the particles are spherical, the ensemble is homogeneous, and the refractive index of the particle and surrounding medium is known. This means that the reported value is actually an equivalent spherical diameter, which has been calculated by determining the size of the sphere that could produce the diffraction data. This should be kept in mind when analysing PSD data of powders of more irregularly shaped particles, as the technique is less precise when determining the size of particles with a high aspect ratio.[51]

2.8.2 Gas Adsorption Measurements

Gas adsorption measurements constitute important techniques for deriving the surface area and pore size distribution of porous materials. Generally, nitrogen gas is adsorbed at 77 K, which results in adsorption data, such as isotherms, that can be used to retrieve information about the material at hand through various methods. The BET method from 1938 has been established as a standard procedure for determining the specific surface area. The BET theory assumes a closed-packed state of the completed monolayer of adsorbed gas on the material, and determines the specific surface area by recognising the point of transition from monolayer to multilayer adsorption. The amount of gas adsorbed until this point is found by measuring the change of gas pressure, which then is used to calculate the surface area. In addition, the type of pore structure can be found by examining the nitrogen isotherms. More specifically, the amount of micropore area and/or external area can be determined. These are the areas of pores with diameter smaller than and larger than 2 nm, respectively, and the sum of micropore and external area gives the total BET surface area.[52]

2.8.3 Scanning Electron Microscopy

SEM enables characterisation of the surface of a material on the microscale. A focused electron beam emits electrons that hit the sample surface resulting in various sets of signals that can be detected. Secondary electrons (SEs) are a result of inelastic interactions between the electron beam and the surface and near-surface regions of the sample. Hence, SEs provide information about the topography of the material and the detection of them gives a detailed image of the surface morphology. Another type of electrons that can be detected are backscattered electrons (BSEs), which are electrons that have been reflected back after elastic interactions between the electron beam and deeper regions of the sample. The BSEs carry information about the atoms in the sample, as larger atoms with higher atomic numbers will scatter electrons much stronger than light atoms with lower atomic numbers. In this way, BSE images can be used to obtain information about the composition of the sample, as atoms with higher atomic numbers will appear brighter compared to atoms with lower atomic numbers.[53]

2.8.4 Focused Ion Beam

The focused ion beam (FIB) is an ion beam that can be utilised for deposition and manipulation of structures. Positive ions, normally Ga-ions, are emitted from a sharpened tungsten needle by applying a high voltage. The FIB has a small beam spot with a diameter from 10 to 100 nm and a high current density greater than 10 A cm^{-2}.[54] In this thesis, the micro-machining capability of the FIB will be utilised to obtain cross sections in sample surfaces.

3 Experimental

3.1 Overview

The experimental work can be divided into four main parts; active materials characterisation, electrode and cell manufacturing, electrochemical testing, and post mortem characterisation. The objective of the active materials characterisation was to see whether the graphite powders differed in morphology, PSD, or specific surface area. These techniques are presented subsequently. In addition, the electrode and cell manufacturing section contains the methods for slurry mixing and tape casting, as well as for coin cell and PAT cell assembly. The cycling parameters used in the electrochemical tests are also presented. Lastly, details regarding the post mortem characterisation of the cycled electrodes with SEM and FIB are included.

3.1.1 Graphite Powders

Two different powders of synthetic graphite provided by Vianode were investigated in the experimental work of this thesis, i.e. a pristine graphite powder without surface modifications (Vianode serial number: S-210923-002593) and a surface modified graphite powder (Vianode serial number: S-211126-002931). The powders will be referred to as "the pristine powder" and "the modified powder", respectively, for the remainder of this thesis. The modified powder is obtained through surface modifying the pristine powder, which among other things includes coating it with amorphous carbon. However, more extensive information about the type of surface modification or process behind could unfortunately not be disclosed by Vianode, due to company regulations.

3.2 Active Materials Characterisation

3.2.1 Morphology

SEM was used to characterise the morphology of the graphite powders. A small amount of powder was collected with a carbon tape on a SEM holder. The working distance (WD) was set to approximately 10 mm before applying an accelerating voltage of 10 keV and detecting the SEs. The instrument used was a Zeiss SUPRA 55-VP FEGSEM.

3.2.2 Particle Size Distribution

The PSD of the pristine and modified graphite powders were estimated by laser diffraction using a Horiba Partica LA-960 particle size analyser. The graphite was added to the instrument filled with isopropanol until a transmittance of approximately 90% was reached. Then, the solution was sonicated for 2-3 minutes to break up any agglomerates before carrying out the measurement. This was repeated two times to ensure a reproducible result. The refractive index of carbon of 1.92 was used for both powders. Laser diffraction is a volume based technique that assumes perfectly spherical particles, which should be kept in mind when evaluating the experimental data.

3.2.3 Specific Surface Area

Nitrogen adsorption (BET) analysis was used to determine the specific surface area of the two graphite powders. Approximately 1.5 g of the powders were weighed out and transferred in glass test tubes. Then, they were heated and degassed in inert nitrogen with a degassing apparatus (Degas Smartprep, Micromeritics) to remove moisture. Table 3.1 shows the degas heating programme. The test tubes were weighed again after the degassing. Filler rods on the inside of the test tubes were used to reduce the area, and isothermal jackets were applied to the outside to minimise the temperature gradients in the samples. The test tubes were then mounted onto the nitrogen adsorption apparatus (3Flex 3500, Micromeritics). Lastly, the samples were evacuated and cooled in liquid nitrogen before the initiation of the BET analysis.

Table 3.1: Degas heating programme before the nitrogen adsorption analysis. The temperature ramp rate was 10 °C min^{-1} in all the steps.

Step	Temperature [°C]	Time [min]
1	30	10
2	90	60
3	250	1000
4	30	100

3.3 Cell Manufacturing

3.3.1 Slurry Mixing and Tape Casting

The graphite electrodes were manufactured by tape casting a homogeneous slurry onto a Cu current collector. The target slurry composition was 2 wt% CB (C-NERGY SUPER C45, Imerys), 1.5 wt% SBR (Targray), 1.5 wt% CMC (Daicel), and 95 wt% graphite (Vianode). The CB acts as a conductive additive, the SBR and CMC are binder materials, and the graphite is the active material in the electrode. Deionised (DI) water was used as a solvent to obtain good mixing, a homogeneous slurry, and a specific loading, i.e. amount of active material per area, of the final electrodes.

A CMC solution (1.5 wt% CMC) was prepared by dissolving the CMC powder in DI water to reduce the mixing time for each new slurry that was made. The SBR binder solution was used as-received from the manufacturer and had a composition of 15 wt% SBR.

To make a slurry sufficient for approximately one tape cast, 3 g of active material was needed. 0.0600 g of CB was weighed out in a mixing jar and added to 3.0007 g of the prepared CMC solution. The CB and CMC solution were mixed in a vacuum centrifugal mixer (TMAX-TP300S) for approximately 10 minutes without vacuum. Then, DI water was added according to a target solid/liquid ratio and mixed for 5 minutes without vacuum and 2 minutes with vacuum. Mixing with vacuum was important to properly disperse the CB nanoparticles in the solvent. 2.8500 g of graphite was then added and mixed with and without vacuum for approximately 15 minutes in total. After ensuring that a homogeneous slurry without agglomerates was obtained, 0.300 g of the SBR binder solution was added and mixed at maximum 1000 rpm with and without vacuum for 5 minutes in total.

The slurry was then casted onto a Cu foil with a tape caster (K Control Coater) using a meter bar with a height of 150 µm. Then, the cast was dried at 60 °C in air for approximately 5 hours before being ready to be cut out into electrode disks.

3.3.2 Coin Cell Assembly

Electrode disks were cut out from the graphite tape cast using an electrode cutter with a diameter of 16 mm. Their mass was then weighed with a 0.1 mg resolution, and the mass of the Cu foil was subtracted to obtain the mass of the active material. Then, the electrodes were dried overnight in a vacuum oven (Binder VD 23) at 120 °C and subsequently transferred into a glove box with argon atmosphere (MBraun Labmaster, H_2O and O_2 <0.1 ppm) where the coin cell assembly took place. In addition, 25 µm thick polypropylene (PP) separators (Celgard 2400) were cut out into 19 mm disks, dried for 5 hours at 60 °C in the vacuum drying oven, and transferred into the glove box.

Figure 3.1a illustrates schematically the coin cell assembly process. The order of assembly from bottom to top was the following: coin cell base, graphite electrode with current collector facing down, separator, coin cell gasket, 50 µL electrolyte, Li foil disk, spacer, and coin cell lid. The coin cell caps used were CR2016 by Hohsen Corp. The Li foil was cut out into 14 mm disks, polished with a brush to remove a possible oxide layer, and pressed onto the spacer. A 0.3 mm thick spacer was needed to enable good electrical contact between the coin cell caps and electrodes, as well as preventing the parts moving after assembly. The electrolyte (Solvionic) used was 1.2 M $LiPF_6$ in (3:7 wt%) EC : EMC with 2 wt% VC.

After assembly, the coin cell was crimped together using an automatic crimping machine (Hohsen Corp.). The final coin cell was left to rest for a minimum of 12 hours before cycling, to ensure that the electrolyte had time to completely wet the separator and electrodes.

3.3.3 PAT Cell Assembly

PAT cells from EL-Cell GmbH were used to run three-electrode cell experiments with Li metal as the counter electrode. Electrode disks with a diameter of 18 mm were cut out from the graphite tape cast using an electrode cutter. These were then weighed, dried overnight, and transferred into the glove box with the same procedure as in the coin cell assembly. The Li metal came as pre-cut disks with a 15.6 mm diameter and 0.6 mm thickness, and these were polished with a brush to remove the possible oxide layer. The insulation sleeve (EL-Cell GmbH) included a Li reference ring and a PP separator.

The PAT cell components, illustrated in Figure 3.1b, were transferred into the glove box where the assembly took place. First, the graphite electrode was placed in the bottom of the insulation sleeve with the lower plunger (200 µm height) securing it in place. Then, the insulation sleeve was put into the cell base together with the lower plunger in the bottom. 100 µL of the $LiPF_6$ electrolyte was added on top of the separator before adding the counter electrode, i.e. the polished Li metal disk, and the upper plunger. Finally, the screw cap with the sealing ring was placed on top of the cell base and locked, and thereby securing all of the three-electrode parts.

After assembly, the PAT cell was left to rest for a minimum of 12 hours before cycling, to ensure complete wetting of the separator and electrodes.

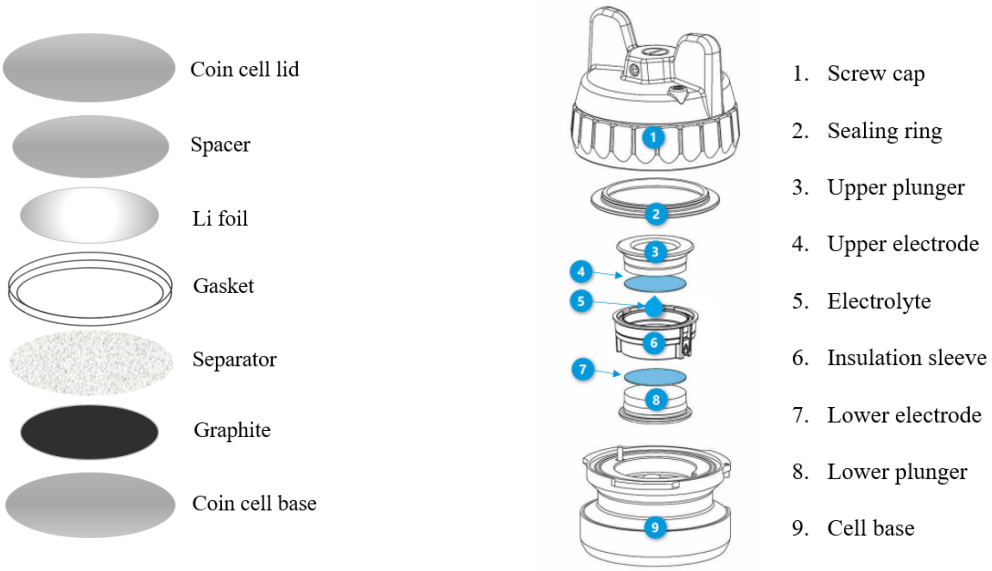

Figure 3.1: Assembly of (a) a coin cell and (b) a PAT cell (illustration adapted from EL-Cell GmbH[55]).

3.4 Electrochemical Testing

Three different electrochemical techniques were utilised; galvanostatic cycling, CV, and EIS, as described below. The battery tester used for the galvanostatic cycling was a BioLogic BCS-805, and the data processing software EC-lab V11.42 was utilised to obtain the differential capacity plots. The impedance spectroscopy was performed on a BioLogic VMP3 potentiostat. The temperature of the cycling room was 25 °C for all the tests. The C-rate was calculated using the theoretical capacity of 372 mAh g^{-1} for fully lithiated graphite (LiC_6). Further on, all the potentials are given with respect to Li/Li^+ unless otherwise stated.

In a half cell configuration consisting of Li metal and graphite, the graphite acts as the cathode (positive electrode) and Li metal as the anode (negative electrode). This is due to Li metal having a higher electrochemical potential than graphite. Hence, charge and discharge result in delithiation and lithiation of the graphite electrode, respectively. Since graphite is the main focus of this thesis, the more intuitive terms "delithiation" and "lithiation" are used when describing the cycling; delithiation occurring when Li-ions move out from the graphite structure, and lithiation when Li-ions move into the graphite structure.

3.4.1 Galvanostatic Cycling

The galvanostatic cycling comprises of programmes for the formation cycles, the reference cells, and two different programmes with imposed plating. Table 3.2 provides an overview of these cycling programmes. For the lithiation, a potentiostatic hold step was introduced after the galvanostatic lithiation to ensure a fully lithiated graphite. This is presented in the table with the cut-off voltage for the lithiation first, followed by the final C-rate for the hold step in parenthesis. The delithiation does not contain a hold step, and is simply ended by reaching a cut-off voltage of 1 V.

Three reference coin cells of each powder were cycled according to the "Reference" programme, in order to compare the specific capacity of the powders and for comparison with the cells undergoing plating. The "Plating" programme describes the general cycling of what will be referred to as the "coin cells plating tests". Two plating programmes were developed with the objective of imposing plating at different SOC of the graphite, i.e. 100% and 50% SOC. The plating programmes were named according to this criteria and the cycling parameters for both of them are presented in Table 3.3. The 100% SOC programme ensured that the graphite was fully lithiated in the first step before the plating was imposed. This was done by increasing the C-rate, i.e. from C/4 to 3C, which introduced an overpotential. This overpotential drove the cell potential below 0 V vs. Li/Li^+ where Li plating occurs. Then, the plating (and/or lithiation in parallel) proceeded until a charge corresponding to 40 mAh g^{-1} had been reached. The 50% SOC programme lithiated the graphite only until a SOC of approximately 50% was reached, which corresponded to a cut-off potential of 50 mV. The potential was held at this potential for 1 minute before the same plating step as for the 100% SOC programme was imposed. The delithiation step succeeding the plating was the same for both programmes. Both plating programmes were tested on the pristine and modified powder with two cells in each parallel.

Table 3.2: Galvanostatic cycling programmes for the initial formation cycles, reference cells, and the programme for the coin cells undergoing a cycle with imposed plating.

		Lithiation		Delithiation	
Programme	Cycles	C-rate	End (hold step)	C-rate	End (hold step)
Formation	2	C/30	5 mV (C/50)	C/30	1 V (-)
Reference	2	Formation			
	20	C/4	5 mV (C/40)	C/4	1 V (-)
Plating	2	Formation			
	5	C/4	5 mV (C/40)	C/4	1 V (-)
	1	Plating: 100% SOC or 50% SOC			
	5	C/4	5 mV (C/40)	C/4	1 V (-)

Table 3.3: A step-by-step description of the two different plating cycles for the coin cell plating tests, i.e. lithiation until 100% SOC or 50% SOC before imposing plating.

Plating prog.	Step	C-rate	End (hold step)
100% SOC	1. Lithiation	C/4	5 mV (C/40)
	2. Plating	3C	40 mAh g^{-1} (-)
	3. Delithiation	C/4	1 V (-)
50% SOC	1. Lithiation	C/4	50 mV (1 min)
	2. Plating	3C	40 mAh g^{-1} (-)
	3. Delithiation	C/4	1 V (-)

3.4.2 CV and EIS

CV and potentiostatic EIS was performed on three-electrode (PAT) cells, i.e. one pristine and one modified. CV was used to impose plating on the graphite electrodes and EIS to characterise the effect of plating on the cell impedance.

Figure 3.2 illustrates the cycling programme. The cells underwent the necessary formation programme (not illustrated in the figure), as well as one C/4 cycle before and after the set of CV and EIS measurements. CV was performed from 1 V to -50 mV with a scan rate of 0.1 mV s^{-1} for two cycles. Initially, a scan rate of 1 mV s^{-1} was tested, but this provided poorer results with high levels of noise. A total of two CV measurements were carried out with impedance spectra being collected before, in-between, and after. Prior to each impedance measurement, the cells were lithiated at C/10 until a cut-off voltage of 75 mV and kept here until a cut-off C-rate of C/30. This was to ensure stable and comparable cell kinetics at approximately the same SOC. After each EIS measurement, the cells were delithiated at C/4 until 1 V. The impedance data was fitted in RelaxIS 3 with the equivalent circuit illustrated in Figure 3.3.

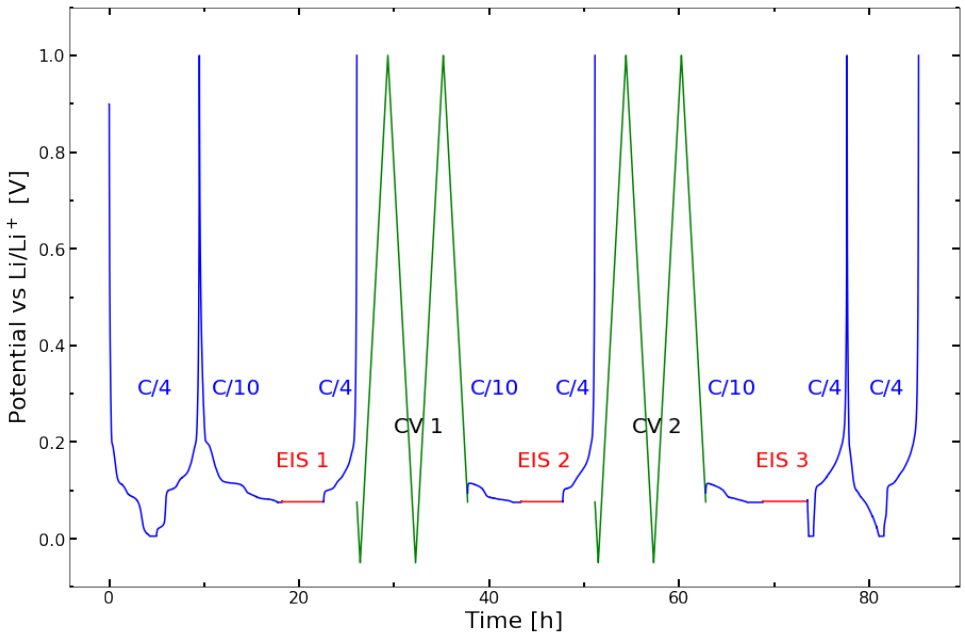

Figure 3.2: CV and EIS programme illustration.

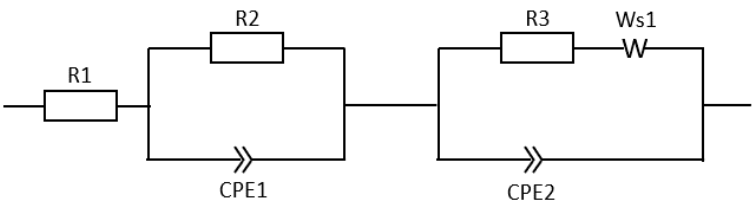

Figure 3.3: The equivalent circuit used to fit the impedance data.

3.5 Post Mortem Characterisation

3.5.1 Cell Disassembly

The cells were opened in a glove box shortly after completing the cycling. The PAT cells were opened by hand and the coin cells were opened using a coin cell disassembling tool (Hohsen Corp.). Immediately after the cells were opened, the electrodes were rinsed with DMC (Sigma-Aldrich) to remove Li salts and then left to dry for at least 30 minutes inside the glove box. The electrodes were photographed with a mobile phone to document and compare any visible degradation on the macroscale. When being transported from the glove box to the SEM/FIB, the electrodes were exposed to air for approximately 30 minutes. However, no excessive oxidation or transportation damages were visible in the microscopes.

3.5.2 SEM

One electrode from each parallel of the cycling programmes were characterised with a Zeiss SUPRA 55-VP FEGSEM. SEs were detected by applying an accelerating voltage of 10 keV to give a detailed image of the surface morphology of the electrodes. The WD was set to approximately 10 mm. In addition, BSEs were detected to obtain a Z-contrast image, which could provide information about variations in the elements present on the surface and possibly reveal plated Li metal.

The electrodes that underwent cycling programmes with imposed plating were imaged both along the edges and in the centre to optimise the chances for observing possible plated Li metal. In addition, one non-cycled electrode and one reference cycled electrode of each powder were imaged in order to compare possible consequences of cycling and imposed plating.

3.5.3 FIB

FIB provided the opportunity to investigate the bulk part of the electrode and possibly reveal remaining plated Li inside the graphite pores by making cross sections in the electrode surface. The FIB analysis was kindly performed by Inger-Emma Nylund (postdoctoral fellow, NTNU) at a FEI Helios G4 PFIB UXe DualBeam with FIB and SEM. This instrument can utilise both electrons and Ga-ions, which enable detailed imaging of morphology as well as manipulation or deposition of structures.

One non-cycled electrode and one electrode from the 100% SOC plating programme for each powder were analysed, and 1-2 cross sections were obtained and imaged for each sample. The cross sections made were approximately 30x30x30 µm in size. The sample stage was adjusted to eucentric height (ca. 4 mm) and tilted 52° to match the angle of the ion source for a perpendicular sputtering. An accelerating voltage of 30 kV was applied for the sputtering. To reduce the sputtering time, the sputtering function called "multipass cross section" and a higher emission current of 65 nA were utilised for the majority of the cut.

The final 5-10 µm were sputtered at a lower emission current of 9.1 nA with the "cleaning cross section" function for a finer and more detailed cut along the end edge. In addition, SEM was used to monitor the sputtering process and to image the area before and after making the cross sections. In this case, a WD of ca. 4 mm, an accelerating voltage of 3 kV, and an emission current of 50 pA was used.

4 Results

4.1 Overview

Firstly, the results from the active materials characterisation of the pristine and modified powders will be presented, which include SEM images of the graphite morphology, the median particle size, PSD, and the specific (BET) surface area. Secondly, a summary of the cell manufacturing with electrode compositions and average electrode loading is presented. Then, the results of the electrochemical characterisation are presented according to the two main types of cycling programmes, i.e. the coin cell plating tests and the CV test including the fitted EIS data. Lastly, the post mortem characterisation of cycled and non-cycled electrodes using SEM and FIB is presented.

4.2 Active Materials Characterisation

4.2.1 Morphology

Figure 4.1 depicts the SEM micrographs of the pristine and modified graphite powder. It can be observed at lower magnification in Figure 4.1a and 4.1b of the pristine and modified powder, respectively, that they are relatively similar in shape and size. The larger and more flat particles are ca. 15-20 µm long and 5-10 µm wide, while the smaller particles generally are more round in shape with diameters between 2 and 10 µm. Looking at the pristine and modified powder at a higher magnification in Figure 4.1c and 4.1d, respectively, it may be observed that the modified particles have a trend of having a slightly more round shape and that there is less of the more irregular and elongated particles.

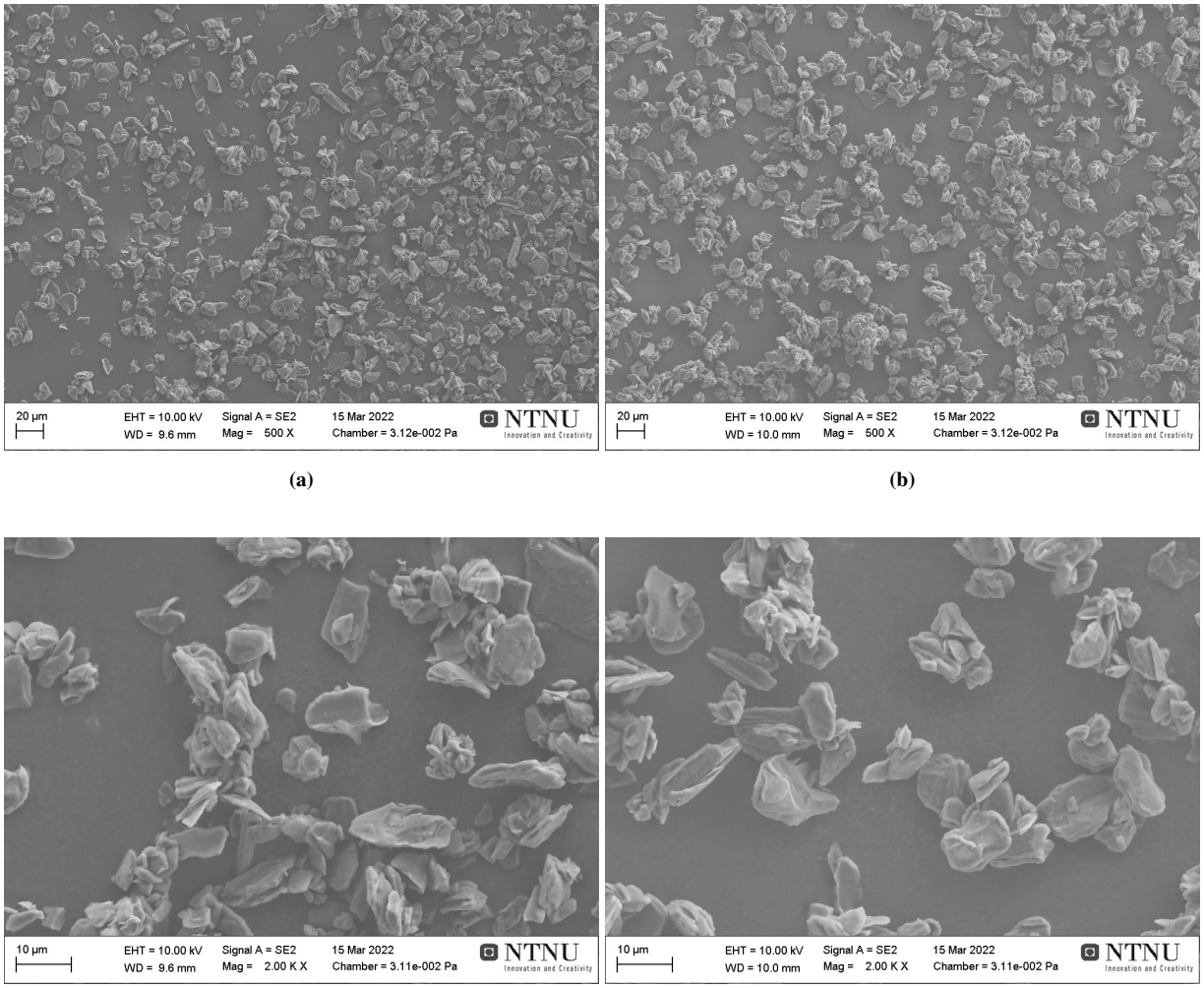

Figure 4.1: SEM micrographs of the pristine (a, c) and modified powder (b, d) at magnifications of 500 (a, b) and 2K (c, d).

4.2.2 Particle Size Distribution

The PSD of the pristine and modified powder obtained by laser diffraction is illustrated in Figure 4.2, and the median particle size is given in Table 4.1. Both powders can be said to be distributed in a monodisperse manner with the highest fractions located between 10 and 20 µm. The modified powder consists seemingly of larger particles, as its PSD curve is shifted rightwards and the median particle size is ca.1 µm larger compared to the pristine powder. However, it should be kept in mind that the laser diffraction technique assumes that the particles are perfect spheres, and not irregular in shape such as the more elongated graphite particles. This may provide an explanation for the relatively high standard deviation for the median, as both the length and width can be taken in as values for the diameter.

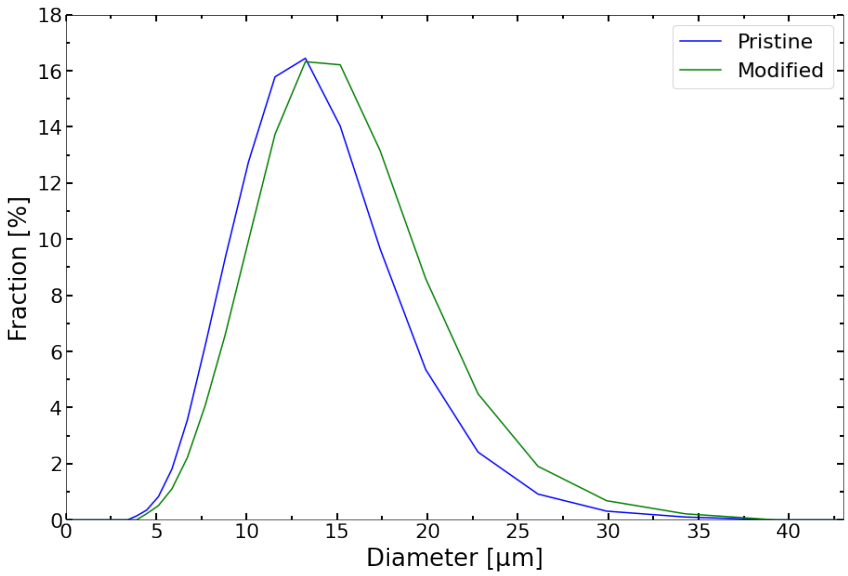

Figure 4.2: Particle size distribution of the pristine and modified powder from laser diffraction measurements.

Table 4.1: Median particle size of the pristine and modified graphite including the standard deviation ($\mu \pm \sigma$) obtained from laser diffraction measurements.

Powder	Median particle size [µm]
Pristine	11.49 ± 3.99
Modified	12.73 ± 4.37

4.2.3 Specific Surface Area

The results from the gas adsorption analysis are presented in Table 4.2. The pristine powder has a slightly larger specific (BET) surface area compared to the modified powder. In addition, Figure 4.3 illustrates the external and micropore surface area, which in total expresses the BET surface area. The micropore area is the area of pores with diameters smaller than 2 nm. Hence, it seems as the pristine powder has a more rough surface compared to the modified powder with zero micropores.

Table 4.2: Specific (BET) surface area of the two graphite powders.

Powder	Surface area [m^2 g^{-1}]
Pristine	1.2483 ± 0.0252
Modified	1.0392 ± 0.0026

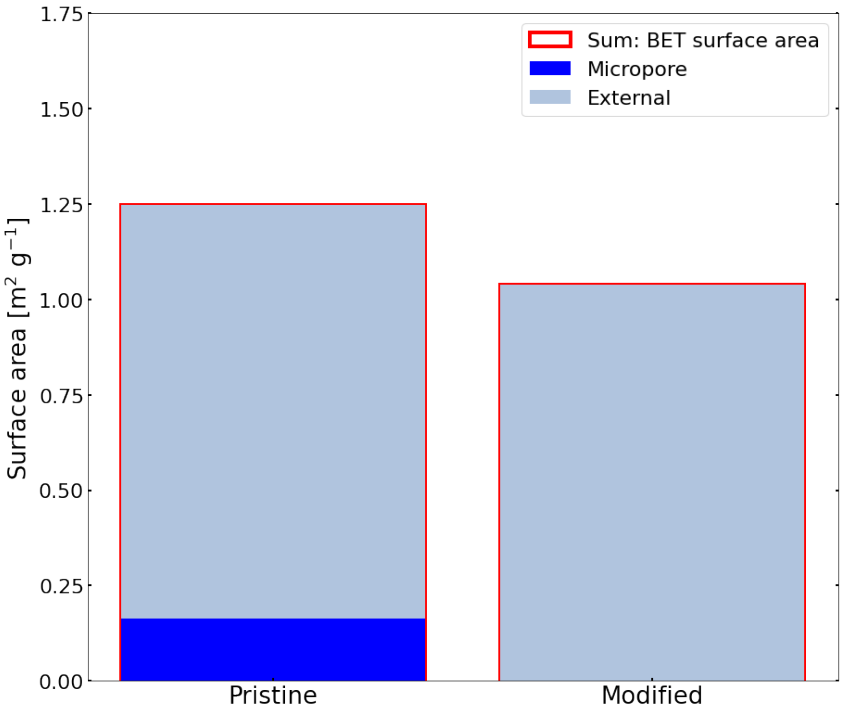

Figure 4.3: Micropore, external and BET surface area of the pristine and modified graphite powders.

4.3 Cell Manufacturing

Table 4.3 provides an overview of the average compositions of the tape casts used to make the electrodes of the pristine and modified powder, including the target recipe composition and desired loading. In addition, the resulting average electrode loading of the cells used in the electrochemical tests are given. In order to obtain electrodes with the same, desired loading, several tape casts with different solid/liquid slurry ratios were made in the preliminary stages. A solid/liquid ratio of 0.70-0.71 was found to give a loading of approximately 6.4 $\mathrm{mg\,cm^{-2}}$ of active material for both powders. In total two and three tape casts with the optimised solid/liquid ratio were made of the pristine and modified powder, respectively, in order to reduce the discrepancy in cell loading between the powders and inside each parallel.

The compositions of the individual tape casts used for making the electrodes can be found in Table B.1 in Appendix B.

Table 4.3: Composition of the target recipe and the tape casts used for electrodes. The solid/liquid ratio of the slurry and the average loading of the electrodes are also given. All values are given as mean ± standard deviation origin from to the number of tape casts or electrodes (loading).

Powder (#tapes)	CB [wt.%]	CMC [wt.%]	SBR [wt.%]	Graphite [wt.%]	Solid/Liquid Ratio [-]	Loading [mg $\mathrm{cm^{-2}}$]
Target	2.0	1.5	1.5	95	N/A	6.4
Pristine (2)	2.001 ± 0.006	1.513 ± 0.001	1.603 ± 0.074	94.88 ± 0.069	0.7073 ± 0.0167	6.439 ± 0.080
Modified (3)	2.032 ± 0.036	1.505 ± 0.006	1.638 ± 0.088	94.82 ± 0.077	0.7006 ± 0.0089	6.457 ± 0.094

4.4 Electrochemical Characterisation

4.4.1 Coin cell plating tests

The specific capacity against cycle number for the 100% SOC and 50% SOC plating tests are presented in Figure 4.4a and 4.4b, respectively. The reference cells of both powders are also included. The C-rates and the plating cycle are also marked in the bottom of the figures.

Generally, it can be observed that the pristine reference cells have a rather similar capacity compared to the modified reference cells. In the first cycle after the formation (cycle 3), the pristine and modified references have an average capacity of 334.7±5.2 mAh g^{-1} and 332.8±1.1 mAh g^{-1}, respectively. In addition, the average capacity from cycle 3 to 13, in parallel to the plating programmes, is 327.6±4.3 mAh g^{-1} and 321.3±8.3 mAh g^{-1} for the pristine and modified references, respectively.

The standard deviation for the pristine 100% SOC test results is quite large, illustrated by the error bars around the average values in Figure 4.4a. This is due to one of the cells (cell B) displaying a poor performance with rapid degradation from the beginning, which is illustrated in Figure 4.5. Hence, the results of cell A are more reliable, as they compare better with the reference cells of the pristine powder. This cell had an average capacity of 337.4±0.9 mAh g^{-1} before the plating cycle, and surprisingly a slightly higher value of 338.7±0.6 mAh g^{-1} in the cycles after. The average value of the 100% SOC pristine cells show on the other hand a slightly lower value of 317.2±3.3 mAh g^{-1} after, compared to 322.5±2.4 mAh g^{-1} before the plating cycle. This matches the trend of the modified cells, as these had an average capacity of 328.1±2.0 mAh g^{-1} before the plating cycle, and a moderately lower value of 322.6±5.2 mAh g^{-1} in the cycles after.

The capacities in the plating cycle, i.e. delithiation capacity after the 100% SOC plating step, are much higher for both powders with values of 371.3 mAh g^{-1} for the pristine cell A and 360.2±2.4 mAh g^{-1} for the modified cells. This is approximately an increase of 34 and 32 mAh g^{-1} for the pristine and modified cells, respectively, when compared with the cycles before. These are reasonable amounts when taking into account that the amount of additional Li lithiated/plated during the plating step was 40 mAh g^{-1}.

Figure 4.4b displays the capacity plots for the cells undergoing the 50% SOC coin cell plating tests, including the same reference cells as before. The pristine cells undergoing the 50% SOC test have an average capacity of 317.4±2.7 mAh g^{-1} before the plating cycle, and a slightly lower value of 313.5±4.2 mAh g^{-1} in the five cycles after. Similarly, the modified cells have an average capacity of 323.1±2.7 mAh g^{-1} before the plating cycle, and a lower value of 312.6±3.8 mAh g^{-1} after. In contrast to the 100% SOC plating programme, the capacities in the plating cycle are decreased for the 50% SOC cells with values of 185.0±13.3 and 209.5±18.0 mAh g^{-1} for the pristine and modified cells, respectively. This was also somewhat expected, as the cells were only lithiated until reaching approximately 50% SOC, i.e. approximately a capacity of 160-165 mAh g^{-1}, before an additional 40 mAh g^{-1} was imposed in the plating step.

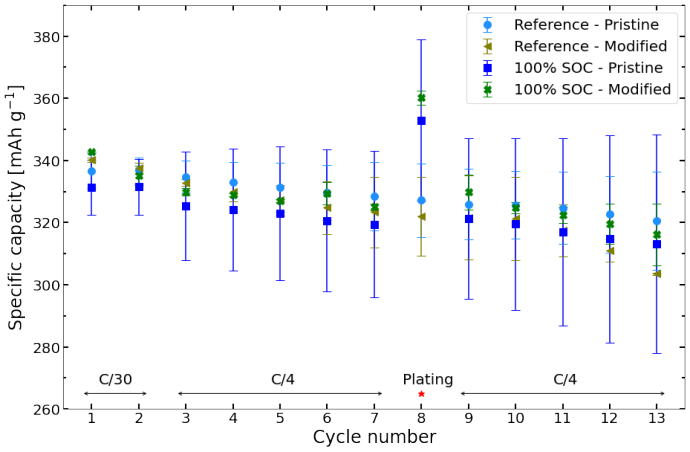

(a)

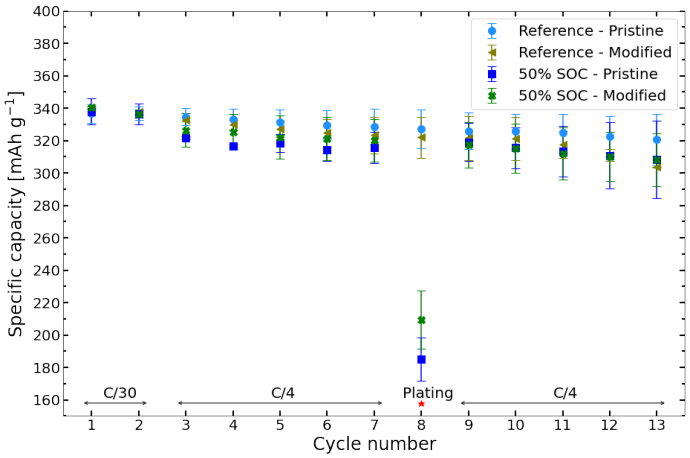

(b)

Figure 4.4: The specific capacity against cycle number for the (a) 100% SOC and (b) 50% SOC coin cell plating tests, including the reference cells.

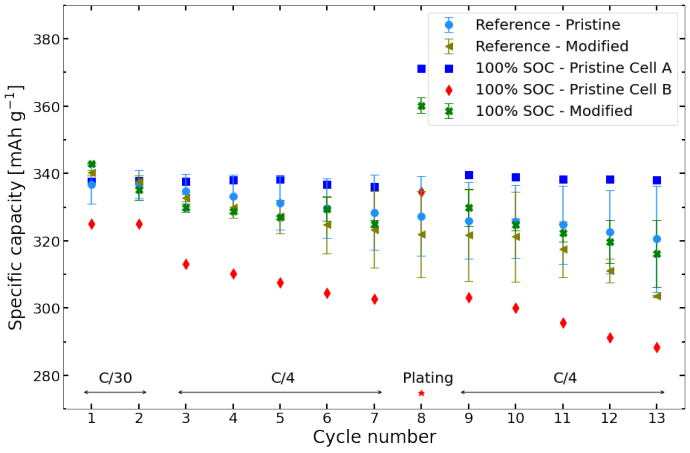

Figure 4.5: The specific capacity against cycle number for the 100% SOC coin cell plating tests showing the pristine cells separately (cell A and B), including the reference cells and the average of the modified cells.

To further analyse the cell performances, the CE against cycle number for the coin cell plating tests are provided. The CE plot for the 100% SOC and 50% SOC plating tests are presented in Figure 4.6a and 4.6b, respectively, including the reference cells. Similarly to the capacity plots, the pristine 100% SOC cells are plotted separately in Figure 4.7.

Generally, it can be observed that the reference cells of each powder have comparable CE, i.e. 99.71±0.10% and 99.63±0.21% for the pristine and modified cells, respectively, in average for the cycles after formation.

The pristine 100% SOC cells have an average CE of 99.98±0.49% in the cycles before and 99.97±0.14% in the cycles after the plating cycle. The modified 100% SOC cells have an average CE of 100.09±0.14% in the cycles before and 99.81±0.29% in the cycles after the plating cycle. Hence, it can be seen that the plating cycle in the 100% SOC plating test has negligible effect on the CE of the cells with marginal decreased CE, as they also are comparable with the reference cells.

The pristine 50% SOC cells have an average CE of 100.13±0.74% in the cycles before and 99.92±0.14% in the cycles after the plating cycle. The modified 50% SOC cells have an average CE of 100.04±0.31% in the cycles before and 99.84±0.21% in the cycles after the plating cycle. Hence, the same trend is observed here.

In addition, it is interesting to compare the first cycle ICL to reveal possible differences between the powders in the formation cycles. The first cycle ICL can be calculated by Equation 2.8 in Section 2.1.2, i.e. 100% - CE (cycle 1). The calculated values for the coin cell plating tests and references are presented in Table 4.4. It can be seen that all of the cells of the modified powder have a smaller first cycle ICL compared to those of the pristine powder.

Table 4.4: The first cycle ICL for the coin cell plating tests and references. The values are the average values of the cells undergoing the same programme including the standard deviation ($\mu \pm \sigma$).

Programme	Powder	First cycle ICL [%]
Reference	Pristine	6.69 ± 2.54
	Modified	4.30 ± 0.20
100% SOC	Pristine	6.25 ± 3.29
	Modified	3.01 ± 1.26
50% SOC	Pristine	3.87 ± 0.12
	Modified	2.06 ± 0.09

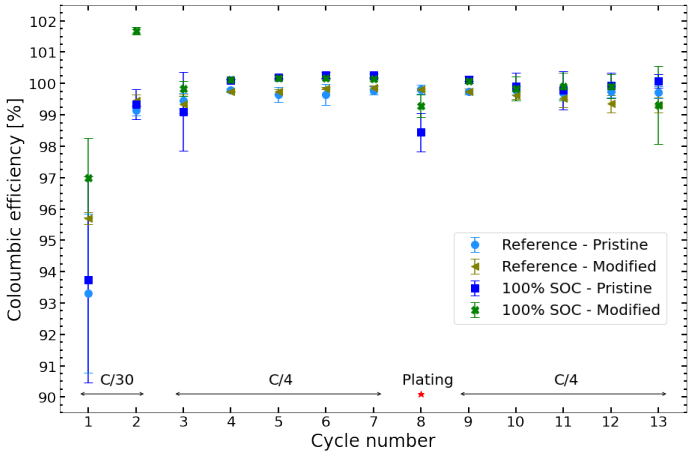

(a)

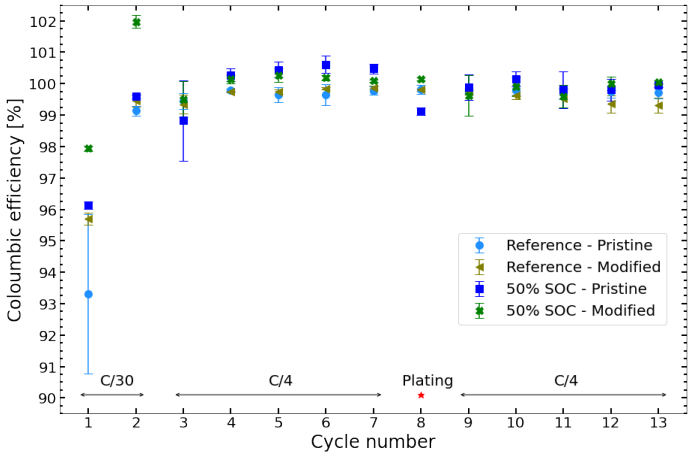

(b)

Figure 4.6: The CE against cycle number for the (a) 100% SOC and (b) 50% SOC coin cell plating tests, including the reference cells.

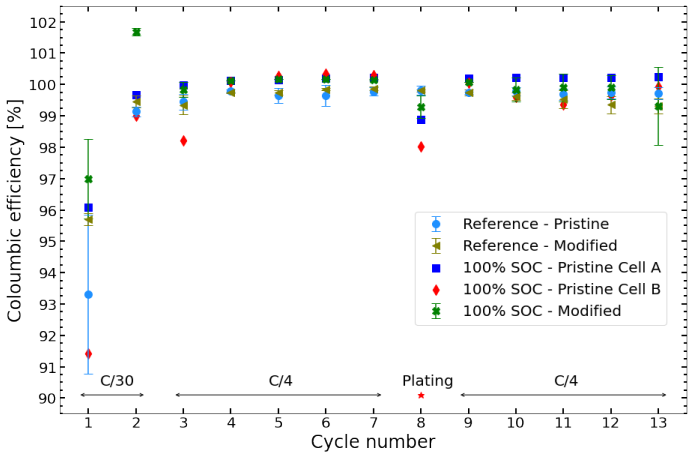

Figure 4.7: The CE against cycle number for the 100% SOC coin cell plating tests showing the pristine cells separately (cell A and B), including the reference cells and the average of the modified cells.

The voltage profiles displaying the potential against the capacity of the plating cycle, as well as the cycle before (pre-plating) and after (post-plating), are of interest to investigate in more detail. Only one of the cells in each parallel are presented in Figure 4.8. However, the cells in the other parallel can be found in Figure A.1 in Appendix A to verify the reproducibility.

Figure 4.8a and 4.8b show the lithiation curves for the 100% SOC and 50% SOC plating tests, respectively. In the pre- and post-plating curves for both programmes, the potential is always kept above 0 V with the cut-off potential of 5 mV for a normal lithiation of the graphite. The plating step is clearly illustrated by the sudden voltage drop in both figures, due to the change in C-rate from C/4 to 3C. In addition, the difference between the plating programmes is visible with the voltage drop occurring much earlier in the lithiation for the 50% SOC programme compared to the 100% SOC programme, i.e. at 50 mV and 5 mV, respectively. The charge limit set for the amount of plating seems to be fulfilled as well, as approximately 40 mAh g^{-1} is lithiated below 0 V for all cells. This amount will be referred to as the "theoretical" amount plated, as the reduction of Li-ions becomes thermodynamically possible below 0 V vs. Li/Li^{+}.

Figure 4.8c and 4.8d show the delithiation curves for the 100% SOC and 50% SOC plating tests, respectively. As opposed to the pre- and post-plating cycles, a voltage plateau in the plating cycle can be observed below 0.10 V approximately, especially for the 100% SOC tests. This corresponds to the stripping reaction of reversibly plated Li, as the deintercalation of Li ions occurs at potentials from about 0.10-0.15 V. For the 50% SOC tests, the plateaus are not as prominent, which indicate a lower amount of reversible plated Li. Also, their final delithiation capacity is much lower compared to the cycles before and after, but this was expected as only 50% of the capacity was lithiated. When comparing the two powders, it seems as the plateaus are slightly longer for the pristine cells, which indicates a larger amount of reversible plated Li for these cells compared to the modified cells.

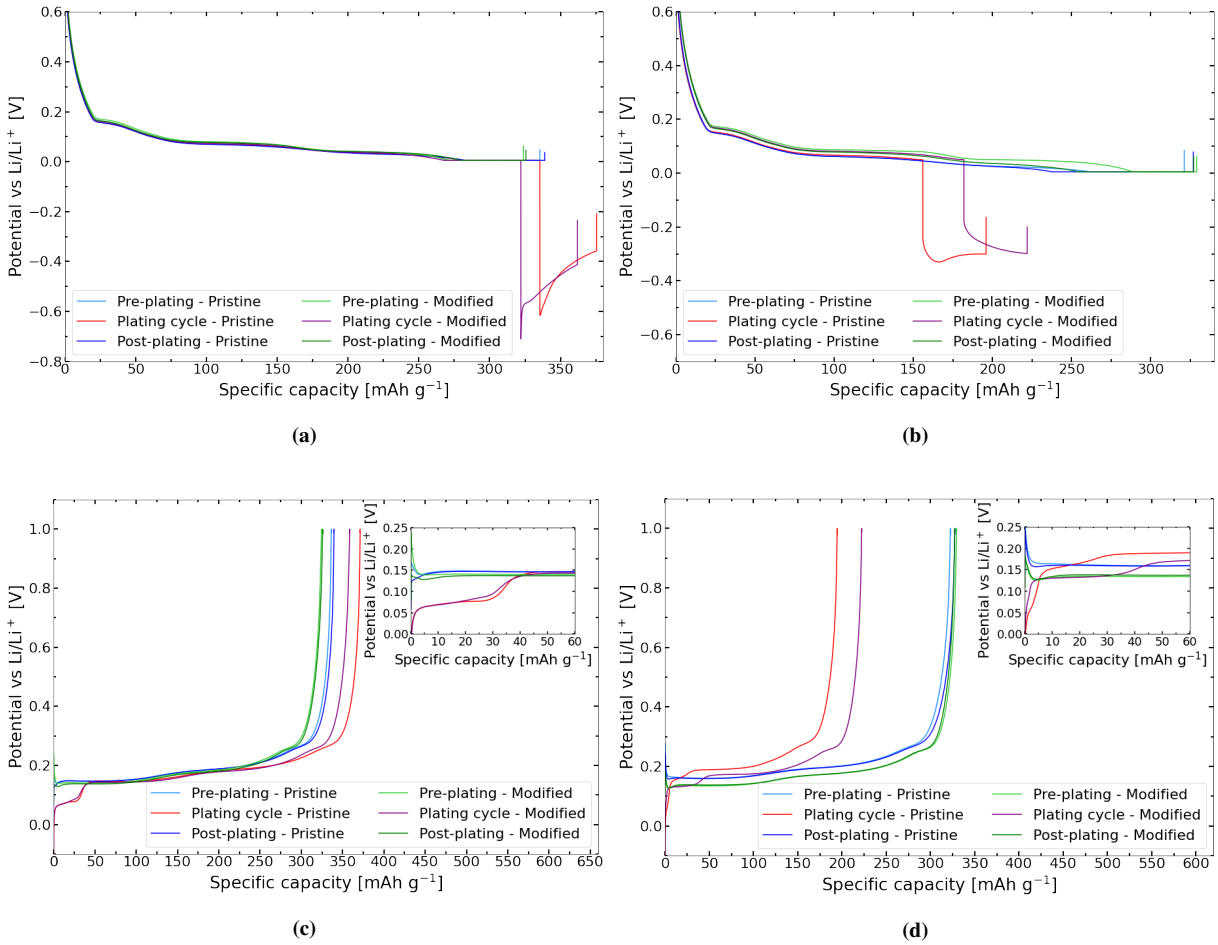

Figure 4.8: Voltage curves of the (a, b) lithiation and (c, d) delithiation for the (a, c) 100% SOC and (b, d) 50% SOC plating tests.

In order to more accurately determine the reversible amounts plated, the same voltage curves were made into differential capacity plots, which are presented in Figure 4.9. Only potentials up to 0.45 V are presented, as no information of interest is found at higher potentials. The differential capacity plots for the parallel cells can be found in Figure A.2 in Appendix A to verify the reproducibility. The direction of lithiation and delithiation processes, as well as the plating and stripping reactions in the plating cycle (red and purple curves), are pointed out.

The trends from the voltage curves can be recognised in the differential capacity plots by looking at the size and positions of the peaks. Firstly, the plating step is seemingly equal for all the cells when looking at the lithiation below 0 V. Secondly, the difference in amounts stripped between the two plating programmes is clear, as the stripping peaks for the 100% SOC cells in Figure 4.9a (pristine) and 4.9c (modified) are much larger compared to the 50% SOC cells in Figure 4.9b (pristine) and 4.9d (modified). In fact, nearly no peaks can be observed at potentials below 0.10 V for the 50% SOC cells.

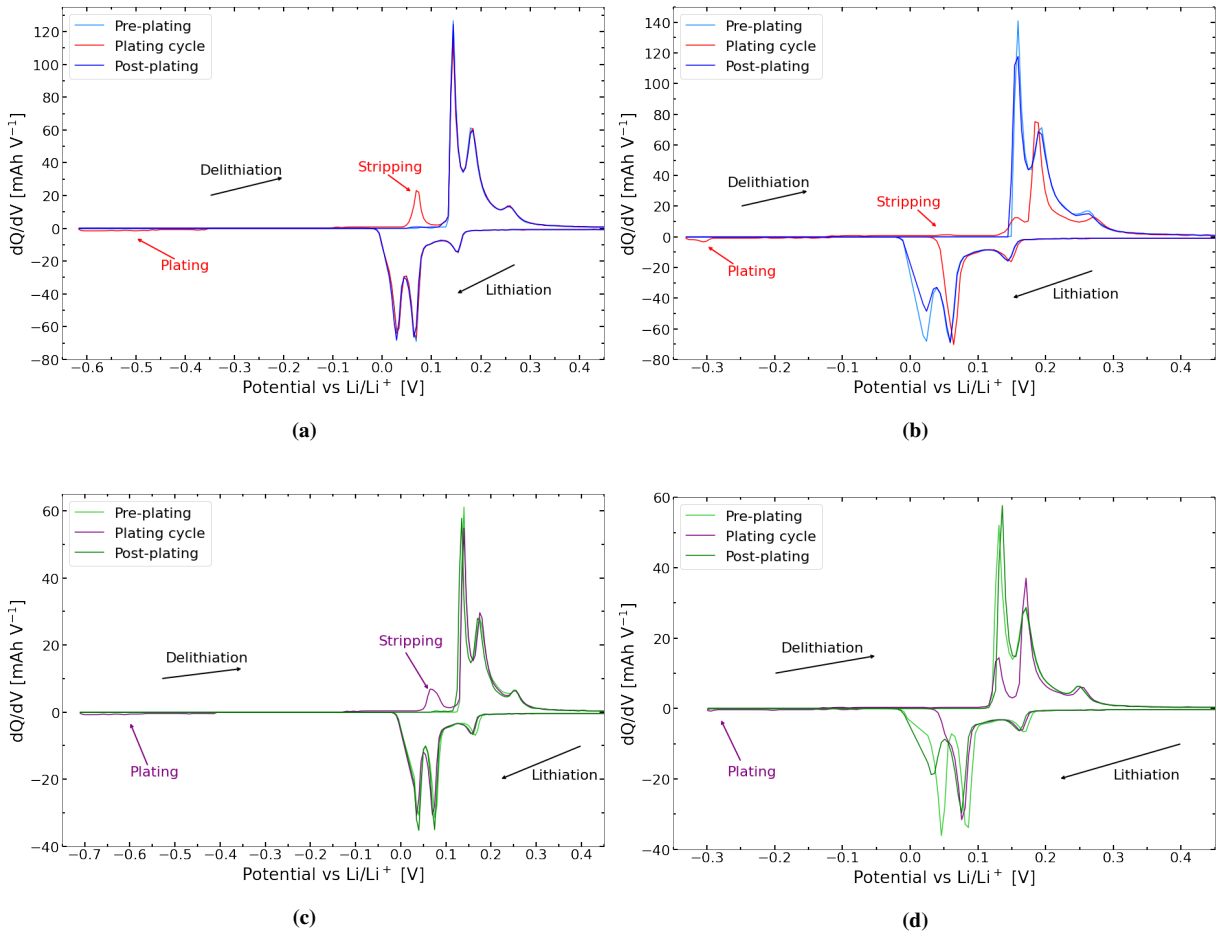

Figure 4.9: Differential capacity plots of the (a) pristine 100% SOC, (b) pristine 50% SOC, (c) modified 100% SOC, and (d) modified 50% SOC cell.

Figure 4.10 illustrates the delithiation between 0 and 0.2 V in the differential capacity plots, which enables better comparison and detection of the stripping peaks. It is evident that much more is stripped for the 100% SOC pristine cell compared to the 100% SOC modified cell, when analysing the magnitude of their respective stripping peaks in Figure 4.10a. This trend is repeated to a small extent for the 50% SOC cells in Figure 4.10b, as it is possible to detect a small peak for the pristine cell, but not for the modified cell. The potential aligning with the end point of the stripping peak was noted for all the cells. These potentials were then used to quantify the reversible plating, i.e. amount stripped, by reading off the capacity that was delithiated until this potential in the voltage curve of the respective cell. The end point of the stripping reaction translated approximately to the inflection point after the plateau at low potentials in the delithation curves.

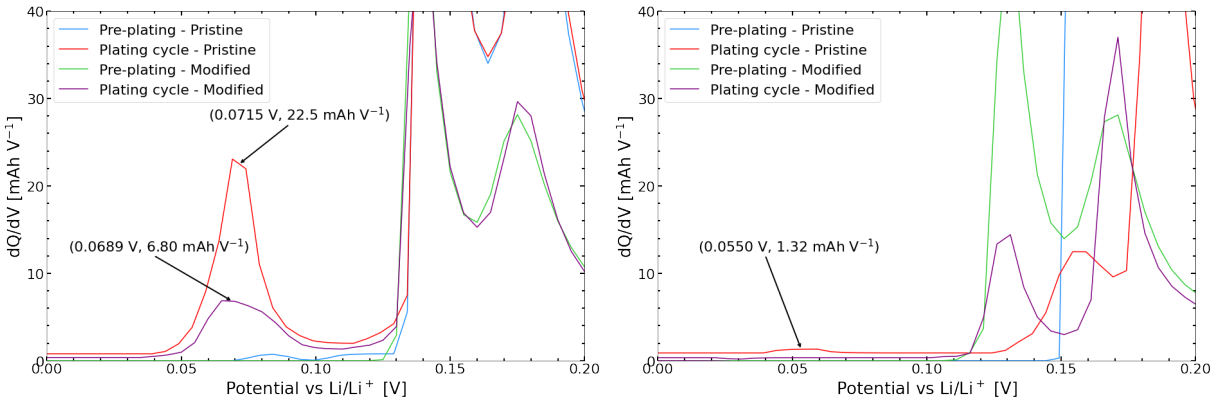

(a) **(b)**

Figure 4.10: Comparison of the stripping peaks of the pristine and modified cells for the (a) 100% SOC and (b) 50% SOC plating tests.

Table 4.5 summarises information about the loading of the cells, the SOC when plating was imposed, and the charge that was plated in theory for the coin cell plating cells. The SOC-values were calculated by dividing the capacity lithiated until the C-rate was changed from C/4 to 3C on the delithiation capacity of the previous cycle.

Table 4.5: The loading, SOC when plating was imposed, and the theoretical (theo.) amount plated for the coin cell plating tests. The values are the average values of the two cells undergoing the same programme including the standard deviation ($\mu \pm \sigma$).

Plating prog.	Powder	Loading [mg cm^{-2}]	SOC plating start [%]	Theo. plated [mAh g^{-1}]
100% SOC	Pristine	6.46 ± 0.03	99.66 ± 0.19	40.01 ± 0.01
	Modified	6.50 ± 0.12	99.30 ± 0.00	39.97 ± 0.00
50% SOC	Pristine	6.56 ± 0.01	46.42 ± 2.80	39.97 ± 0.01
	Modified	6.40 ± 0.02	52.79 ± 3.48	39.96 ± 0.01

Table 4.6 summarises the reversible (stripped) and irreversible amounts plated for the coin cell plating tests. The reversible amounts were determined from the analysis of the voltage curves and differential capacity plots, as previously described. The irreversible plated Li accounts for Li that has been plated, but not reversibly oxidised into ions again. This results in an irreversible capacity loss, and is determined by calculating the difference between the delithiation and lithiation capacity in the plating cycle. The sum of reversible and irreversible plating gives the "experimental" amount plated. This value was then divided by the "theoretical" amount plated presented in Table 3.3 to give the percentage of experimental plating of the theoretical amount (lithiation < 0 V). Interestingly, there is a significant difference between the pristine and modified powder in both the 100% SOC and 50% SOC plating programmes, as a much higher percentage is plated for the pristine cells. In addition, much less seems to be plated when the SOC of the cell is lower.

Table 4.6: The experimentally (exp.) determined amounts plated and the percentage plated of theoretical (theo.) amount. The total experimental amount plated is the sum of the reversible (stripped) and the irreversible plated Li. The values are the average values of the two cells undergoing the same programme, including the standard deviation ($\mu \pm \sigma$).

		Exp. plated [mAh g^{-1}]			
Plating prog.	Powder	Reversible	Irreversible	Total	%-Exp. plated of theo. [%]
100% SOC	Pristine	33.3 ± 1.1	5.5 ± 1.8	38.8 ± 2.9	96.8 ± 7.2
	Modified	30.3 ± 3.2	2.6 ± 1.3	32.9 ± 4.5	82.1 ± 11.2
50% SOC	Pristine	3.5 ± 0.7	1.7 ± 0.10	5.2 ± 0.8	12.9 ± 2.0
	Modified	2.0 ± 0.7	0	2.0 ± 0.7	5.0 ± 1.8

4.4.2 CV and EIS

Figure 4.11 illustrates the cyclic voltammogram of the second CV performed (CV 2) in the CV and EIS cycling programme. The cyclic voltammogram of the first CV (CV 1) can be found in Figure A.3 in Appendix A, but will not be discussed or analysed in-depth.

The modified cell is illustrated in the green curves and it can be observed that the lithiation occurs at higher potentials compared to the pristine cell. Similarly, the delithiation occurs at lower potentials for the modified cell, as the green curves are shifted to the left for positive currents.

The similar loadings of the pristine and modified cell, i.e. 6.40±0.14 mg cm^{-2} and 6.42±0.14 mg cm^{-2}, respectively, can be assumed to have negligible effect on the cell performances.

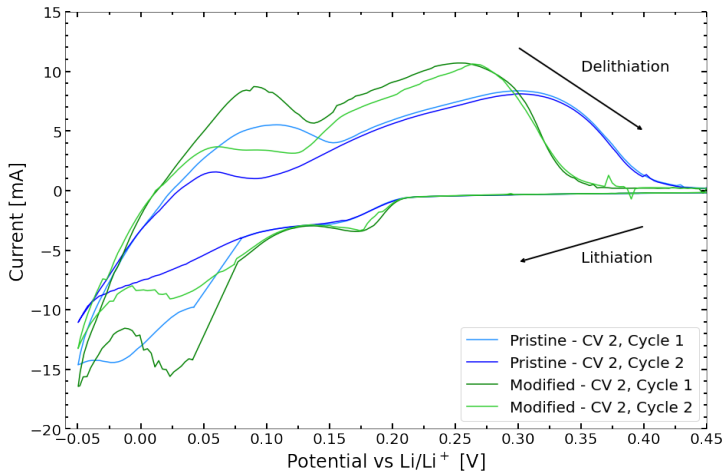

Figure 4.11: CV curves of the second CV test performed on the pristine (blue) and modified (green) PAT cells.

The impedance spectra collected before (EIS 1), between (EIS 2), and after (EIS 3) the two CV tests for the pristine and modified cell are presented in Figure 4.12a and 4.12b, respectively. The spectra were fitted with the equivalent circuit presented in Section 3.4.2, and the resulting values of the circuit elements can be found in Table 4.7 and 4.8 for the pristine and modified cell, respectively.

The pristine cell has a higher total electrode resistance compared to the modified cell, when observing the larger width of the half circles in Figure 4.12a compared to the ones in Figure 4.12b. This coincides with the tabulated values in Table 4.7 and 4.8, as R_1+R_2 is greater for the pristine cell in all of the EIS measurements. R_1 represents the ohmic resistance and R_2 the total resistance of the electrode. Moreover, the trend over the EIS measurements is the same for both cells with an increased impedance after each of the CV tests with imposed plating. However, there is a significantly larger increase in the final EIS measurement for the modified cell.

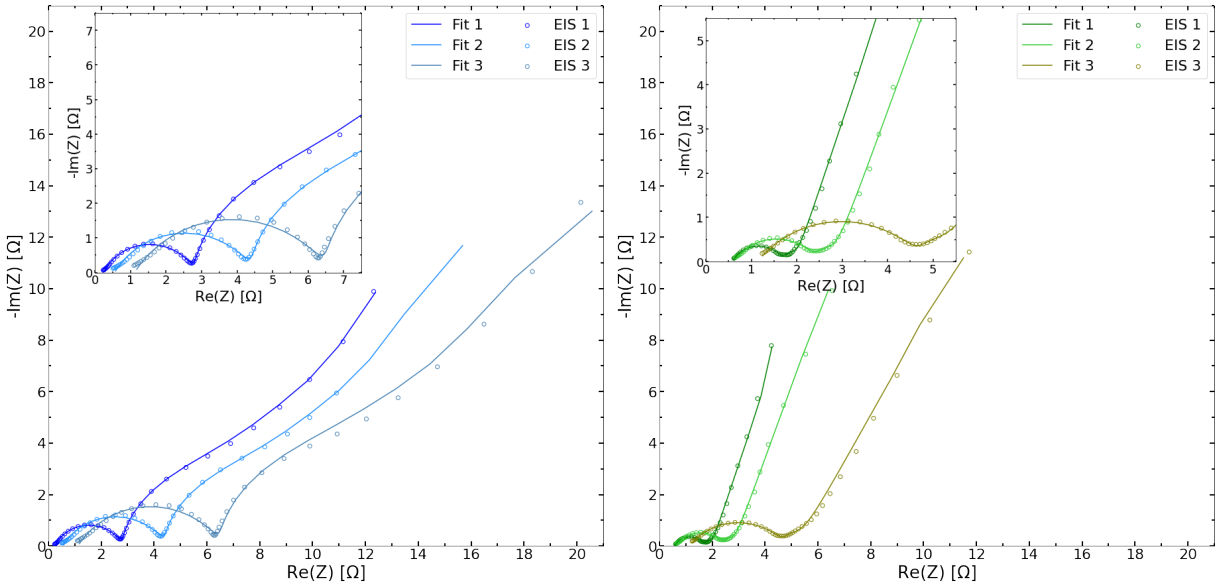

Figure 4.12: Nyquist plots for the (a) pristine and (b) modified graphite cell undergoing plating in CV. EIS 1 is the impedance measurement performed before the first CV, EIS 2 is between the first and second CV, and EIS 3 is after the second CV.

Table 4.7: Circuit element values from the EIS fits for the pristine cell.

Circuit element		EIS 1	EIS 2	EIS 3
R_1	[Ω]	0.245 ± 0.006	0.553 ± 0.014	1.11 ± 0.025
R_2	[Ω]	2.57 ± 0.02	3.93 ± 0.05	5.48 ± 0.07
R_3	[Ω]	4.60 ± 0.38	3.82 ± 0.77	4.64 ± 1.41
Z_{Ws1}	[Ω $s^{\alpha-1}$]	33.3 ± 1.9	32.6 ± 2.9	34.1± 4.5
τ_{Ws1}	[s]	998 ± 89.0	783 ± 119	718 ± 168
α_{Ws1}	[-]	0.554 ± 0.010	0.539 ± 0.015	0.514 ± 0.024
Q_{CPE1}	[F $s^{\alpha-1}$]	0.00702 ± 0.00025	0.00645 ± 0.00038	0.00455 ± 0.00030
α_{CPE1}	[-]	0.715 ± 0.006	0.666 ± 0.010	0.648 ± 0.011
Q_{CPE2}	[F $s^{\alpha-1}$]	1.44 ± 0.03	1.20 ± 0.06	1.08 ± 0.06
α_{CPE2}	[-]	0.948 ±0.019	1.00 ± 0.05	1.00 ± 0.07

Table 4.8: Circuit element values from the EIS fits for the modified cell.

Circuit element		EIS 1	EIS 2	EIS 3
R_1	[Ω]	0.587 ± 0.005	0.623 ± 0.008	1.14 ± 0.02
R_2	[Ω]	1.11 ± 0.02	1.83 ± 0.04	3.67 ± 0.05
R_3	[Ω]	0.498 ± 0.086	0.572 ± 0.146	0.754 ± 0.208
Z_{Ws1}	[Ω $s^{\alpha-1}$]	68.4 ± 9.3	93.9 ± 14.7	64.9 ± 6.9
τ_{Ws1}	[s]	1517 ± 97	2226 ± 378	1660 ± 290
α_{Ws1}	[-]	0.805 ± 0.019	0.770 ± 0.094	0.672 ± 0.008
Q_{CPE1}	[F $s^{\alpha-1}$]	0.0113 ± 0.0007	0.0117 ± 0.0008	0.00622 ± 0.00037
α_{CPE1}	[-]	0.716 ± 0.010	0.646 ± 0.011	0.583 ± 0.009
Q_{CPE2}	[F $s^{\alpha-1}$]	1.63 ±0.18	1.26 ± 0.16	0.764 ± 0.119
α_{CPE2}	[-]	0.781 ±0.064	0.887 ± 0.126	0.967 ± 0.132

It is interesting to compare the change in capacitance of the cells, as this provides an indication of the active area inside the electrodes. The value can be estimated by plotting -Im(Z) against ω^{-1} for the values at high frequencies and finding the slope of the linear regression. Figure 4.13a and 4.13b illustrate such plots for the pristine and modified cell, respectively, with the insets showing the points in their respective Nyquist plot. Table 4.9 displays the results of the slope of the linear regressions in Figure 4.13, and the corresponding capacitance, which equals the reciprocal of the slope; $C = 1/slope$.

Overall, the pristine cell has a steeper slope compared to the modified cell. This then translates to a smaller capacitance in all of the EIS measurements compared to for the modified cell. The change in capacitance seems to be comparable going from EIS 1 to EIS 2, i.e. after the first CV test, as the capacitance is approximately halved for both cells. On the other hand, the capacitance of the modified cell is drastically reduced by 75% from EIS 2 to EIS 3, while the pristine cell shows a reduction of 50%.

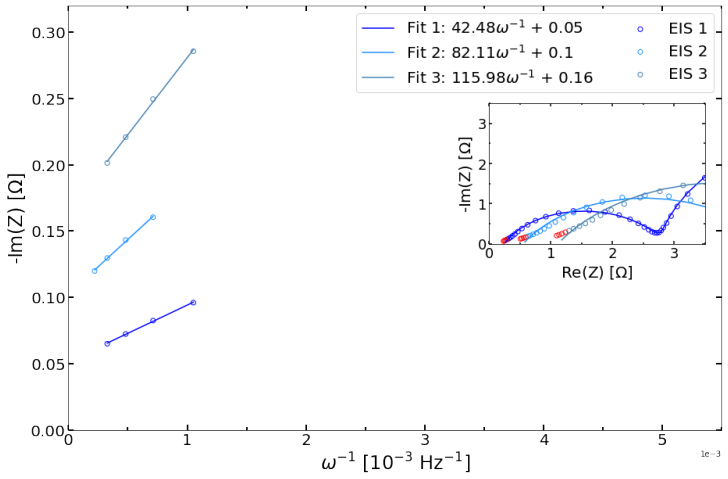

(a)

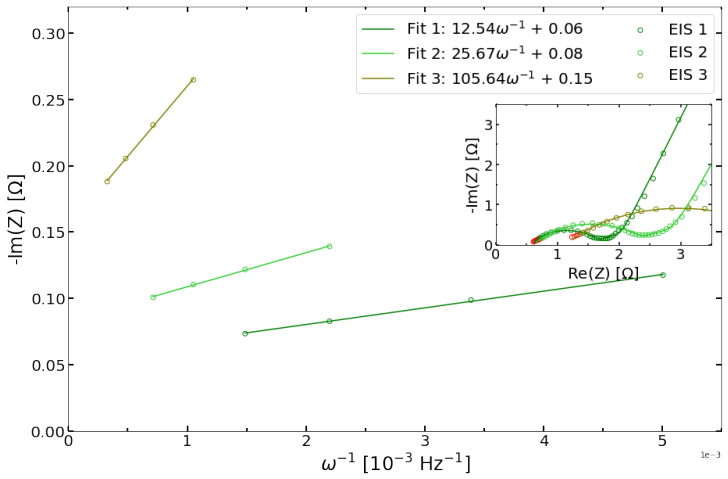

(b)

Figure 4.13: -Im(Z) against ω^{-1} for the impedance measurements at high frequencies including linear regression fittings for the (a) pristine and (b) modified cell. The inset plots show the corresponding points in the Nyquist plots marked in red.

Table 4.9: The slope and resulting capacitance determined from the -Im(Z) vs ω^{-1} plots.

EIS measurement		Slope [Ω Hz]	C [10^{-2} F]
Pristine	1	42.48	2.354
	2	82.11	1.218
	3	115.98	0.8622
Modified	1	12.54	7.974
	2	25.67	3.900
	3	105.64	0.9466

4.5 Post Mortem Characterisation

4.5.1 Camera Images

Figure 4.14 presents the camera images of the non-cycled and cycled graphite electrodes. Clearly, the electrodes that have been imposed with plating (c-h) are much more deteriorated compared to the non-cycled electrode in (a) and the reference cycled electrode in (b). Especially, the CV tested electrodes illustrated in (e) and (h) seem to be covered with some kind of depositions.

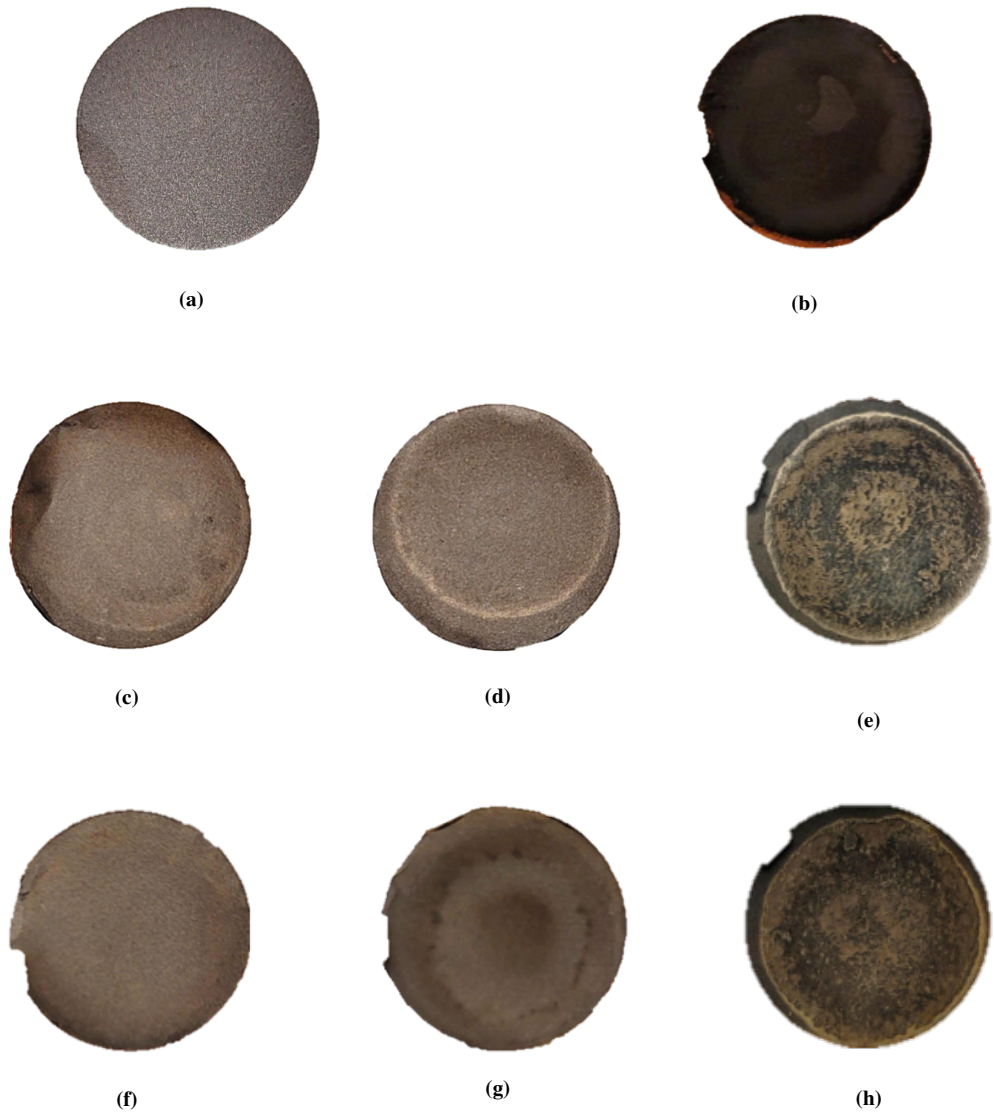

Figure 4.14: Camera images of electrodes; (a) non-cycled electrode, (b) cycled reference with no imposed plating, (c) 100% SOC pristine, (d) 50% SOC pristine, (e) CV pristine, (f) 100% SOC modified, (g) 50% SOC modified, (h) CV modified.

4.5.2 SEM - SE Micrographs

Non-cycled - Figure 4.15 presents the SEM micrographs of the non-cycled electrodes of the (a, c) pristine and (b, d) modified powder at (a, b) 2 K and (c, d) 5 K magnifications.

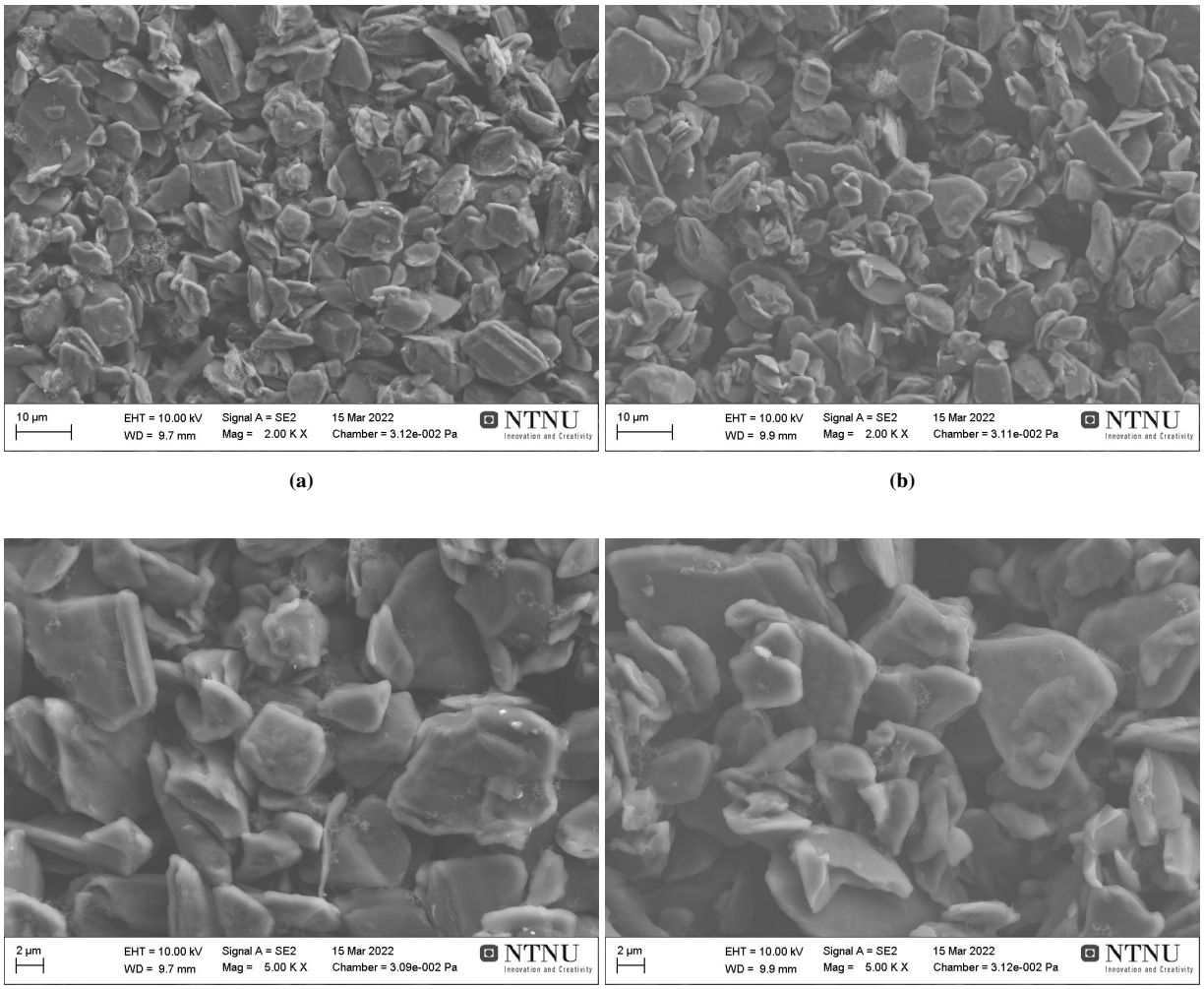

Figure 4.15: SEM images of non-cycled electrodes of the (a, c) pristine and (b, d) modified powder at (a, b) 2 K and (c, d) 5 K magnifications.

100% SOC plating - Figure 4.16 presents the SEM micrographs of the electrodes undergoing the 100% SOC plating programme of the (a, c, e) pristine and (b, d, f) modified powder at (a, b) 2 K, (c, d) 5 K, and (e, f) 10 K magnifications. The red ellipses highlight some structures that look like Li metal dendrites, which indicate traces of remaining Li plating on both electrodes.

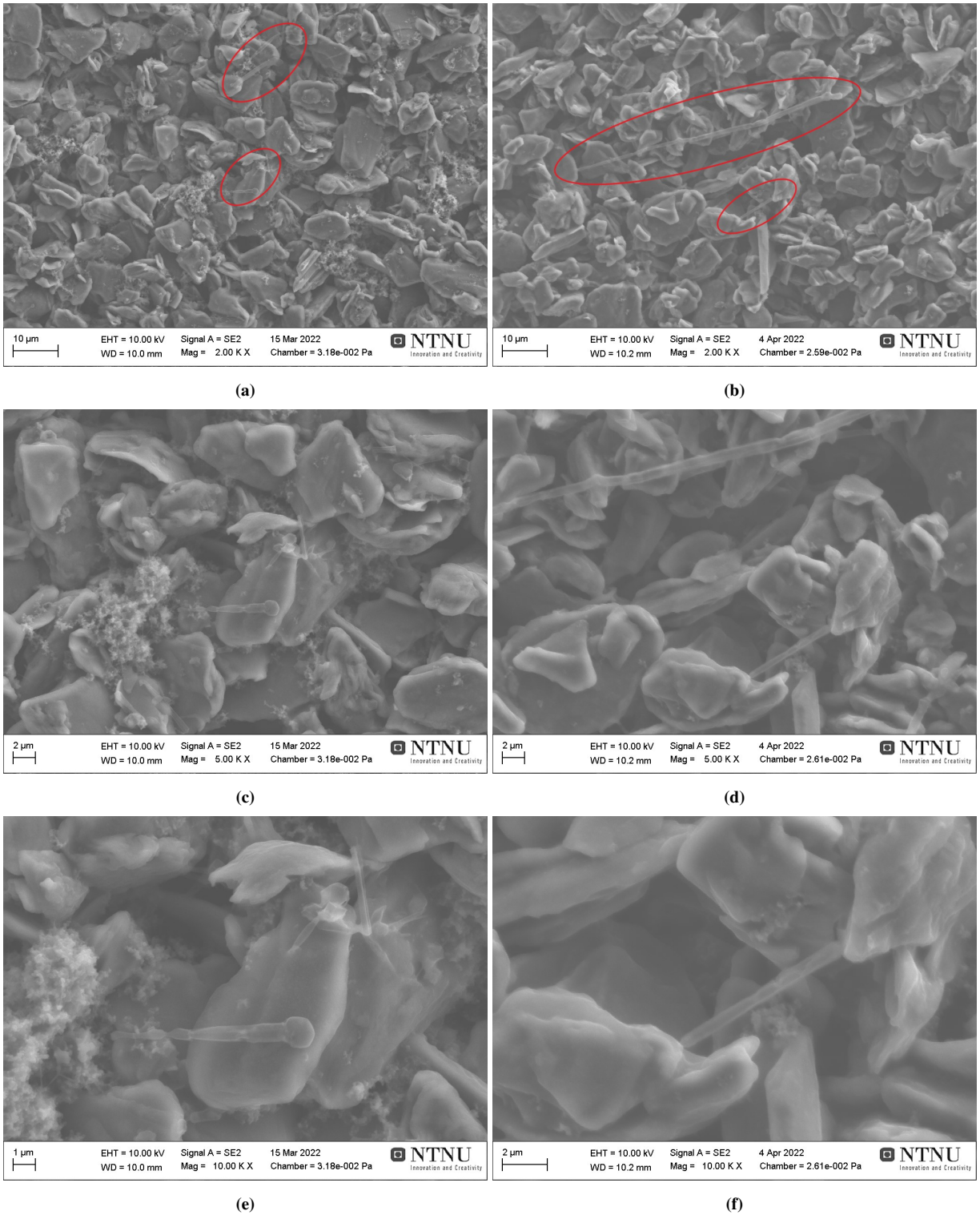

Figure 4.16: SEM micrographs of 100% SOC electrodes of the (a, c, e) pristine and (b, d, f) modified powder at (a, b) 2 K, (c, d) 5 K, and (e, f) 10 K magnifications.

50% SOC plating - Figure 4.17 presents the SEM micrographs of the electrodes undergoing the 50% SOC plating programme of the (a, c, e) pristine and (b, d, f) modified powder at (a, b) 2 K, (c, d) 5 K, and (e, f) 10 K magnifications. There are no abnormal structures, such as Li metal dendrites, visible on either electrodes.

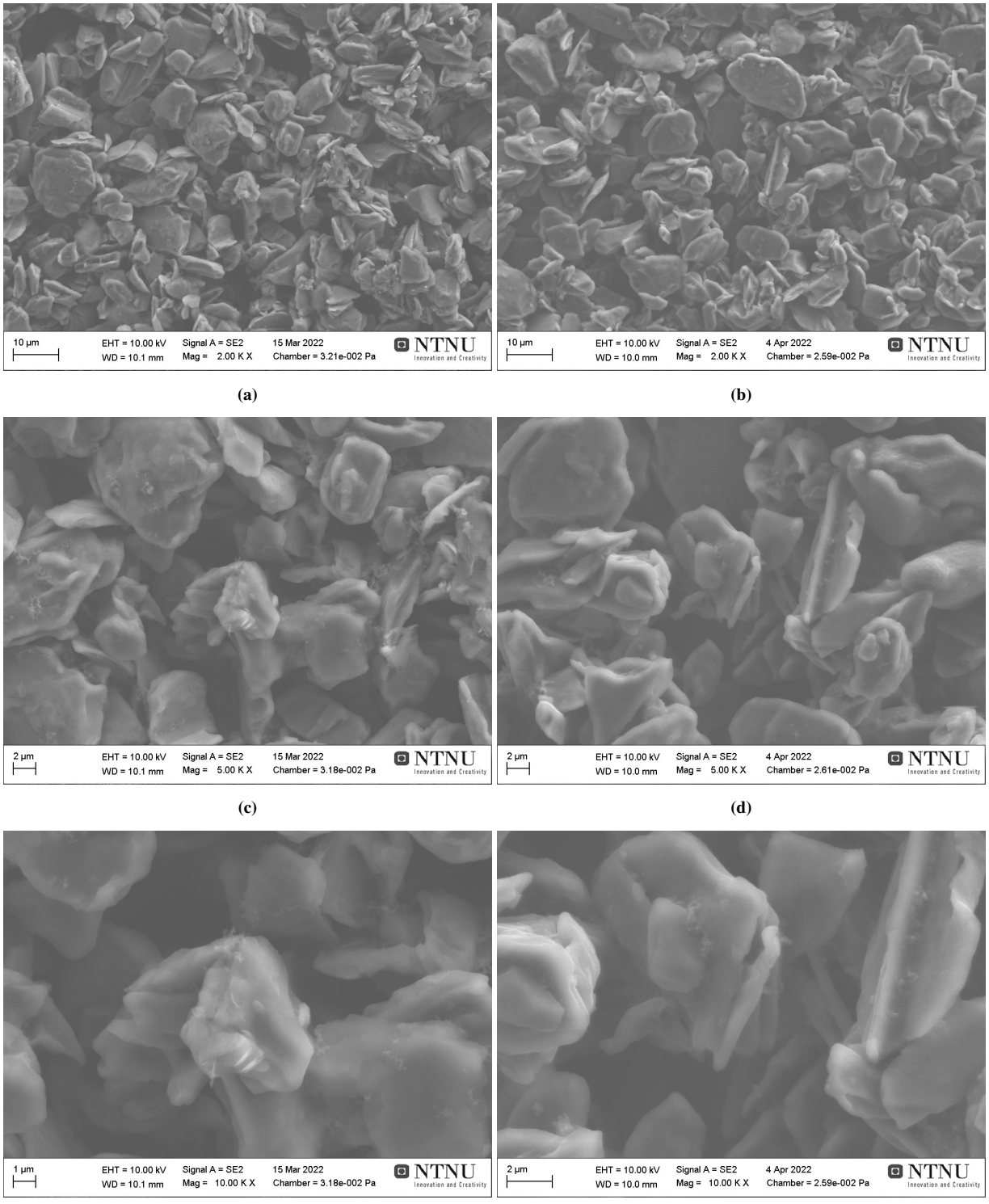

Figure 4.17: SEM micrographs of 50% SOC electrodes of the (a, c, e) pristine and (b, d, f) modified powder at (a, b) 2 K, (c, d) 5 K, and (e, f) 10 K magnifications.

CV - Figure 4.18 presents the SEM micrographs of the electrodes undergoing the CV and EIS programme of the (a, c, e) pristine and (b, d, f) modified powder at (a, b) 500, (c, d) 2 K, and (e, f) 5 K magnifications. There are clearly some abnormal structures deposited on the surface of both electrodes. The lower magnification micrographs display a film-like structure on both electrodes. In addition, a mossy structure is visible at higher magnifications, especially for the pristine electrode.

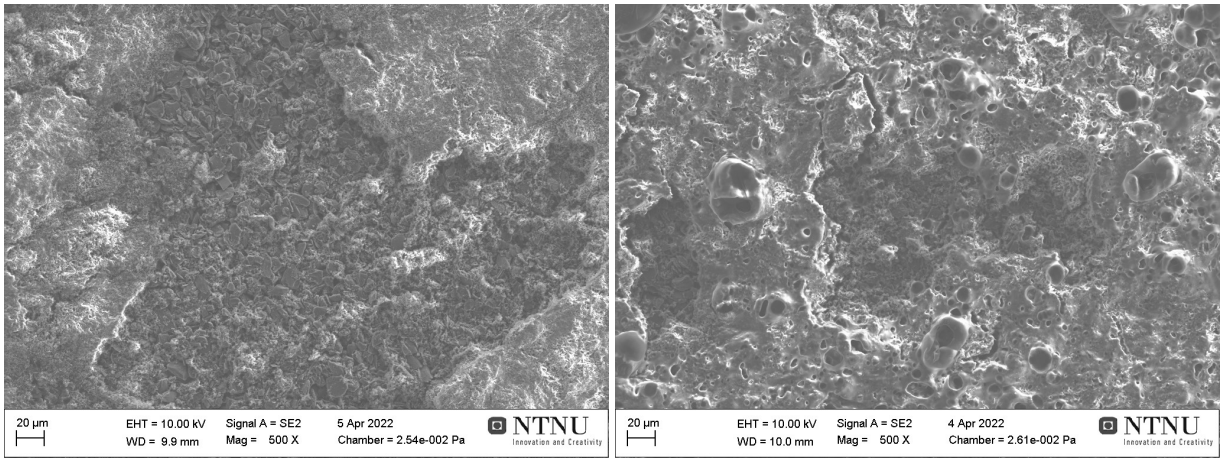

(a) **(b)**

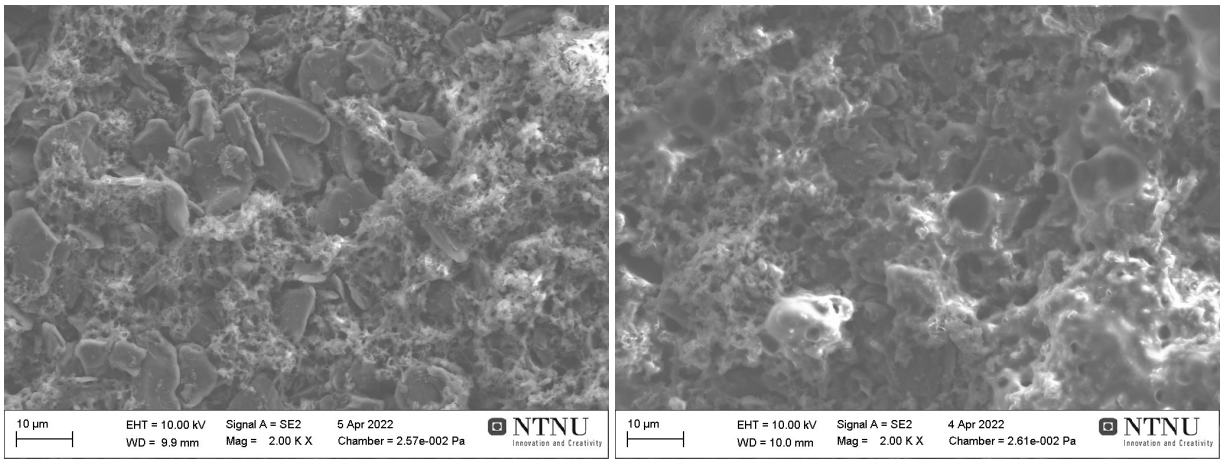

(c) **(d)**

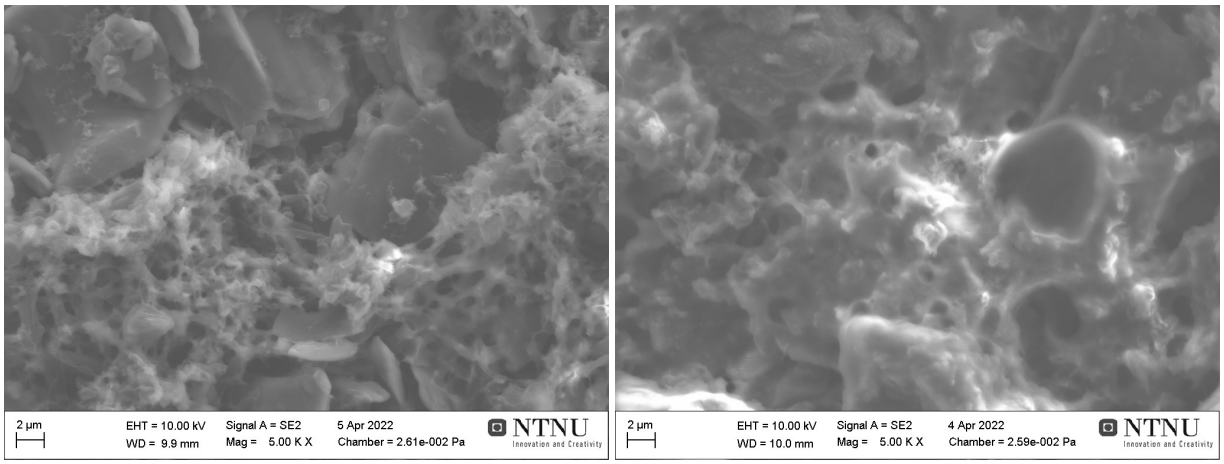

(e) **(f)**

Figure 4.18: SEM micrographs of CV electrodes of the (a, c, e) pristine and (b, d, f) modified powder at (a, b) 500, (c, d) 2 K, and (e, f) 5 K magnifications.

4.5.3 SEM - BSE Micrographs

Reference - To confirm possible Li plating, some SEM micrographs obtained by BSEs will be presented and compared with micrographs obtained by SEs. For comparison, Figure 4.19 presents the SE and BSE micrographs of one of the reference cells of the modified powder. The Z-contrast images obtained by BSEs at (b) 2 K and (d) 5 K magnifications illustrate no significant difference in the elemental composition on the surface. This was expected as the graphite electrodes are composed of 95 wt% graphite.

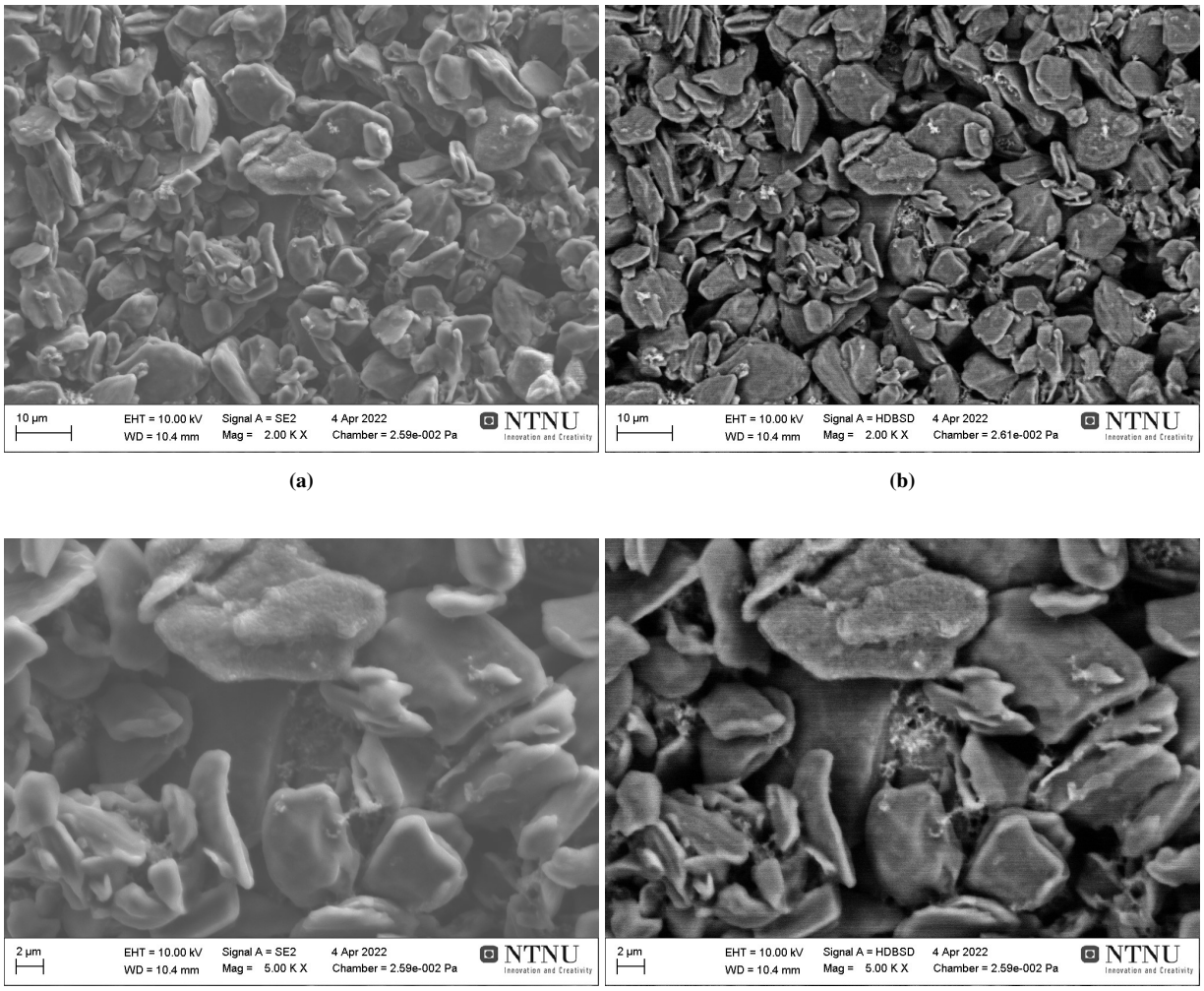

Figure 4.19: SEM micrographs of one of the reference cells of the modified powder at (a, b) 2K and (c, d) 5K magnifications using (a, c) SEs and (b, d) BSEs.

100% SOC modified - Figure 4.20 presents the SE and BSE micrographs of one of the modified 100% SOC electrodes with the visible Li metal dendrites highlighted. The Z-contrast images obtained by BSEs at (b) 2 K and (d) 5 K magnifications show that the dendrites become more transparent and slightly darker compared to in the corresponding SE micrographs in (a) and (c).

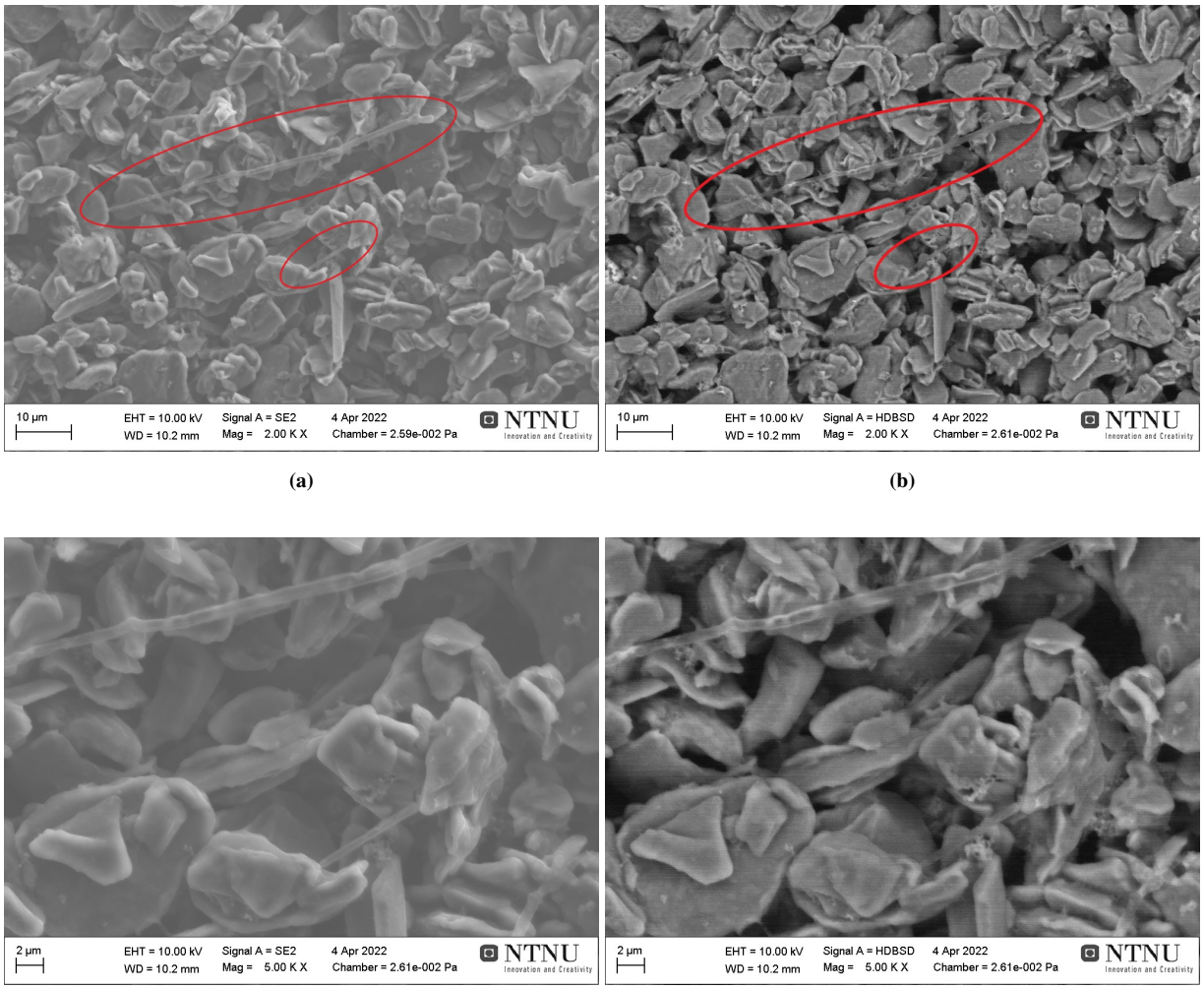

Figure 4.20: SEM micrographs of one of the modified 100% SOC electrodes at (a, b) 2K and (c, d) 5K magnifications obtained by (a, c) SEs and (b, d) BSEs.

CV pristine - Figure 4.21 presents (a, c) SE and (b, d) BSE micrographs of the pristine CV electrode at (a, b) 2 K and (c, d) 5 K magnifications. The mossy structure is brighter than the graphite particles. Some of the smaller dendrite structures covering the graphite particles, highlighted by the red ellipses in (c) and (d), become darker in the BSE micrographs.

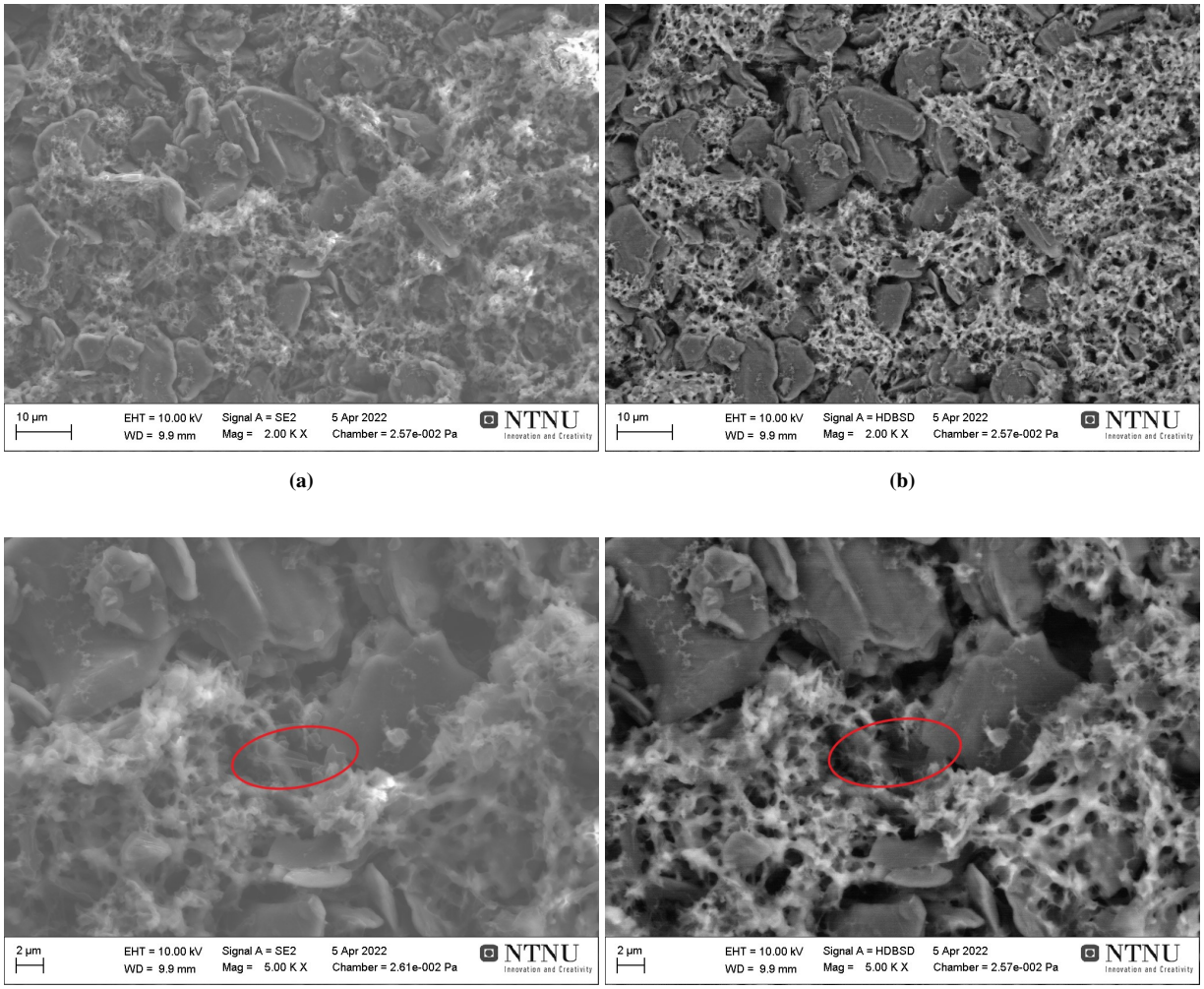

(a) **(b)**

(c) **(d)**

Figure 4.21: SEM micrographs obtained by (a) SEs and (b) BSEs of the pristine CV electrode at (a, b) 2 K and (c, d) 5K magnifications.

CV modified - Figure 4.22 presents (a, c) SE and (b, d) BSE micrographs of the modified CV electrode at (a, b) 2 K and (c, d) 5 K magnifications. Less of the mossy/dendrite structure is visible here compared to the pristine cell, as the majority of the surface is covered by the film-structure. The film appears brighter than the graphite particles, which indicates presence of heavier elements than carbon.

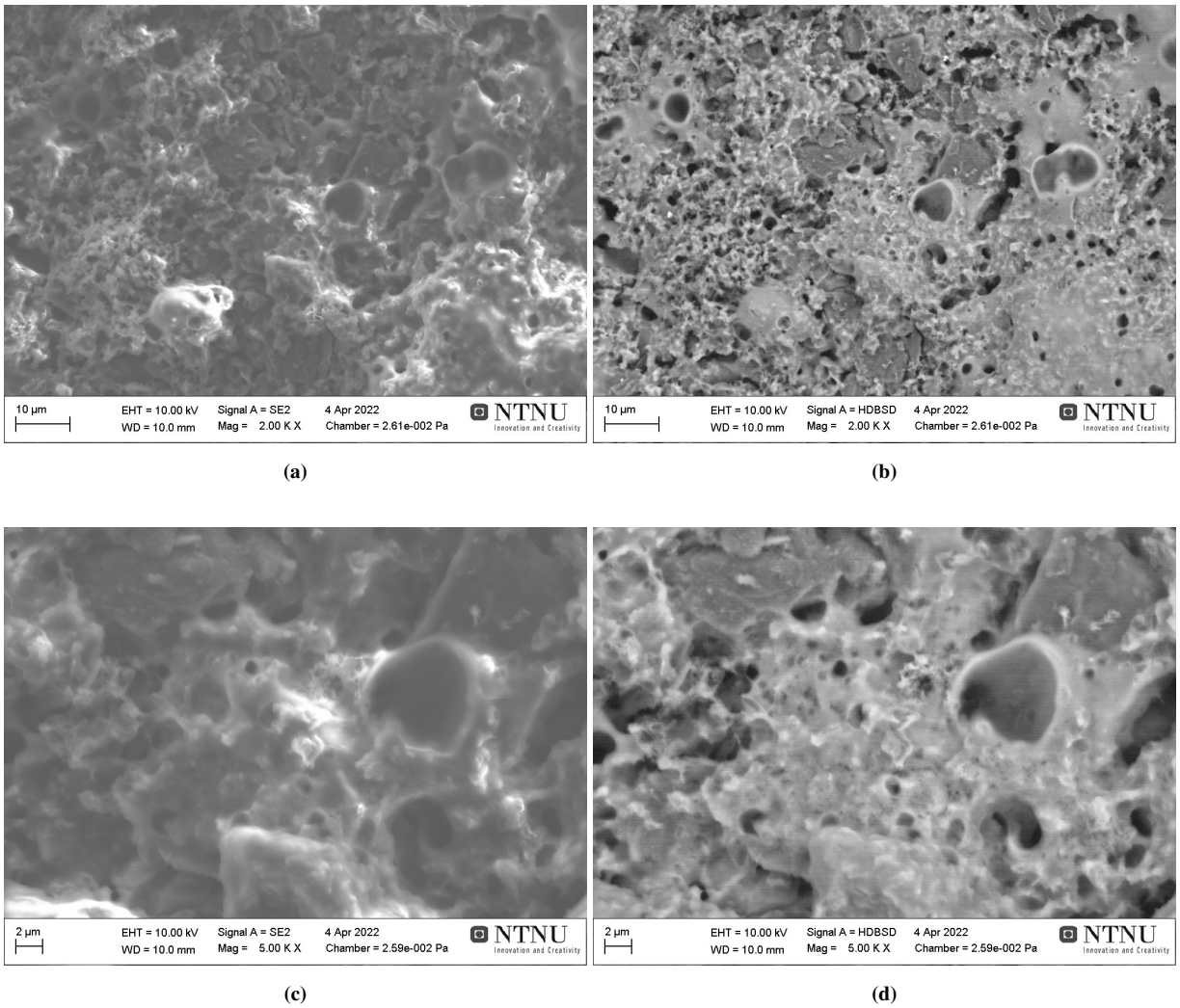

Figure 4.22: SEM micrographs obtained by (a) SEs and (b) BSEs of the pristine CV electrode at (a, b) 2 K and (c, d) 5K magnifications.

4.5.4 FIB

Non-cycled - Figure 4.23 shows the SEM micrographs of the non-cycled electrodes of the pristine and modified powder with cross sections obtained by FIB. The cuts made were 17.12 and 16.16 µm deep for the pristine and modified, respectively, and will be used in comparison with the plated electrodes.

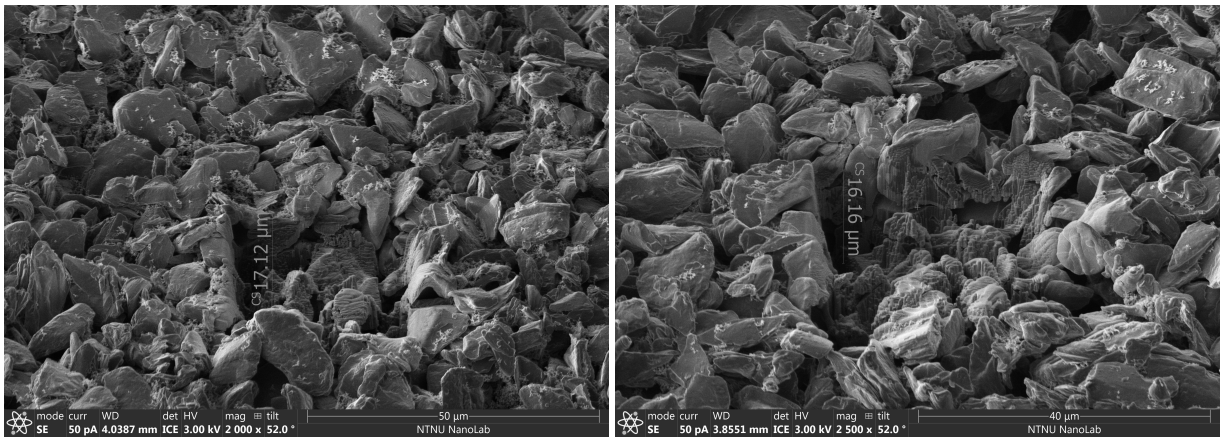

(a) **(b)**

Figure 4.23: SEM micrographs of the cross sections obtained by FIB of non-cycled electrodes of the (a) pristine (2 K magnification) and (b) modified (2.5 K magnification) powders.

Plated electrodes - Figure 4.24 shows the SEM micrographs of 100% SOC plating electrodes with the cross sections obtained by FIB. One can observe Li metal dendrites on the surface of the pristine electrode in (a), but none on the surface of the modified electrode in (b). The cross sections were approximately 30 µm deep for both electrodes. The cross sections of the pristine and modified are shown in (c) and (d), respectively. No evident differences can be observed between the two cross sections, which may indicate that the plated Li metal is only superficial and does not remain inside the pores of the electrode. An additional cross section was made in the pristine electrode in an area without visible plating on the surface. The SEM micrographs of this area display the same trend as the cross sections presented here, i.e. with no signs of plating beneath the surface. These complementary results can be found in Figure A.4 in Appendix A.

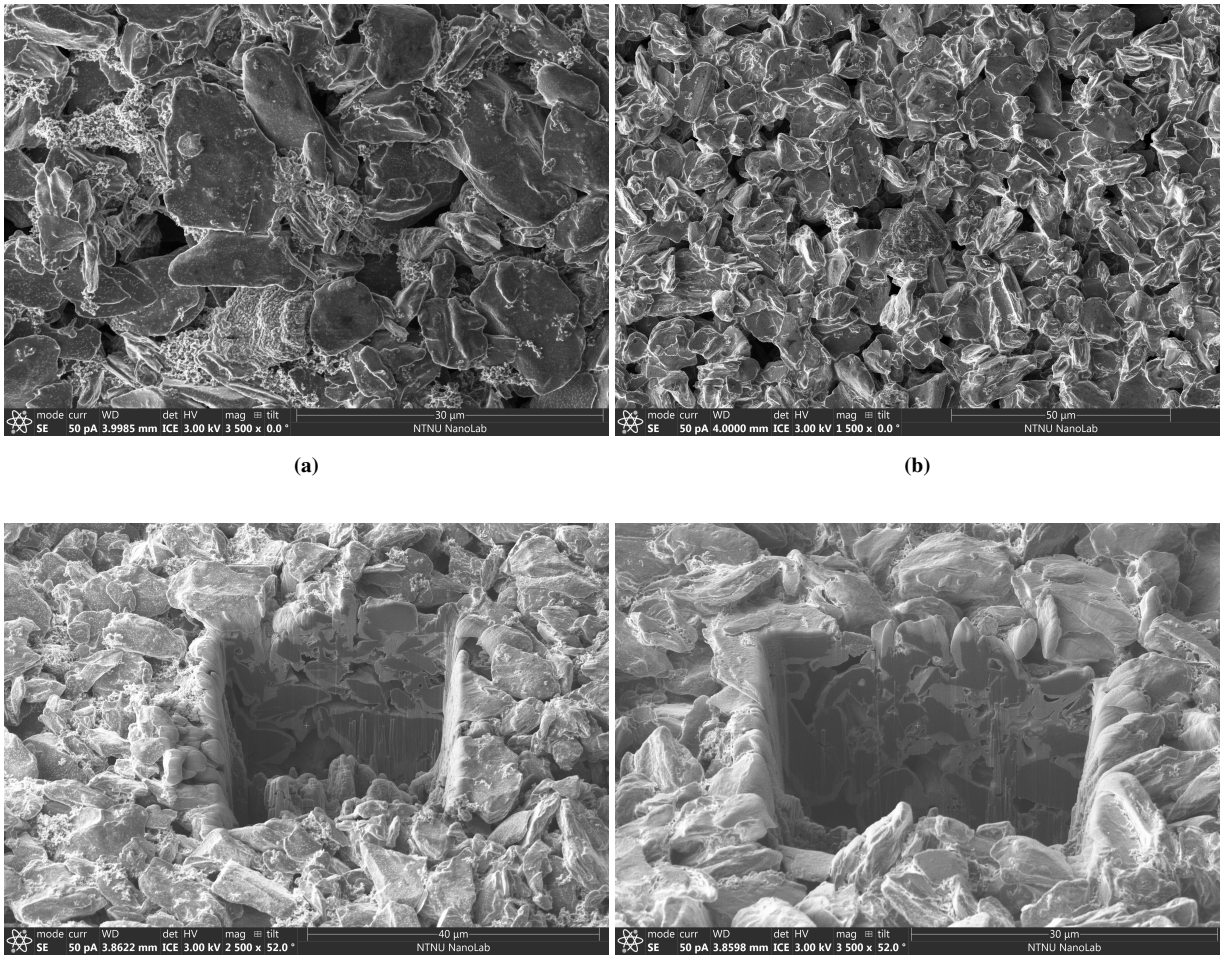

(a) **(b)**

(c) **(d)**

Figure 4.24: SEM micrographs of 100% SOC plating electrodes; (a) overview of the pristine with visible plating (3.5 K), (b) overview of the modified without visible plating (1.5 K). (c) and (d) show the FIB cross sections of the pristine (2.5 K) and modified (3.5 K), respectively.

5 Discussion

5.1 Detection and Quantification of Li Plating

The electrochemical tests presented in this thesis were designed with the objectives of imposing Li plating on the graphite anodes and evaluating the response. Hence, methods for imposing, detecting and quantifying Li plating were determined and utilised.

In a half cell configuration with Li metal as the counter electrode or in a three-electrode cell with a Li metal reference ring, it is possible to detect the occurrence of Li plating by monitoring the graphite potential, as discussed in Section 2.6.4. Hence, it was possible to validate the occurrence of imposed plating when the graphite potential dropped below 0 V. In the coin cell plating tests, the potential drop was created by polarising the graphite surface with a change in C-rate from C/4 to 3C. This is illustrated in the lithiation curves in Figure 4.8. Hence, this confirms that an increased charging C-rate is a triggering factor for Li plating, as pointed out by Waldmann et al.[31] In the CV and EIS test, it was possible to impose Li plating by performing the CV until the lower potential limit of -50 mV, as shown in Figure 4.11.

One should consider and be aware of several factors when quantifying the amount of Li plating. It is important to consider that the intercalation and plating reactions may occur in parallel below 0 V, despite the plating reaction being favoured in theory. In the coin cell plating tests, approximately 40 mAh g^{-1} was lithiated below 0 V for all cells, as shown in Table 4.5. However, when quantifying the Li plating by adding the reversible and irreversible amounts plated, as proposed by e.g. Petzl and Danzer,[46] it can be seen that much less than the theoretical amount has been plated. Table 4.6 summarises the results from this experimental approach of quantifying Li plating. It can be seen that 96.8$\pm$7.2% and 82.1$\pm$11.2% of the theoretical amount were plated for the 100% SOC pristine and modified cells, respectively. While only 12.9$\pm$2.0% and 5.0$\pm$1.8% of the theoretical amount were plated for the 50% SOC pristine and modified cells, respectively. Hence, the theoretical approach of quantifying the Li plating cannot be seen as very reliable, especially for plating occurring at a low SOC.

Nevertheless, one should evaluate possible weaknesses of the experimental approach as well. For instance, the quantification of reversible plating may become less precise for smaller quantities of plating, such as for the cells in the 50% SOC plating test. This is because it becomes increasingly difficult to determine the end potential of the stripping reaction, which is used to determine the capacity stripped in the voltage curves. This is illustrated in Figure 4.10 by the small or even absent stripping peaks for the 50% SOC cells compared to the large and well-defined peaks for the 100% SOC cells. In this way, it may become impossible to quantify possible plating for smaller quantities of imposed plating at low SOC or marginal quantities at higher SOC. This is because the corresponding voltage relaxation plausibly would be even smaller than in the results reported here, which are for relatively large amounts of imposed plating. Hence, it could be interesting to investigate the effect of imposing smaller quantities of plating for a range of SOCs, in order to find a lower limit for quantifying reversible plating from voltage curves with a high level of confidence.

The method for quantifying the irreversible plating should also be evaluated, as cell ageing due to e.g. side reactions in the electrolyte also results in irreversible capacity losses over time. In the CE plots for the coin cell plating tests in Figure 4.6, it can be seen that the CE in the plating cycle is reduced for all the plated cells compared to the cycles before and after. This indicates that less has been lithiated compared to delithiated, and that some capacity has been lost. This loss is reasonable to assume to be due to Li plating, as the CE seems to be relatively stable in the cycles before and after, indicating marginal capacity loss due to other side reactions. However, it may become increasingly difficult to distinguish the capacity loss due to side reactions from the irreversible loss due to plating over time, as LIBs degrade more rapidly over time. Hence, it could be interesting to impose plating after e.g. 25, 50 and 100 cycles to see whether there is a clear reduction in CE only for the plating cycle here as well, or that it becomes difficult to accurately quantify the possible irreversible plating, especially for smaller amounts of imposed plating.

Supplementary to the electrochemical characterisation, various post mortem characterisation techniques can be utilised to verify the occurrence of plating. For instance, Ghanbari et al.[47] demonstrated higher mass-% of Li in areas with assumed Li plating with the use of GD-OS. Also, the characteristic dendrite structure of Li plating was detected in these areas using SEM, which provided additional confirmation upon the occurrence of Li plating. In this thesis, the electrode surfaces were characterised in SEM using SEs and BSEs with the aim of detecting and verifying possible remaining Li plating on the plated electrodes. The SE micrographs in Figure 4.16 of the 100% SOC electrodes illustrate the presence of some dendrite structures that can be assumed to be Li plating. Different from Ghanbari et al.,[47] Z-contrast micrographs obtained by BSEs were used to analyse the composition of the electrode surfaces. In the Z-contrast micrographs in Figure 4.20, it can be observed that the dendrite structures become more transparent and slightly darker compared to the surrounding graphite particles. This indicates that the dendrites are composed of an element with a lower atomic number compared to the graphite particles. Since Li is a lighter element than carbon, which constitutes most of the graphite electrode (95 wt%), one can assume with a higher level of confidence that the dendrite structures actually are Li metal remaining after imposed plating. The fact that no such dendrite structures were observed for the 50% SOC electrodes, such as in Figure 4.17, coincides with the results of the electrochemical characterisation with much less being plated for these cells compared to the 100% SOC cells. It also confirms the higher irreversible plating of the 100% SOC cells, as Li metal is visibly remaining after plating.

In summary, the experimental method for quantifying the amount of Li plating seems to be much more reliable compared to the theoretical estimate. However, limitations such as possible decreased accuracy for small amounts of plating and aged cells should be noted, and are interesting subjects for further studies. Post mortem characterisation can be used to verify the occurrence of plating, as plated Li metal has characteristic structures such as dendrites that stand in stark contrast to the graphite particles.

5.2 Mitigation of Li Plating

A goal of investigating the nature of Li plating was to reveal the main factors that influence the ability of the graphite anode to mitigate plating. The characteristics of the graphite particles and the influence of surface modifications, in addition to external factors such as the effect of SOC and charging C-rate are among the factors that will be discussed.

5.2.1 Effect of Surface Modifications

Active materials characterisation

The active materials characterisation reveals some notable differences between the pristine and modified powder. The powders are relatively similar in size and shape, but it could be observed in the SEM micrographs in Figure 4.1 that the modified particles are slightly more round and less irregular compared to the pristine particles. It is difficult to detect the amorphous carbon coating of the modified particles on the microscale, but this was somewhat expected as such coatings only are a few nanometres thick to not compromise the energy density of the LIB or the diffusion distance of Li-ions, as discussed in Section 2.6.3. Nevertheless, the slight increase in thickness caused by the modifications and the coating can be detected from the laser diffraction results presented in Figure 4.2 and Table 4.1. The mean diameter of the pristine and modified powder was $11.49 \pm 3.99\,\mu m$ and $12.73 \pm 4.37\,\mu m$, respectively. This was illustrated in the PSD curves by a small shift towards larger diameters for the modified powder compared to the pristine powder. The coating will also cover possible defects and irregularities on the surface of the particles, as discussed in Section 2.6.3, which reduces the specific surface area and micropore area. This is confirmed by the lower specific surface area and lack of micropore area for the modified powder compared to the pristine powder, as seen in Table 4.2 and Figure 4.3. Hence, the amorphous carbon coating has resulted in slightly larger particles with lower surface roughness. However, it is interesting to evaluate to what extent these surface modifications may affect the electrochemical performance and possibly the mitigation of Li plating.

Coin cell plating results

In the results from the coin cell plating tests, it can be observed that the pristine powder provides a slightly higher specific capacity compared to the modified powder, i.e. 334.7 ± 5.2 mAh g^{-1} and 332.8 ± 1.1 mAh g^{-1} in average for cycle 3 for the pristine and modified reference cells, respectively. This trend is kept over the whole duration of the cycling programme, which is expected as the amorphous carbon coating adds extra weight to the electrode without providing additional capacity. However, there is no apparent difference between the powders when evaluating the standard deviation, so more cells should be cycled to verify the observed trend. This is as the capacity of the graphite anode is an important parameter to optimise when developing LIBs for use in EVs. Nevertheless, other parameters of the electrochemical performance of the powders must also be considered.

One such parameter is the first cycle ICL. This loss is smaller for all of the cells of the modified powder compared to those of the pristine powder, as seen in Table 4.4. Hence, the carbon coating successfully contributed with reducing the first cycle ICL, due to the reduced surface area and improved Li-ion diffusion on the anode surface, as discussed in Section 2.6.3. This is also highly favourable towards the mitigation of plating, as a smaller first cycle ICL corresponds to the formation a thinner SEI layer, which in turn results in a decreased cell resistance and polarisation. This is reflected by the quantities plated in the plating cycle of the coin cell plating tests presented in Table 4.6, as less is plated for the modified cells compared to the pristine cells. Approximately 85% and 39% of the pristine amount was plated for the modified cells for the 100% SOC and 50% SOC tests, respectively. Moreover, the irreversible plating is greater for the pristine cells, which means that an increased amount of "dead Li" has been formed, as discussed in Section 2.6.3. Hence, these reported results confirm the expected correlation between a reduced first cycle ICL and increased ability of mitigating plating, due to the formation of a thinner SEI layer by amorphous carbon coating.

The post mortem characterisation supports these findings, as generally more Li plating was detected in the SEM micrographs of the pristine electrodes compared to the modified electrodes. Figure 4.16 illustrates how the 100% SOC electrodes of both powders have remaining plating visible on the surface, but that there is an increased number of dendrites on the pristine electrode compared to the modified electrode. No plating was observed on the surface of the 50% SOC modified electrodes, as illustrated by the micrographs in Figure 4.17. This was expected for the modified electrodes, as no irreversible plating was detected for these cells. Similarly, only $1.7 \pm 0.10\%$ was irreversibly plated for the pristine electrodes, which reduced the probability of detecting it in SEM. It should be noted that both the edges and the centre of all electrodes were investigated in SEM to increase the probability of observing plated Li. Moreover, it seems as the Li plating is superficial, as illustrated by the micrographs of the FIB cross sections in Figure 4.24. This is as there are no evident differences in the images of the cross sections of the pristine electrode with visible dendrites on the surface compared to the cross sections of the modified electrode without visible dendrites or the non-cycled electrodes in Figure 4.23. Nevertheless, only a limited area was explored for each electrode, which means that more cross sections should be analysed in order to substantiate this observation.

Overall, it seems as the modified graphite particles are less susceptible to plating. However, when analysing the capacity and CE plots of the coin cell plating tests in Figure 4.4 and 4.6, respectively, there are no apparent differences in the cell performance of the two powders after imposed plating. In fact, the plated cells of both powders are within the error bars of their respective reference cells in the final cycle of the programmes. Therefore, it would have been interesting to increase the number of cells in the parallels to improve the confidence in the results. In addition, the consequences of plating and the mitigation capability of the powders may become more evident after more cycles. In this way, the cycling programmes should be prolonged in further studies to investigate this effect.

CV and EIS results

The influence of the carbon coating can also be seen in the results from the CV and EIS cycling programme. The cyclic voltammogram in Figure 4.11 provides information on the kinetics of the graphite electrodes. The lithiation and delithiation reactions occur at higher and lower potentials, respectively, for the modified cell compared to for the pristine cell. In addition, the peaks are more distinct for the modified cell. This means that the modified cell seemingly has more favourable cell kinetics, as it is desirable that the lithiation and delithiation occur at the earliest stage possible, i.e. at higher and lower potentials, respectively. Moreover, this is reflected by the smaller electrode resistance for the modified cell compared to the pristine cell, as illustrated by the Nyquist plots in Figure 4.12. The ohmic resistance of the pristine cell is slightly larger than the modified cell, as illustrated by their respective R_1-values in Table 4.7 and 4.8. This represents the resistance at the highest frequencies, dominated by the ionic transport in the electrolyte between the graphite electrode and the reference, but could also have contributions from contact resistance, or changes in the available surface area of the graphite. The exact reason for the small increase observed here is not known. It is reasonable that these not differ greatly, as the electrolyte is the same for both cells. On the other hand, the charge transfer resistance for processes at medium frequencies (1 Hz to 1 kHz) differs to a greater extent, as the R_2- and R_3-values are much larger for the pristine cell. In particular the R_2-values reflect the total resistance of the electrodes, i.e. the charge transfer at the interface, the resistance of the SEI layer, and the desolvation of the Li-ions. The total electrode resistance is larger for the pristine cell, in agreement with the CV results. The physical interpretation of the last R-CPE circuit, with R_3, is not known, and probably contains contributions from several processes, including transport in the pore structure. Overall, these findings indicate that the carbon coating of the modified graphite powder provides superior electronic conductivity and desolvation of Li-ions at the electrode surface, which are key factors that contribute to reduce the risk of plating.

Another reason behind the improved mitigation properties of the modified powder may be the larger cell capacitance illustrated in Table 4.9, which was determined from the slope of the -Im-ω^{-1} plots in Figure 4.13. The greater capacitance translates into a greater active internal surface area, which contributes to an increased number of active sites where the intercalation of Li-ions may occur. This can also explain the lower total electrode resistance.

Moreover, it is interesting to compare the development in impedance after imposing plating in CV 1 and CV 2. Overall, the pristine cell has a higher electrode resistance in all the EIS measurements compared to the modified. It can be seen that the charge transfer resistance and ohmic resistance increase steadily, as illustrated by the values in Table 4.7. This is supported by the decrease in capacitance, and thus active surface area, which is reduced by 50% after each of the CV tests, as seen in Table 4.9. The modified cell follows the same trend as the pristine after CV 1, as the ohmic and charge transfer resistance increase steadily and the capacitance is reduced by approximately 50%, as seen in Table 4.8 and 4.9, respectively.

However, the increase in resistance for the modified cell is much larger after the second CV, which is illustrated by the much wider semicircle of the final impedance spectra, i.e. EIS 3, compared to the first two, i.e. EIS 1 and 2, in the Nyquist plot in Figure 4.12b. The capacitance values show the same trend here as well, as the capacitance is reduced by approximately 75% from EIS 2 to EIS 3, as seen in Table 4.9. Nevertheless, the overall electrode resistance and capacitance is still more favourable for the modified cell compared the pristine cell after both CV tests. Hence, the surface modification of the graphite particles seems to reduce the electrode resistance and improve the plating mitigation. However, after excessive plating, the difference between the two powders seems to diminish.

The post mortem characterisation of the CV electrodes may reveal additional information for this diminishing difference. The degradation due to the imposed plating can be observed on the macroscale in the camera images of the pristine and modified CV electrodes in Figure 4.14e and 4.14h, respectively. In addition, the SEM micrographs of the CV electrodes in Figure 4.18 reveal more extensive degradation compared to the non-cycled and coin cell plating cells, as the majority of the investigated areas are covered with several abnormal structures; a thick film, a mossy structure, and some small dendrites. The dendrites appear darker in the Z-contrast micrographs compared to the graphite particles, which is illustrated in Figure 4.21 for the pristine CV cell. This confirms the occurrence of plating. On the other hand, the film and mossy structures appear brighter in the Z-contrast micrographs, which is illustrated in Figure 4.22 for the modified CV cell. This indicates the presence of heavier elements, possibly on top of the Li plating, which likely corresponds to phosphorus and fluorine originating from the $LiPF_6$ electrolyte. In this way, the plating imposed in the CV test heavily degrades the electrodes with the occurrence of electrolyte depletion and film formation. This supports the trend observed in the impedance spectra and capacitance, as there is rapid degradation of the cells after each CV test. The excessive film formation may have contributed to the particularly worsened performance of the modified cell after CV 2. Hence, it would be interesting to repeat the test until the second CV, to investigate the extent of electrode degradation at this point, and possibly detect the point when the excessive film formation occurred.

5.2.2 Effect of SOC

In addition to investigating the effect of surface modifications, the effect of SOC at the point of imposing plating can be evaluated. In this thesis, plating was imposed at approximately 100% and 50% SOC in the coin cell plating tests, as given in Table 4.5. It was expected from literature, such as the review by Waldmann et al.,[31] that the risk of plating increases with an increase in SOC, due to the increased resistance towards lithiation for increased concentrations of Li in the graphite structure. This can also be seen in the results of this thesis, as much more of the theoretical amount is plated at 100% SOC compared to at 50% SOC, i.e. 80-97% and 5-13%, respectively. Moreover, the imposed overpotential was roughly 0.3 V larger for the 100% SOC cells compared to the 50% SOC cells, which can be observed in the lithiation curves in Figure 4.8a and 4.8b. This indicates more favourable conditions for Li plating, as a larger overpotential is a sign of slow Li-ion diffusion and intercalation rate.

The irreversible plating is also increased for plating at higher SOC, as seen by comparing the irreversible plating of the 100% and 50% SOC cells in Table 4.5. Petzl and Danzer[46] explain this to be due to the Li metal growing past the SEI layer and reacting with the electrolyte to a greater extent with increasing amounts of plating. This increases the irreversible capacity loss, as the increased distance between the plated Li and the electrode increases the probability for the Li plating to lose electrical contact and consequently form "dead Li". This underlines the benefits of a thinner SEI layer and corresponding reduced electrode resistance, as this enhances the electrical contact between the electrode and plated Li, which increases the probability for reversible oxidation of Li metal back into Li-ions upon discharge. In addition, this effect can be observed when comparing the reversibility of the two powders, i.e. the percentage stripped of total amount plated, which was approximately 85% for the pristine cells and 92% for the modified cells in the 100% SOC test. This correlates with the theory discussed here, as the impedance results showed that the SEI resistance was smaller for the modified cell, which hence may have contributed with reducing the irreversible capacity loss. Nevertheless, the SOC is a factor that strongly increases the risk of plating regardless of the mitigation properties of the graphite particles.

5.2.3 Effect of Plating C-rate

One can evaluate the effect of the C-rate applied during plating by comparing the results of the coin cell plating tests and the CV and EIS test. The plating C-rate was set to 3C in the coin cell tests, while the current response below 0 V in the CV tests varied between C/5 and C/2. Even though the plating was more extreme in the CV tests compared to in the coin cell plating tests, one can evaluate a few differences in the morphology of the remaining Li metal structures that possibly are related to the different C-rates. This is in accordance with previous works by Petzl and Danzer[46] and Wen et al.[48] who report a correlation between the charging C-rate and the plating structure, i.e. high charging currents ($\sim$1C) lead to the formation of thick dendrites and low charging currents ($\sim$C/5) lead to a mossy and more porous structure. The occurrence of thick dendrites due to a high charging C-rate (3C) is illustrated in the SEM micrographs of the 100% SOC cells in Figure 4.16. The mossy structure expected for lower charging C-rates (C/5) is not as easy to detect in the micrographs of the CV electrodes in Figure 4.18, due the majority of the electrodes being covered by the thick film formed from electrolyte depletion. However, a mossy structure can be observed in the left part of the 5 K magnification micrograph of the pristine electrode in Figure 4.18e. The higher porosity and hence larger surface area of this plating structure compared to the dendrites may be the reason for the electrolyte depletion and the resulting film formation on the CV electrodes. Nevertheless, this is a hypothesis that should be investigated further. Hence, to better verify the correlation between charging C-rate and the resulting plating structure, as well as the onset of film formation due to electrolyte depletion, one may repeat the coin cell plating tests for different plating C-rates, such as C/2 and C/5.

6 Conclusion

In this thesis, the main aim was to investigate whether the surface treatment of the graphite particles affects the susceptibility of the anode material towards Li plating, as well as how Li plating affects anode performance. In addition, the effect of external factors, such as the SOC and charging C-rate, during plating was examined.

One pristine and one surface modified synthetic graphite powder were compared. Plating was purposely imposed by lithiation of the graphite electrodes below 0 V. The amount of reversible and irreversible plating was determined from the stripping curves and differential capacity plots, and the capacity loss of the plating cycle, respectively. By using this method, it was possible to quantify the amount of plating more accurately compared to relying on the assumption that all charge below 0 V was plated. Post mortem SEM using SEs and BSEs was used to verify the occurrence of plating. It was shown that the plated Li metal had a characteristic dendrite structure, which stood in stark contrast to the graphite particles.

The electrochemical results showed that the modified particles were less susceptible to plating, as less Li plating was quantified and detected for these cells compared to the pristine cells. The reduced BET surface area and lower surface roughness of the modified particles were associated with a lower first cycle ICL, which is a factor that reduces the susceptibility to plating. In addition, the EIS measurements revealed a reduced electrode resistance for the modified cells both before and after plating, which supports the theory about how carbon coating reduces the resistance towards desolvation of Li-ions on the anode surface. The modified cells were found to have an increased active internal surface area, which may also reduce the risk of plating through the increased number of active sites for intercalation. In general, the reduced electrode resistance of the modified cells appears to increase the amount of intercalation at low potentials.

The effect of imposing plating at medium (50%) and high (100%) SOC was investigated. The results correlated with what was expected from literature, i.e. the risk of plating increases with increasing SOC due to the increased resistance towards lithiation for increased concentrations of Li in the graphite structure. The larger irreversible plating loss observed at higher SOC may be linked to the increased distance between the plated Li and the electrode with more excessive plating, as there is an increased risk of the plated Li losing electrical contact with the electrode. In addition, an effect of charging C-rate on the structure of plated Li was observed. High charging C-rates during plating resulted in thick dendrites, whereas low C-rates resulted in porous, mossy structures. The latter may be responsible for more rapid electrolyte depletion, but this should be validated by investigating the effect of plating smaller amounts at this C-rate.

In conclusion, the surface treatment of graphite particles with amorphous carbon coating appears to successfully mitigate the risk of Li plating, the key contributing factors being the reduction of the first cycle ICL and electrode resistance. In addition, external factors, such as plating at a high SOC and with low C-rates, should also be noted since they can increase the risk of irreversible plating and electrolyte depletion.

7 Further Work

The Li plating mitigation abilities of two synthetic graphite powders were investigated with the overall aim of developing better graphite anodes for fast charging LIBs. The surface treatment of graphite particles including amorphous carbon coating proved to reduce the susceptibility of Li plating on the graphite anode. However, the consequences of plating did not deviate substantially between the two powders when analysing the capacity and CE. Hence, further work should aim at investigating the long term consequences of plating by e.g. increasing the number of cycles after imposing plating. The effect of plating aged cells, such as imposing plating after 50-100 cycles, can also bring more insight into the graphite powders resilience and stability over time, which are important factors to consider for the application of LIBs in EVs.

In addition, it would be interesting to investigate the reliability of the quantification method presented in this thesis for smaller amounts of imposed Li plating. The effect of plating at a set of different SOC and C-rates may also provide insights into the occurrence of irreversible plating and the morphology of the deposited Li metal. Moreover, this can be used to improve battery management systems and charging protocols, as unfavourable charging conditions leading to increased irreversible Li plating and detrimental plating structures can be avoided. The graphite powders should also be tested in full cells with e.g. LFP as the counter electrode. This is as the reactions in the graphite/Li metal half cells may arise from reactions on the Li metal surface, which may not be present in full cells. Lastly, alternative post mortem techniques, such as GD-OS, could also be carried out to characterise irreversible Li plating on the graphite electrode.

References

[1] IPCC. (2022). *Climate Change 2022: Impacts, Adaptation and Vulnerability* (tech. rep.). Cambridge University Press. In Press.

[2] IEA. (2021). *Global EV Outlook 2021* (tech. rep.). International Energy Agency. https://doi.org/10.1787/d394399e-en

[3] Zubi, G., Dufo-López, R., Carvalho, M., & Pasaoglu, G. (2018). The lithium-ion battery: State of the art and future perspectives. *Renewable and Sustainable Energy Reviews*, *89*(March), 292–308. https://doi.org/10.1016/j.rser.2018.03.002

[4] Goodenough, J. B., & Park, K. S. (2013). The Li-ion rechargeable battery: A perspective. *Journal of the American Chemical Society*, *135*(4), 1167–1176. https://doi.org/10.1021/ja3091438

[5] Zhang, S. S. (2020). Identifying rate limitation and a guide to design of fast-charging Li-ion battery. *InfoMat*, *2*(5), 942–949. https://doi.org/10.1002/inf2.12058

[6] Zhang, H., Yang, Y., Ren, D., Wang, L., & He, X. (2021). Graphite as anode materials: Fundamental mechanism, recent progress and advances. *Energy Storage Materials*, *36*(December 2020), 147–170. https://doi.org/10.1016/j.ensm.2020.12.027

[7] Liu, R., Duay, J., & Lee, S. B. (2011). Heterogeneous nanostructured electrode materials for electrochemical energy storage. *Chemical Communications*, *47*(5), 1384–1404. https://doi.org/10.1039/c0cc03158e

[8] Warner, J. (2015). *The Handbook of Lithium-Ion Battery Pack Design*. Elsevier Inc. https://doi.org/10.1016/C2013-0-23144-5

[9] Kabir, M. M., & Demirocak, D. E. (2017). Degradation mechanisms in Li-ion batteries: a state-of-the-art review. *International Journal of Energy Research*, *41*(14), 1963–1986. https://doi.org/10.1002/er.3762

[10] Goodenough, J. B., & Kim, Y. (2010). Challenges for rechargeable Li batteries. *Chemistry of Materials*, *22*(3), 587–603. https://doi.org/10.1021/cm901452z

[11] Asenbauer, J., Eisenmann, T., Kuenzel, M., Kazzazi, A., Chen, Z., & Bresser, D. (2020). The success story of graphite as a lithium-ion anode material-fundamentals, remaining challenges, and recent developments including silicon (oxide) composites. *Sustainable Energy and Fuels*, *4*(11), 5387–5416. https://doi.org/10.1039/d0se00175a

[12] Loeffler, N., Bresser, D., Passerini, S., & Copley, M. (2015). Secondary lithium-Ion battery anodes: From first commercial batteries to recent research activities. *Johnson Matthey Technology Review*, *59*(1), 34–44. https://doi.org/10.1595/205651314X685824

[13] Fong, R., von Sacken, U., & Dahn, J. R. (1990). Studies of Lithium Intercalation into Carbons Using Nonaqueous Electrochemical Cells. *Journal of The Electrochemical Society*, *137*(7), 2009–2013. https://doi.org/10.1149/1.2086855

[14] Manthiram, A. (2020). A reflection on lithium-ion battery cathode chemistry. *Nature Communications*, *11*(1), 1–9. https://doi.org/10.1038/s41467-020-15355-0

[15] Andre, D., Kim, S. J., Lamp, P., Lux, S. F., Maglia, F., Paschos, O., & Stiaszny, B. (2015). Future generations of cathode materials: An automotive industry perspective. *Journal of Materials Chemistry A*, *3*(13), 6709–6732. https://doi.org/10.1039/c5ta00361j

[16] Julien, C., Mauger, A., Vijh, A., & Zaghib, K. (2015). *Lithium Batteries: Science and Technology*. Springer International Publishing. https://doi.org/10.1007/978-3-319-19108-9

[17] Nitta, N., Wu, F., Lee, J. T., & Yushin, G. (2015). Li-ion battery materials: Present and future. *Materials Today*, *18*(5), 252–264. https://doi.org/10.1016/j.mattod.2014.10.040

[18] Goriparti, S., Miele, E., De Angelis, F., Di Fabrizio, E., Proietti Zaccaria, R., & Capiglia, C. (2014). Review on recent progress of nanostructured anode materials for Li-ion batteries. *Journal of Power Sources*, *257*, 421–443. https://doi.org/10.1016/j.jpowsour.2013.11.103

[19] Chen, Z., Belharouak, I., Sun, Y. K., & Amine, K. (2013). Titanium-based anode materials for safe lithium-ion batteries. *Advanced Functional Materials*, *23*(8), 959–969. https://doi.org/10.1002/adfm.201200698

[20] Lu, Y., Yu, L., & Lou, X. W. D. (2018). Nanostructured Conversion-type Anode Materials for Advanced Lithium-Ion Batteries. *Chem*, *4*(5), 972–996. https://doi.org/10.1016/j.chempr.2018.01.003

[21] Novák, P., Goers, D., & Spahr, M. E. 7 Carbon Materials in Lithium-Ion Batteries (F. Beguin & E. Frackowiak, Eds.; 1st ed.). In: In *Carbons for electrochemical energy storage and conversion systems* (F. Beguin & E. Frackowiak, Eds.; 1st ed.). Ed. by Beguin, F., & Frackowiak, E. 1st ed. CRC Press, 2010. Chap. 7 Carbon M, pp. 263–328. ISBN: 978-1-4200-5307-4.

[22] Winter, M., Besenhard, J. O., Spahr, M. E., & Novák, P. (1998). Insertion electrode materials for rechargeable lithium batteries. *Advanced Materials*, *10*(10), 725–763. https://doi.org/10.1002/(SICI)1521-4095(199807)10:10<725::AID-ADMA725>3.0.CO;2-Z

[23] Chung, D. D. (2002). Review: Graphite. *Journal of Materials Science*, *37*(8), 1475–1489. https://doi.org/10.1023/A:1014915307738

[24] Kaskhedikar, N. A., & Maier, J. (2009). Lithium storage in carbon nanostructures. *Advanced Materials*, *21*(25-26), 2664–2680. https://doi.org/10.1002/adma.200901079

[25] Joho, F., Rykart, B., Blome, A., Novák, P., Wilhelm, H., & Spahr, M. E. (2001). Relation between surface properties, pore structure and first-cycle charge loss of graphite as negative electrode in lithium-ion batteries. *Journal of Power Sources*, *97-98*, 78–82. https://doi.org/10.1016/S0378-7753(01)00595-X

[26] Sharova, V., Moretti, A., Giffin, G., Carvalho, D., & Passerini, S. (2017). Evaluation of Carbon-Coated Graphite as a Negative Electrode Material for Li-Ion Batteries. *C*, *3*(4), 22. https://doi.org/10.3390/c3030022

[27] Peled, E., Tow, D. B., Merson, A., & Burstein, L. (2000). Microphase structure of SEI on HOPG. *Journal of New Materials for Electrochemical Systems*, *3*(4), 319–326.

[28] Profatilova, I. A., Kim, S. S., & Choi, N. S. (2009). Enhanced thermal properties of the solid electrolyte interphase formed on graphite in an electrolyte with fluoroethylene carbonate. *Electrochimica Acta*, *54*(19), 4445–4450. https://doi.org/10.1016/j.electacta.2009.03.032

[29] Matsuoka, O., Hiwara, A., Omi, T., Toriida, M., Hayashi, T., Tanaka, C., Saito, Y., Ishida, T., Tan, H., Ono, S. S., & Yamamoto, S. (2002). Ultra-thin passivating film induced by

vinylene carbonate on highly oriented pyrolytic graphite negative electrode in lithium-ion cell. *Journal of Power Sources*, *108*(1-2), 128–138. https://doi.org/10.1016/S0378-7753(02)00012-5

[30] Liu, X., Ren, D., Hsu, H., Feng, X., Xu, G. L., Zhuang, M., Gao, H., Lu, L., Han, X., Chu, Z., Li, J., He, X., Amine, K., & Ouyang, M. (2018). Thermal Runaway of Lithium-Ion Batteries without Internal Short Circuit. *Joule*, *2*(10), 2047–2064. https://doi.org/10.1016/j.joule.2018.06.015

[31] Waldmann, T., Hogg, B.-I., & Wohlfahrt-Mehrens, M. (2018). Li plating as unwanted side reaction in commercial Li-ion cells – A review. *Journal of power sources*, *384*, 107–124.

[32] Arora, P., Doyle, M., & White, R. E. (1999). Mathematical Modeling of the Lithium Deposition Overcharge Reaction in Lithium-Ion Batteries Using Carbon-Based Negative Electrodes. *Journal of The Electrochemical Society*, *146*(10), 3543–3553. https://doi.org/10.1149/1.1392512

[33] Legrand, N., Knosp, B., Desprez, P., Lapicque, F., & Raël, S. (2014). Physical characterization of the charging process of a Li-ion battery and prediction of Li plating by electrochemical modelling. *Journal of Power Sources*, *245*, 208–216. https://doi.org/10.1016/j.jpowsour.2013.06.130

[34] Persson, K., Sethuraman, V. A., Hardwick, L. J., Hinuma, Y., Meng, Y. S., Van Der Ven, A., Srinivasan, V., Kostecki, R., & Ceder, G. (2010). Lithium diffusion in graphitic carbon. *Journal of Physical Chemistry Letters*, *1*(8), 1176–1180. https://doi.org/10.1021/jz100188d

[35] Wiley, J. D., & Webster, J. G. (1982). Analysis and Control of the Current Distribution under Circular Dispersive Electrodes. *IEEE Transactions on Biomedical Engineering*, *BME-29*(5), 381–385. https://doi.org/10.1109/TBME.1982.324910

[36] Failla, R., Bologna, M., & Tellini, B. (2019). Dendrite growth model in battery cell combining electrode edge effects and stochastic forces into a Diffusion Limited Aggregation scheme. *Journal of Power Sources*, *433*(May), 126675. https://doi.org/10.1016/j.jpowsour.2019.05.081

[37] Tian, Y., Lin, C., Li, H., Du, J., & Xiong, R. (2021). Detecting undesired lithium plating on anodes for lithium-ion batteries – A review on the in-situ methods. *Applied Energy*, *300*(June), 117386. https://doi.org/10.1016/j.apenergy.2021.117386

[38] Wang, C., Zhao, H., Wang, J., Wang, J., & Lv, P. (2013). Electrochemical performance of modified artificial graphite as anode material for lithium ion batteries. *Ionics*, *19*(2), 221–226. https://doi.org/10.1007/s11581-012-0733-9

[39] Li, H., & Zhou, H. (2012). Enhancing the performances of Li-ion batteries by carbon-coating: Present and future. *Chemical Communications*, *48*(9), 1201–1217. https://doi.org/10.1039/c1cc14764a

[40] Xu, W., Welty, C., Peterson, M. R., Read, J. A., & Stadie, N. P. (2022). Exploring the Limits of the Rapid-Charging Performance of Graphite as the Anode in Lithium-Ion Batteries. *Journal of The Electrochemical Society*, *169*(1), 010531. https://doi.org/10.1149/1945-7111/ac4b87

[41] Kim, J., Nithya Jeghan, S. M., & Lee, G. (2020). Superior fast-charging capability of graphite anode via facile surface treatment for lithium-ion batteries. *Microporous and Mesoporous Materials*, *305*(March), 110325. https://doi.org/10.1016/j.micromeso.2020.110325

[42] Cai, W., Yan, C., Yao, Y.-X., Xu, L., Xu, R., Jiang, L.-L., Huang, J.-Q., & Zhang, Q. (2020). Rapid Lithium Diffusion in Order@Disorder Pathways for Fast-Charging Graphite Anodes. *Small Structures*, *1*(1), 2000010. https://doi.org/10.1002/sstr.202000010

[43] Natarajan, C., Fujimoto, H., Tokumitsu, K., Mabuchi, A., & Kasuh, T. (2001). Reduction of the irreversible capacity of a graphite anode by the CVD process. *Carbon*, *39*(9), 1409–1413. https://doi.org/10.1016/S0008-6223(00)00267-0

[44] Waldmann, T., Kasper, M., & Wohlfahrt-Mehrens, M. (2015). Optimization of Charging Strategy by Prevention of Lithium Deposition on Anodes in high-energy Lithium-ion Batteries - Electrochemical Experiments. *Electrochimica Acta*, *178*, 525–532. https://doi.org/10.1016/j.electacta.2015.08.056

[45] Smart, M. C., & Ratnakumar, B. V. (2011). Effects of Electrolyte Composition on Lithium Plating in Lithium-Ion Cells. *Journal of The Electrochemical Society*, *158*(4), A379–A389. https://doi.org/10.1149/1.3544439

[46] Petzl, M., & Danzer, M. A. (2014). Nondestructive detection, characterization, and quantification of lithium plating in commercial lithium-ion batteries. *Journal of Power Sources*, *254*, 80–87. https://doi.org/10.1016/j.jpowsour.2013.12.060

[47] Ghanbari, N., Waldmann, T., Kasper, M., Axmann, P., & Wohlfahrt-Mehrens, M. (2016). Inhomogeneous degradation of graphite anodes in Li-ion cells: A postmortem study using glow discharge optical emission spectroscopy (GD-OES). *Journal of Physical Chemistry C*, *120*(39), 22225–22234. https://doi.org/10.1021/acs.jpcc.6b07117

[48] Wen, J., Yu, Y., & Chen, C. (2012). A review on lithium-ion batteries safety issues: Existing problems and possible solutions. *Materials Express*, *2*(3), 197–212. https://doi.org/10.1166/mex.2012.1075

[49] Yang, X., & Rogach, A. L. (2019). Electrochemical Techniques in Battery Research: A Tutorial for Nonelectrochemists. *Advanced Energy Materials*, *9*(25), 1–10. https://doi.org/10.1002/aenm.201900747

[50] Barsukov, Y., & Macdonald, J. R. Electrochemical Impedance Spectroscopy (E. N. Kaufmann, Ed.; 2nd ed.). In: In *Characterization of materials* (E. N. Kaufmann, Ed.; 2nd ed.). Ed. by Kaufmann, E. N. 2nd ed. John Wiley & Sons, 2012. ISBN: 978-1-118-11074-4.

[51] Scientific, H. (2021). A guidebook to particle size analysis. https://static.horiba.com/fileadmin/Horiba/Products/Scientific/Particle_Characterization/Particle_Guidebook_06-2021.pdf

[52] Sing, K. (2001). The use of nitrogen adsorption for the characterisation of porous materials. *Colloids and Surfaces A: Physicochemical and Engineering Aspects*, *187-188*, 3–9. https://doi.org/10.1016/S0927-7757(01)00612-4

[53] Hjelen, J. (1986). *Scanning elektron-mikroskopi* (1st ed.). SINTEF, NTH.

[54] Sakamoto, T. Focused ion beam scanning electron microscope (The Surface Science Society of Japan, Ed.; 1st ed.). In: In *Compendium of surface and interface analysis* (The Surface Science Society of Japan, Ed.; 1st ed.). Ed. by The Surface Science Society of Japan. 1st ed. Tokyo: Springer Singapore, 2018. Chap. 13, pp. 181–186. ISBN: 9789811061561. https://doi.org/10.1111/jmi.12127.

[55] EL-CELL GmbH. (2021). User Manual PAT-Cell. https://el-cell.com/products/test-cells/standard-test-cells/pat-cell/#1569919604429-036be455-63ac

A Supplementary Figures

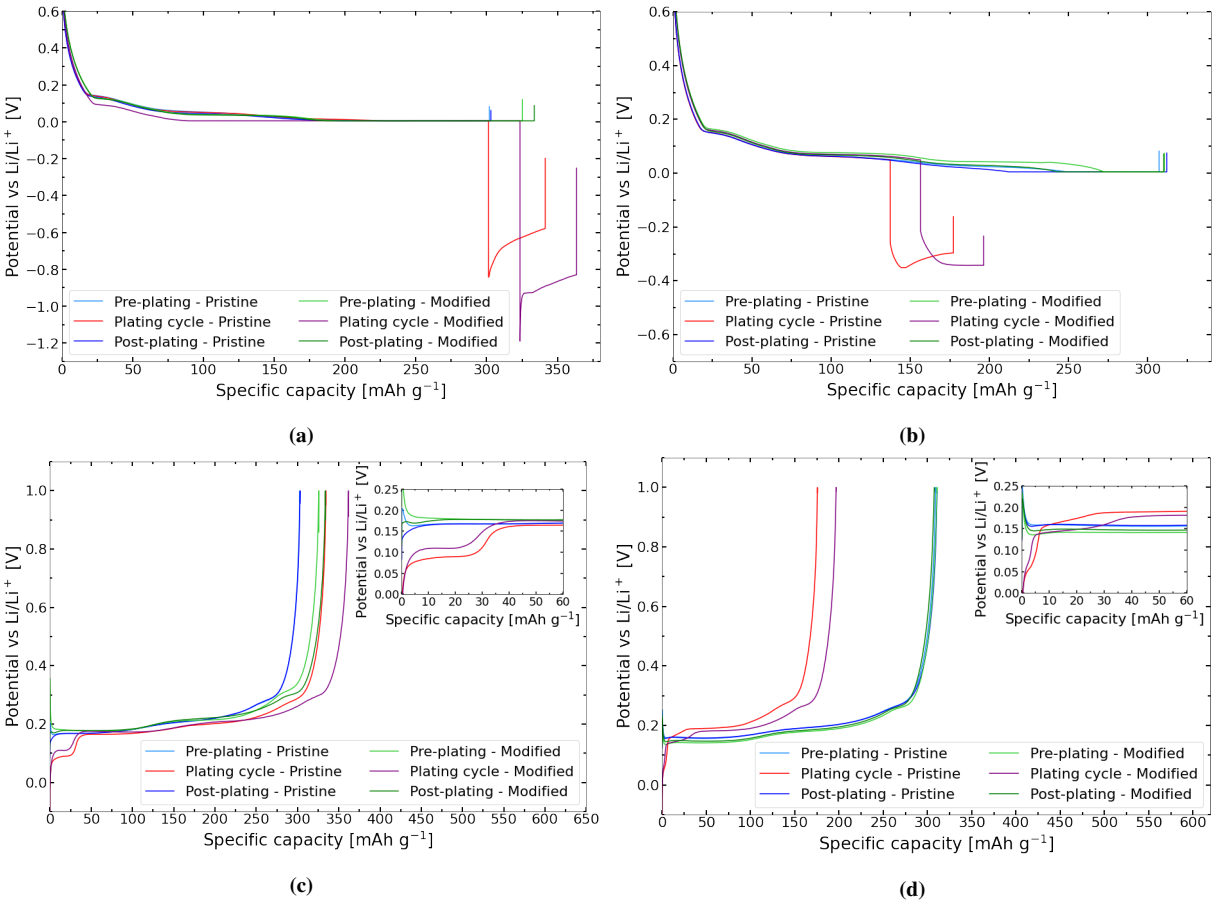

Figure A.1: Voltage curves of parallel cells undergoing the coin cell plating tests; (a) lithiation 100% SOC, (b) lithiation 50% SOC, (c) delithiation 100% SOC, and (d) delithiation 50% SOC.

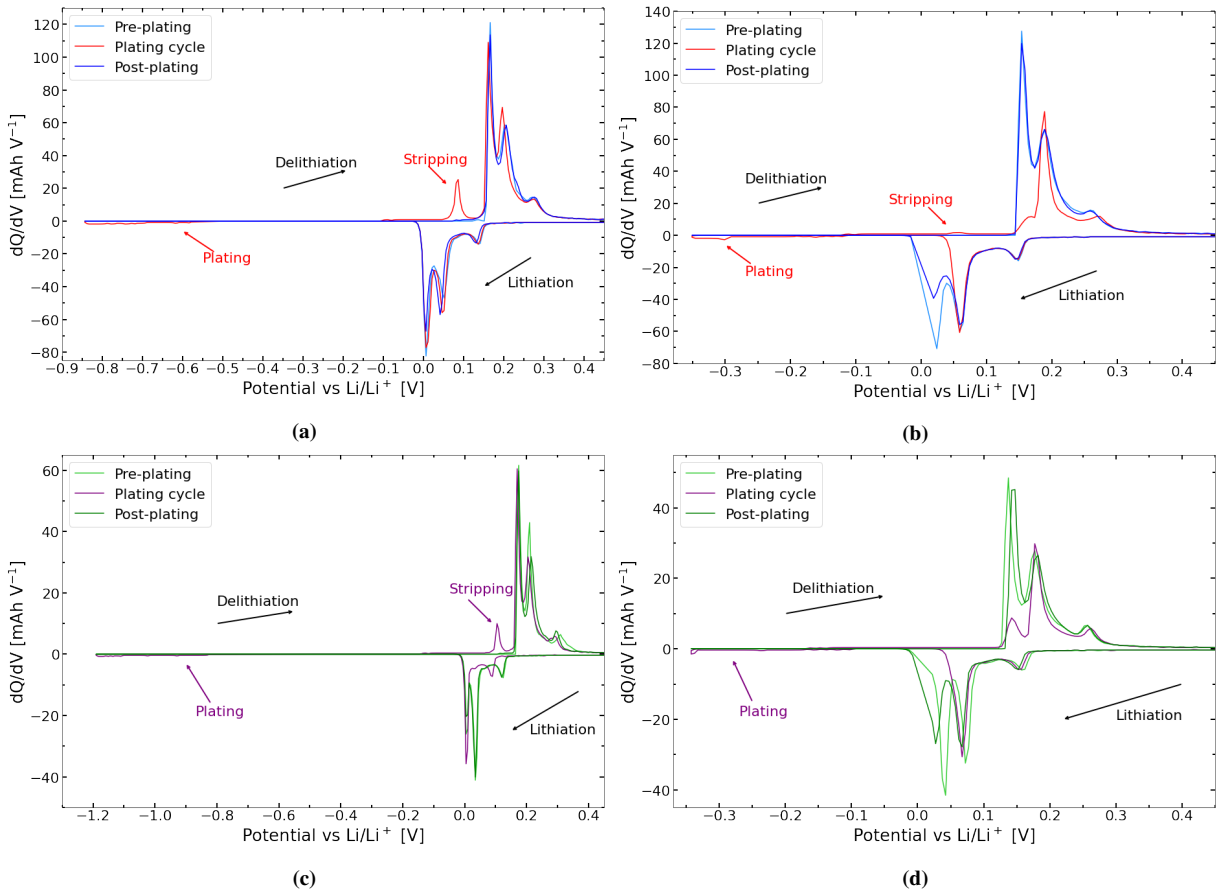

Figure A.2: Differential capacity plots of parallel cells undergoing the coin cell plating tests; (a) pristine 100% SOC, (b) pristine 50% SOC, (c) modified 100% SOC, and (d) modified 50% SOC.

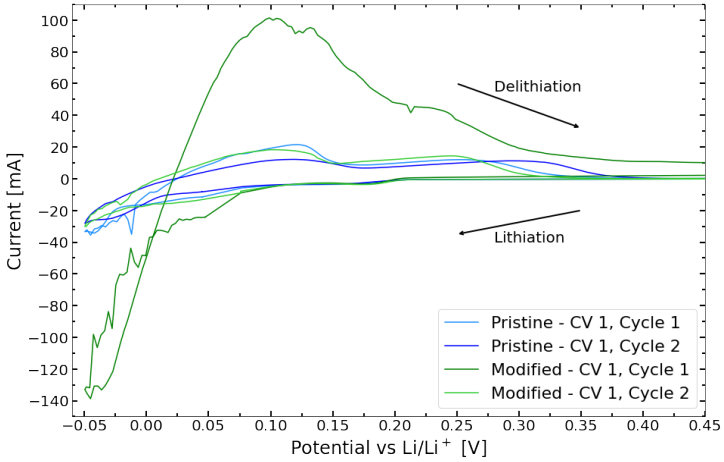

Figure A.3: Cyclic voltammogram of the first CV test.

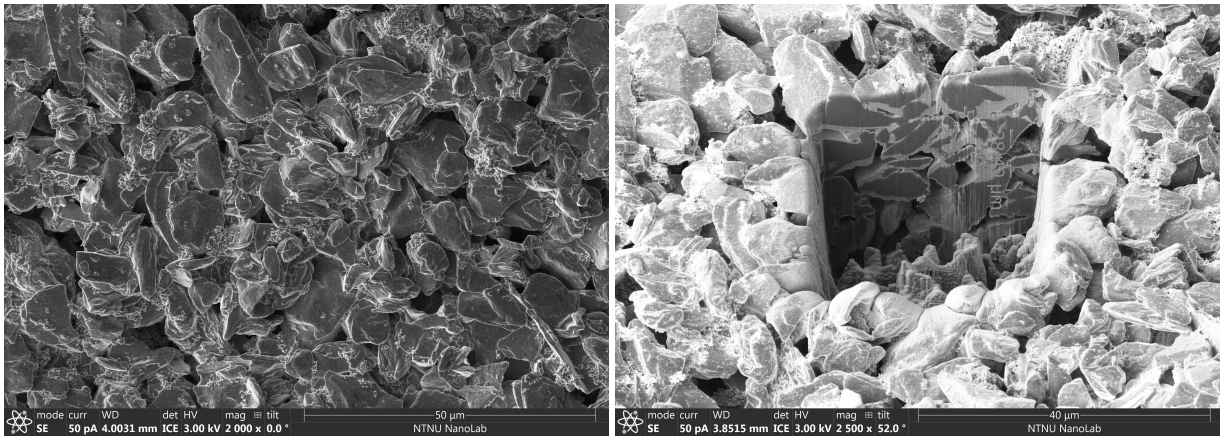

(a) **(b)**

Figure A.4: SEM micrographs of pristine 100% SOC plating electrode showing (a) an overview of the area with no visible plating (2 K) and (b) the cross section obtained by FIB (2.5 K).

B Supplementary Tables

Table B.1: Composition of all the tape casts used for making the electrodes, including the solid/liquid ratio of the corresponding slurry.

Powder	Tape	CB [wt.%]	CMC [wt.%]	SBR [wt.%]	Graphite [wt.%]	Solid/Liquid Ratio [-]
Pristine	1	2.006	1.513	1.550	94.93	0.7191
	2	1.997	1.513	1.655	94.84	0.6954
Modified	3	2.004	1.512	1.740	94.74	0.7107
	4	2.020	1.503	1.579	94.90	0.6970
	5	2.073	1.501	1.596	94.83	0.6941

Emilie Bjønnes

Surface Treatment of Graphite for the Mitigation of Lithium Plating

NTNU
Norwegian University of
Science and Technology